Computational Studies of Autoignition and Combustion in Low Temperature Combustion Engine Environments

by

Gaurav Bansal

A dissertation submitted in partial fulfillment
of the requirements for the degree of
Doctor of Philosophy
(Mechanical Engineering)
in The University of Michigan
2009

Doctoral Committee:

Associate Professor Hong G. Im, Chair
Professor James F. Driscoll
Professor Margaret S. Wooldridge
Research Professor Zoran S. Filipi

To mom, pops, and gudia
for a lifetime of support and encouragement

Acknowledgements

The last four years have been truly wonderful and I am filled with nostalgia as I write this section. First and foremost, I would like to thank my advisor Prof. Hong Im for his tremendous support, guidance, encouragement and trust in me throughout my doctoral studies. The freedom that he provided made it possible for me to pursue research ideas that I wanted to. He has been accessible whenever I needed any guidance or help. His advice and encouragement on both research matter and life in general have been most valuable. I have learnt a great deal from him and I will always cherish the long technical discussions we have had during our meetings.

Next, I would like to thank Profs. Jim Driscoll, Margaret Wooldridge, and Zoran Filipi for their valuable advice and participation in my dissertation committee. I am also grateful to Profs. James Sutherland of University of Utah, Su-Ryong Lee of Seoul National University of Technology, and John Bechtold of New Jersey Institute of Technology for fruitful collaboration and as co-authors. My undergraduate thesis advisors at IIT Delhi, Profs. M. R. Ravi and Anjan Ray showed me the beauty of combustion science and they are one of the main reasons I chose combustion as a field to build my career in. I am thankful to them for showing me such a wonderful path which has been very exciting and rewarding.

Next, I would like to thank my labmates over these years: Amit, Songtao, and Jingjing who greeted me and made me feel at home when I was a new graduate student. Amit helped me with everything related to linux, latex, and other hi-fi softwares. Songtao and Jingjing have been most helpful with anything related to both technical matter and fortran programming. Johnny and Paul who joined the lab at the same time as me. They have made the hours I spent at lab tremendously enjoyable. Saurabh who joined the lab a year after me. My discussions with Saurabh on both research and non-research issues have been very enjoyable.

Next, I would like to thank other great friends I have made at Umich whose friendship have made the time here pass so quickly: Kaushik, Ashish, Naveen, Sibu, Anurag, Deva, Saumil, Paul Teini, Paul Davidson, and Rushyal, among others I am sure to have left out. I will always cherish the tea-time discussions I have had with Kaushik, Ashish and Sibu

where we used to discuss everything under the sun. A special thanks to Greg who was the first friend I made at Umich. His help during my first year helped me settle down in United States.

Last, but not the least, I would like to thank my parents, my sister Garima, and my brother-in-law Sanjay for their support throughout these years. The constant source of energy that I have obtained from them is the reason I have been able to come this far in my doctoral studies starting from the time I started schooling twenty-one years ago.

This work was financially supported by the following:

1. University Consortium on Low Temperature Combustion for High-Efficiency Ultra-Low Emission Engines, directed by the University of Michigan, and funded by Department of Energy.

2. College of Engineering Deans/Named Fellowship.

3. Rackham Predoctoral Fellowship.

4. Rackham Travel Grants.

Table of Contents

List of Tables

Table

List of Figures

Figure

Abstract

Computational studies are performed on the autoignition and combustion characteristics in the presence of temperature and composition inhomogeneities encountered in modern internal combustion (IC) engines in which combustion is achieved primarily by autoignition of the reactant mixture. Examples of such engines include homogeneous charge compression ignition (HCCI) or partially premixed compression ignition (PPCI) engines, which are categorized under the generic term of low temperature combustion (LTC) engines. High-fidelity computational tools with varying levels of complexity are employed in order to systematically investigate essential driving physical and chemical mechanisms for the phenomena under consideration.

As a first baseline study, the effects of unsteady temperature fluctuations on the ignition of homogeneous hydrogen-air mixture in a constant-volume reactor is studied both computationally and theoretically using asymptotic analysis. It is found that ignition delay shows a harmonic response to the frequency of imposed temperature fluctuation and the response monotonically attenuates as frequency increases. The distinct effects of cumulative mean temperature during the induction period and those of instantaneous phasing of temperature fluctuation at the onset of ignition are identified.

Building on the results from the homogeneous ignition study, the effects of spatial transport on the autoignition characteristics are next investigated using a one-dimensional counterflow configuration, in which the well-defined unsteady scalar dissipation rate (χ) represents the effects of turbulent flow field. For a nonpremixed hydrogen-air system under study, response of the ignition delay to the frequency of the χ oscillation is found to be

highly non-monotonic with distinct behaviors in low-, intermediate-, and high-frequency regimes of χ fluctuation. A newly defined ignitability parameter is proposed based on the ignition kernel Damköhler number which systematically accounts for all the unsteady effects. *n*-Heptane, which exhibits a two-stage ignition behavior is studied next using similar configuration. Under steady χ conditions, the first-stage ignition is found to be insensitive to variation in χ, while the second-stage ignition is affected significantly. Similar to the hydrogen case, the response of the ignition delay to frequency of χ fluctuation is found to be highly non-monotonic. Interestingly, two-stage ignition is observed even at significantly high initial temperatures when the ignition kernel is subjected to unsteady χ. Mechanism for the reappearance of the two-stage ignition in unsteady conditions is found to be not chemical but is attributed to the spatial broadening of the ignition kernel and subsequent radical losses.

Guided by the above findings, multi-dimensional simulations are conducted to investigate the effects of spatial fluctuations in temperature and composition. Non-reacting 3D engine simulations are first conducted using a full-cycle engine simulation to investigate different mixture formation scenarios that might exist in LTC engines prior to autoignition. Different temperature-equivalence ratio correlations are found at the top dead center depending on the timing of fuel spray injection and the level of wall heat loss. Small-scale effects of these different mixture formation scenarios on the autoignition and subsequent front propagation are then studied using high-fidelity direct numerical simulation (DNS). Numerical diagnostics are developed to identify different modes of heat release such as premixed flame propagation, spontaneous ignition front propagation, and homogeneous autoignition.

In the last part of dissertation, a novel principal component analysis (PCA) based approach is used to identify intrinsic low-dimensional manifolds in a complex autoigniting environment. A small number of principal components (PCs), which are essentially a linear combination of primitive variables like species mass fractions and temperature, are found

to very well represent the complex reacting system. The approach thus provides a promising modeling strategy to reduce the computational complexity in solving realistic detailed chemistry in mixed mode combustion systems.

Chapter 1

Introduction

Dwindling petroleum supply and ever-increasing greenhouse gas emissions are two extremely important problems faced by mankind today. Efficient and clean utilization of fossil fuels is thus critical to enhance the energy sustainability and to overcome the threat of global warming. Given the fact that in United States two-thirds of the total petroleum consumption is attributed to transportation, there is an urgent need to develop highly efficient and clean internal combustion (IC) engines for automotive applications. Recent developments in internal combustion (IC) engine research have mainly focused on achieving low temperature combustion (LTC) in favor of superior efficiency and emission performance [1, 2]. LTC engines can also enable the use of a wider spectrum of fuels such as hydrogen and bio-fuels such as ethanol, which can slowly reduce our dependence on fossil fuels.

A number of new engine concepts, such as homogeneous charge compression ignition (HCCI), controlled autoignition (CAI), and partially premixed compression ignition (PPCI), all fall into this new breed of IC engines design. The central idea of these designs is to operate the engines fuel-lean and at low temperatures, thus avoiding the formation of nitric oxides (NOx) and soot. Despite all the promises, however, two important technical issues are impeding the immediate development of LTC engines. Firstly, the initiation of combustion in LTC engines generally relies on spontaneous autoignition of charge without any external ignition sources such as a spark. Therefore, maintaining the consistent

ignition timing and combustion phasing in different engine cycles becomes a tremendous challenge. Secondly, the rate of heat release is not controlled, neither by the finite turbulent flame propagation speed as in a conventional spark-ignition (SI) gasoline engine, nor by the rate of fuel-air mixing as in a conventional compression-ignition (CI) diesel engine. Thus, if large amounts of mixture autoignites simultaneously, there is an extremely rapid pressure rise which causes severe knock and mechanical stresses to the engine.

Mixture inhomogeneities play an important role in LTC engine combustion. Sample images acquired by Richter *et al.* [3] using planar laser-induced fluorescence (PLIF) of the OH radical revealed a non-uniformly igniting charge in spite of efforts to make the most homogeneous fuel, temperature, and residual gas distribution possible for that engine configuration. Several other PLIF- and chemiluminescence-based experiments have shown similar results [4–8]. From these results, it appears that inhomogeneities dictate the spatial and temporal distribution of autoignition sites within an LTC engine. Therefore, as a possible remedy, some degree of stratification is deliberately introduced [9, 10] in order to avoid extremely rapid pressure rise and heat release rates in the engine. Exhaust gas recirculation (EGR) [11] and multiple fuel injection [12] are some of the techniques that are employed to introduce charge stratification in the engine cylinder. Moreover, some natural thermal stratification always exists in the cylinder due to wall heat loss. Therefore, one of the major technical challenges in the development of LTC engines is the difficulties in controlling the start and subsequent phasing of combustion, because they essentially rely on the spontaneous autoignition of the mixture pockets that are subjected to varying degrees of flow/scalar inhomogeneities.

Due to turbulence mixing, large scale stratification of charge leads to small scale inhomogeneities in temperature, fuel mass fraction, and EGR. The presence of mixture inhomogeneities results in a mixed mode combustion in LTC engines, as both volumetric and front-like combustion modes can occur. Optical experiments with HCCI engines by Hultqvist *et al.* [13] have demonstrated the existence of reaction fronts that propagated at

speeds much higher than the deflagration speeds under such conditions. They have also found that the small scale hot spots, which evolve due to compression heating, have reaction zones propagating at speeds comparable to flame propagation speeds. Similarly, visualization of combustion in the rapid compression facility at University of Michigan has shown the presence of reaction fronts with speeds higher than normal flame propagation speeds [14]. Very recently, experiments have been conducted in an optical engine [15, 16] to investigate the effects of both thermal and compositional stratification. In these experiments also a very high speed progression (much greater than premixed flame speeds) of combustion event from hot regions to cold regions is observed in the engine. Moreover, it is also found that if stratification in fuel concentration is introduced opposite to the stratification in temperature, then the effects of thermal stratification are substantially reduced and a more volumetric-like ignition mode is observed. As a theoretical basis for the observed phenomena, Zeldovich [17] identified the regimes of a reaction front propagating through a non-uniform mixture. Of particular relevance to LTC combustion are: (i) *spontaneous propagation*, which is the sequential autoignition of neighbouring mixture purely due to the differences in their respective ignition delays, without any contribution from molecular diffusion, and (ii) *premixed deflagration*, which is a standard premixed flame propagating by molecular diffusion and conductive mechanisms. Therefore, the role of these two regimes as well as the importance of volumetric ignition sites in an LTC engines should be completely understood for optimal development of these engines.

At present, the effects of turbulence on autoignition and the ignition delay time are also still far from being understood. Turbulence has a two-folds effect on autoignition in stratified systems: Turbulence enhances mixing which promotes the reaction rate, and at the same time high turbulence leads to high levels of scalar dissipation rates which inhibits reaction by increasing the loss of radicals and heat from the ignition kernel [18]. In-depth understanding of the turbulence-autoignition interaction is therefore also crucial for optimal design of these engines.

Computational modeling of flow and combustion in engines can serve as an important tool for understanding the underlying physics and thus is extremely essential to shed light on technical issues mentioned eariler. However, the in-cylinder combustion process is an extremely complex multi-physics phenomena with simultaneous presence of multi-phase flow, turbulence, heat and mass transport, and chemical kinetics, which non-linearly interact with each other. As such, it is impossible to conduct direct numerical simulations of realistic engine combustion even in the foreseeable future due to the extremely high computational cost involved. High-fidelity computational studies in simpler idealistic configurations which isolate different physical phenomena are, therefore, valuable and provide great insights of the complex combustion process. Combination of insights obtained from various simplified studies can then provide an overall understanding of the complete process. Moreover, datasets generated from high-fidelity computational studies serve as a benchmark for developing turbulent closure models for Reynolds-Averaged-Navier-Stokes (RANS) and Large-Eddy-Simulation (LES) for conducting realistic engine simulations. In view of these important facts, in this dissertation, models of various levels of complexity are employed, ranging from a homogenous zero-dimensional (0-D) model to one-dimensional (1-D) counterflow configuration to high-fidelity two-dimensional (2-D) direct numerical simulations (DNS).

First part of the dissertation is devoted to understanding turbulence-autoignition interaction. In this part, effects of monochromatic temporal oscillations of flow velocity or some key scalar on autoignition are investigated via reduced dimensional models in canonical configurations. The results of time-varying response can be readily translated to a spatially non-uniform situation by the Eulerian-Lagrangian conversion. Extensive parametric studies are conducted in order to map out the ignition behavior in terms of some key representative system parameters, such as the characteristic amplitude and wave number of elementary mode of the fluctuations.

As a first step, in Chapter 3 a homogeneous constant-volume ignition of hydrogen-air

mixture subjected to imposed harmonic oscillation in temperature is studied. Relevance of such a simplified model to practical LTC engine application can be further justified based on the following aspects. For both premixed or nonpremixed systems, the ignition kernel can be approximated as a homogeneous mixture pocket subjected to heat and mass transport with the surroundings, such that the subsequent evolution of the ignition event may be described by a Lagrangian description of an ignition kernel whose uniform thermodynamic conditions undergo temporal variations during the ignition delay period. Among the many thermodynamic variables, temperature is chosen in this study because reaction is most sensitive to temperature. In IC engine applications, the time-varying temperature may also represent the isentropic heating of the combustion chamber during the compression stroke. Parametric studies are conducted to examine the unsteady ignition characteristics of hydrogen-air mixture in response to the imposed temperature oscillations at various frequencies. Hydrogen-air mixture is chosen because of the following two reasons. Firstly, hydrogen is of importance because it may be blended into gasoline, diesel and other alternative fuels as a means to control ignition, combustion and pollutant formation characteristics of the engine. Secondly, the ignition chemistry of hydrogen-air mixture is well understood and forms the building block in understanding more complex hydrocarbon fuels. The resulting system with detailed chemistry is integrated numerically. In addition, analytic closed-form solutions are also obtained using activation energy asymptotics. The primary goal is to find the response of the ignition delay to frequency of the imposed temperature oscillations. Different initial temperature and pressure conditions are chosen such that the two distinct chemical ignition characteristics of the hydrogen-oxygen system (high temperature and low temperature ignition regimes) can be studied. Effects of the initial pressure on the overall ignition response is also examined. The role of temperature oscillation on ignition is assessed in terms of its cumulative effect over the entire induction period versus the instantaneous phasing of temperature excursion near the onset of runaway.

Next, the effects of sinusoidal fluctuations in the strain rate on the autoignition behav-

ior of nonpremixed fuel-air mixtures is studied. The study is based on the viewpoint that the turbulent eddies at different scales have different characteristic time scales; smaller eddies, which are often more effective in influencing the ignition kernels, are at shorter time scales such that one may need to consider multiple repeated attacks of such eddies during the ignition delay. Previously, the effects of unsteady strain rate on autoignition behavior have been studied for hydrogen-air [19] and methane-air mixtures [20], considering a monochromatic sinusoidal strain rate oscillation. Sung and Law [19] found that an initially non-ignitable system may ignite under oscillatory conditions if the excursion time over favorable strain conditions was long enough compared to a characteristic ignition delay time. Consistent results were found by Mason *et al.* [21] who studied the effects of impulsive strain rate forcing on ignition of non-premixed hydrogen-air mixtures. More recently, Liu and coworkers [22] studied autoignition in a strained nonpremixed system by employing *n*-heptane as a surrogate fuel for diesel, providing many important characteristics of the ignition kernel behavior as well as the net effects of the steady scalar dissipation rate [22]. They extended the study to consider an impulsive burst in the strain rate [23], in order to represent an intermittent attack of a small turbulent eddy on the ignition kernel. The effects of different amplitude and timing have been investigated while the duration of the impulse was fixed.

The results from these unsteady ignition studies seem to suggest that the ultimate fate of an ignition kernel depends on the history of the temporal excursion of the strain rate during the ignition delay. However, a unified understanding of autoignition behavior in response to various parameters governing the unsteady strain rate oscillation such as amplitude and frequency is still missing in these studies. Therefore, considering the findings from previous studies, we extend the parametric studies to consider a wider range of frequencies and different mean scalar dissipation rates with respect to the steady ignition limit, with an objective to identify a unifying criterion for unsteady effects. A counterflow configuration is adopted in which similarity assumption makes the system one-dimensional. Fuel and air

are injected from opposing nozzles some distance apart. Scalar dissipation rate fluctuates by fluctuating velocity at the nozzle inlet sinusoidally. Thus, in this configuration, fluctuations in strain rate results in fluctuations in scalar dissipation rate. Therefore, for this study, the terms 'strain rate fluctuation' and 'scalar dissipation rate fluctuation' are used interchangeably.

Firstly, hydrogen-air system is investigated in Chapter 4. Detailed investigation is undertaken to examine the ignition kernel growth. A non-dimensional ignitability parameter is proposed based on ignition kernel Damköhler number such that the unsteady ignition delay behavior can be uniquely mapped to this parameter. Subsequently, a unified ignitability criterion is proposed. After gaining important insights from the simple hydrogen-air system, autoignition behavior of *n*-heptane, which is more directly relevant to IC engines, is studied in Chapter 5. One of the key distinctive features of *n*-heptane, which is most pronounced in diesel engine applications, is that they often exhibit two-stage ignition under the typical operating conditions. This behavior has been explained by the negative temperature coefficient (NTC) regime, due to a competition between recombination of isomerization products and the activation of radical branching through H_2O_2 at intermediate temperatures near 900K [24]. In this dissertation, we attempt to provide a more complete understanding of the effects of steady and unsteady scalar dissipation rate on *n*-heptane autoignition at conditions relevant to LTC engines. In particular, it complements previous work of Liu *et al.* [22, 23] by emphasizing on the effect of *time scales* of the unsteady fluctuation. Autoignition behavior is studied in both negative-temperature-coefficient (NTC) regime, as well as at higher temperatures. Implications of the results on modeling of autoignition in turbulent flows in RANS/LES context are discussed.

Next part of the dissertation is focused on understanding the different modes of heat release which may exist in LTC engines due to the presence of inhomogenities in temperature and equivalence ratio. As mentioned earlier, premixed flame propagation, spontaneous ignition front propagation [17], and homogeneous autoignition may all exist in LTC engines

due to the presence of mixture inhomogeneities. Towards this goal of understanding different combustion modes in LTC engines, the first objective is to identify possible mixture formation patterns close to top-dead center (TDC) prior to autoignition in a typical LTC engine. Of particular interest is to identify the possible correlations between temperature and equivalence ratio fields prior to autoignition. To this end, in Chapter 6, non-reacting three-dimensional (3D) real engine simulations are performed using a multi-dimensional KIVA-3v code which is widely used for internal combustion engine simulations [11, 25]. Depending on the fuel injection timing, exhaust gas recirculation, and the amount of wall heat loss, different correlations may exist between temperature and equivalence ratio at TDC. Essentially, it is found that two distinct scenarios exist: (1) early start of fuel injection results in largely uncorrelated temperature and equivalence ratio fields mostly due to turbulence mixing and wall heat loss; (2) late start of fuel injection results in negatively correlated temperature and equivalence ratio fields mostly due to evaporative cooling. Furthermore, insufficient mixing between hot residual gas which contain oxygen and the fresh charge can result in a negatively correlated temperature and equivalence ratio fields even in early injection or port fuel injection cases (see, for example, Fig. 3 of Ref. [11]).

The non-reacting engine simulations provide guidance to representative initial scalar fields to be studied for the autoignition characteristics. Using the Kiva-3v results to set-up initial conditions, in Chapter 7, the ignition and front propagation events are studied using two-dimensional (2D) direct numerical simulation (DNS) with detailed chemistry. Three different initial conditions are studied: Case (A) - a baseline case with only thermal inhomogeneities and a uniform equivalence ratio field. This configuration has been studied in a few recent studies [26–28]; Case (B) - uncorrelated temperature and equivalence ratio fields; and Case (C) - negatively correlated temperature and equivalence ratio fields. High pressure hydrogen-air mixture is used and a constant volume configuration is adopted. Detailed hydrogen-air chemistry is employed. A two-dimensional homogeneous isotropic turbulence spectrum is imposed on the initial field. Main reason for using hy-

drogen is to reduce the computational complexity in solving detailed chemistry which is already very high due to the need for resolving extremely thin fronts which occur at high pressure. However, as mentioned earlier, hydrogen-air mixture is important in its own right for its practical relevance in blended hydrocarbon and other alternative fuels. Although turbulence is inherently three-dimensional, the present two-dimensional study is a first step in understanding the effects of inhomogeneities in both temperature and equivalence ratio which are representative of inhomogeneities in real LTC engines and provides valuable insights.

As mentioned before, due to the presence of equivalence ratio and temperature inhomogeneities, combustion occurs in both volumetric and wave-like propagation modes. Therefore, in Chapter 7 a numerical diagnostic criterion is developed which can quantitatively distinguish between the different modes of heat release such as homogeneous autoignition, spontaneous ignition front propagation [17] and premixed deflagration, in an igniting mixture with thermal and compositional stratification. Previously, a straightforward temperature gradient cut-off has been proposed [26] to distinguish between spontaneous ignition front and premixed deflagration. However, this criterion will not be valid when inhomogeneities in both temperature and equivalence ratio are present. More recently, Chen and coworkers [27] have proposed the comparison of displacement speed of the front with some reference laminar flame speed, to distinguish between the combustion modes. However, if the mixture has both thermal and compositional stratification, then it is difficult to identify the reference laminar flame speed. Moreover, using an unstretched steady premixed flame speed as a reference in this highly transient autoigniting turbulent medium is questionable. Furthermore, this criterion breaks down if the reaction front is not thin and the front propagation is not one-dimensional, i.e. if the front does not propagate normal to itself. In this case, displacement speed may not correctly represent the ignition front speed. Thus, an alternative criterion is sought in this dissertation. To this end, autoignition behavior is investigated through several 1D simulations with different levels of initial temperature

gradients. A quantitative criterion based on an appropriately defined Damköhler number of HO_2 species is developed in order to distinguish between the wave-propagation-like mode and homogeneously auto-igniting mode, and to identify if the propagating wave is a spontaneous ignition front or a premixed deflagration. This criterion is applied on the two-dimensional DNS cases.

So far we have attempted to obtain fundamental physical insights of the complex combustion process occuring in LTC engine environments. In the last part of the dissertation, we focus on the modeling aspects of LTC combustion in the context of RANS/LES. Modeling of turbulent combustion in modern engines which employ the LTC strategy is highly complex because of the presence of mixed modes of combustion: front propagation occurs in partially-premixed inhomogeneous mixtures, and also other pheonomena such as autoignition and extinction may be simultaneously present. Current state-of-the-art turbulent combustion models for tackling with this problem are the broad category of flamelet models [29], conditional-moment-closure (CMC) models [30], and transported probability density function (PDF) models [31]. In flamelet or CMC models an *a priori* low-dimensional subspace, such as mixture fraction, enthalpy, or some form of a progress variable is employed and it is assumed that in this subspace the fluctuations of reactive scalars are small. One [32, 33] and two-dimensional [34, 35] models have been formulated. However, the choice of the low-dimensional subspace is largely based on physical intuition and not on mathematically rigorous methods, and therefore, may not do a good job in achieving low levels of fluctuations. Second-order CMC methods [36] have also been formulated precisely to address this issue. However, application of second-order CMC using detailed chemistry is formidable because large number of conditional variance and covariance equations need to be solved.

In this dissertation, a novel methodology based on principal component analysis (PCA) is proposed to identify the inherent low-dimensional manifolds in complex combustion systems. PCA offers the potential to automate the selection of an optimal basis for repre-

senting the low-dimensional manifolds which exist in turbulent combustion [37, 38]. For conducting PCA, high-fidelity datasets from either DNS or experiments are required. The central idea of PCA is to linearly transform a number of possibly correlated variables into a smaller number of uncorrelated variables called principal components (PCs). PCs are essentially linear combination of original reactive scalar variables such as temperature and species mass fractions. The first PC accounts for as much of the variability in the data as possible, and each succeeding PC accounts for as much of the remaining variability as possible. It is a rigorous mathematical technique [39, 40], and one can precisely define the error in parameterizing the original reactive scalars in the low-dimensional manifold. As such, PCA provides a low-dimensional subspace in which the fluctuations of reactive scalars are small, hence, offers a way to reduce the computational complexity in simulating realistic detailed chemistry. One of the caveats of using PCA is that principal components may not be conserved scalars and therefore their source terms also need to be parameterized in the low-dimensional principal component space.

In Chapter 8, we apply PCA to the DNS database of autoignition and front-propagation in inhomogeneous turbulent hydrogen-air mixture. A dataset representing the entire time-history of autoignition and front propagation is compiled from the DNS database and PCA is applied on it. The PCA parameterization is compared with other standard parameterizations based on mixture fraction, enthalpy, and scalar disspation rate which are generally used in flamelet or CMC models. An effort is made to parameterize the source terms of PCs in the low-dimensional space.

Next chapter presents the mathematical formulation and computational methodology for various numerical models employed in this dissertation. Finally, in Chapter 9 the main results of this dissertation are summarized along with recommendations for future work.

Chapter 2

Formulation and Numerical Method

In this chapter, the formulation and numerical methods for the models employed in the subsequent chapters are described. The computational models used in this dissertation include a homogeneous reactor, a counterflow configuration, a multi-dimensional RANS computational fluid dynamics solver KIVA-3v for engine simulations, and a multi-dimensional DNS flow solver. The underlying mathematical formulation and numerical solution techniques for these models will be briefly discussed.

2.1 Homogeneous Reactor Model

The time evolution of a homogeneous reacting gas mixture in a closed constant volume system is a simple modeling approach for several practical problems such as I.C. engine combustion. Although the assumption of mixture homogeneity takes away several key physical issues, it makes the problem simple and readily amenable to modeling, and in special cases closed-form analytical solutions can also be obtained using activation-energy-asymptotics (AEA). The state of such a homogenous reactor is described by the pressure (P), specific volume (ν), Temperature (T) and species mass fractions (Y_k).

This model is used in Chapter 3 to study the effects of unsteady temperature fluctuation on the autoignition of homogeneous hydrogen/air mixture. The governing equations for constant volume reactor for the k^{th} species mass fraction and temperature are given as:

$$\frac{dY_k}{dt} = \frac{W_k \omega_k}{\rho_0}, \tag{2.1}$$

$$\rho_0 c_v \frac{dT}{dt} = -\sum_k u_k W_k \omega_k + \rho_0 c_v \frac{dT_I}{dt}, \tag{2.2}$$

where W_k, ω_k, u_k are the molecular weight, reaction rate and internal energy of k^{th} species, respectively, and ρ_0, c_v are density and specific heat at constant volume for the reacting mixture, respectively. The additional source term in the temperature equation (second term on rhs) represents the imposed temperature oscillation given in a sinusoidal form:

$$T_I(t) = T_0 * (1 + A \sin(2\pi f t)) \tag{2.3}$$

where T_0 is the initial temperature, and A and f are the amplitude and frequency of temperature oscillation, respectively.

The time evolution of the reactor state is described by the above set of ordinary differential equations. The governing equations are numerically integrated by the DVODE software package [41], which uses an implicit scheme to perform the time integration. The code is interfaced with CHEMKIN [42] package for computing detailed reaction rates and thermodynamic properties.

2.2 Counterflow Configuration

The counterflow, also known as the opposed flow, serves as a convenient configuration to study the effects of flow straining on the characteristics of laminar flames and their autoignition behavior. This is due to the well-defined fluid-mechanical strain field in such flows, allowing efficient computational solution. Furthermore, experimental apparatus can be easily set up, allowing for direct quantitative comparison between model prediction and measured data. Figure 2.1 shows a schematic of the counterflow configuration.

Two opposing axisymmetric nozzles are separated by a distance L. Either a diffusion or

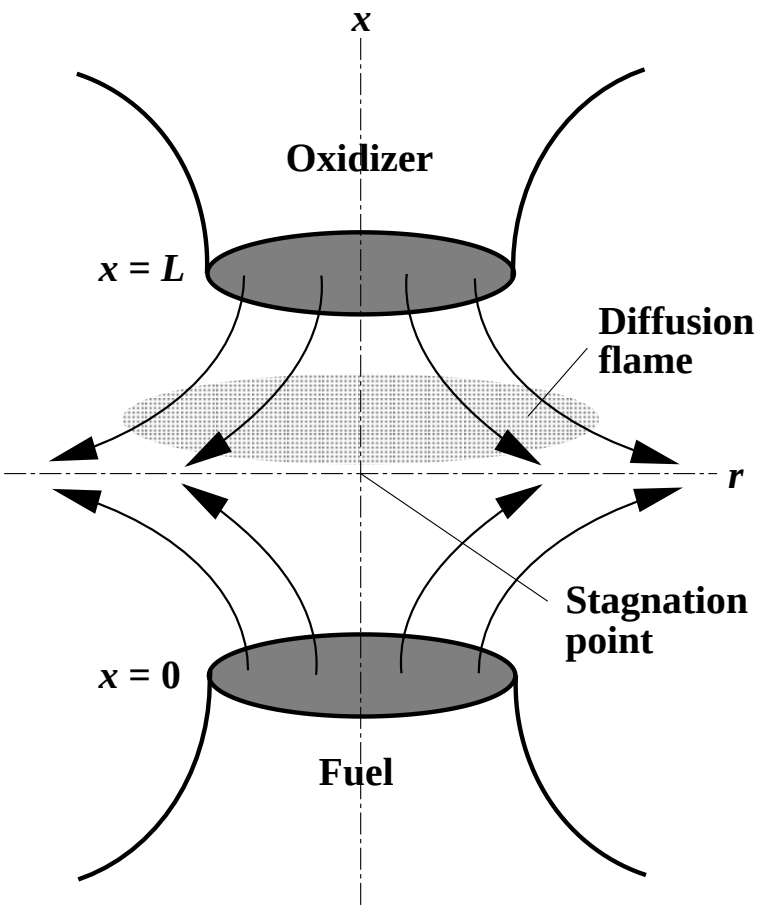

Figure 2.1: Schematic of the counterflow configuration.

a premixed flame can be formed in between the two nozzles. A diffusion flame is formed (as seen in figure 2.1) when fuel and oxidizer are supplied at $x = 0$ and $x = L$ respectively. A back-to-back twin premixed flame can be formed by supplying premixed fuel-oxidizer mixture through both the nozzles. Counterflow configuration is especially well-suited to study the flame response to unsteadiness in strain rate or any other variable such as temperature or equivalence ratio. Unsteady strain rate field can be imposed by fluctuating the velocity at the boundary. These studies form a building block for understanding the complex turbulent combustion phenomena in the laminar flamelet regime [43]. This configuration is adopted in Chapters 4 and 5 to investigate autoignition response to unsteady strain rate fields for hydrogen and *n*-heptane fuels, respectively.

2.2.1 Mathematical formulation

The governing equations for the steady opposed-flow geometry had been originally formulated by Kee *et al.* [44] and implemented in the OPPDIF code [45]. The formulation for the unsteady system was derived and refined in order to deal with the numerical stiffness arising from fast transients coupled with acoustic waves [20, 46]. Defining the self-similar variables for the axial velocity, scaled radial velocity, temperature, and k^{th} species mass fraction as:

$$u = u(t,x), \quad v/r = V(t,x), \quad T = T(t,x), \quad Y_k = Y_k(t,x), \tag{2.4}$$

the conservation equations for mass, axial momentum, radial momentum, energy, and species are written as:

$$\frac{\rho}{P}\frac{\partial p}{\partial t} - \frac{\rho}{T}\frac{\partial T}{\partial t} - \rho\overline{W}\sum_k \frac{1}{W_k}\frac{\partial Y_k}{\partial t} + \frac{\partial}{\partial x}(\rho u) + 2\rho V = 0, \tag{2.5}$$

$$\rho\frac{\partial u}{\partial t} + \rho u\frac{\partial u}{\partial x} + \frac{\partial p}{\partial x} - 2\mu\frac{\partial V}{\partial x} - \frac{4}{3}\frac{\partial}{\partial x}\left(\mu\frac{\partial u}{\partial x}\right) + \frac{4}{3}\frac{\partial}{\partial x}(\mu V) = 0, \tag{2.6}$$

$$\rho\frac{\partial V}{\partial t} + \rho u\frac{\partial V}{\partial x} + \rho V^2 - \frac{\partial}{\partial x}\left(\mu\frac{\partial V}{\partial x}\right) + \Lambda = 0, \tag{2.7}$$

$$\rho c_p\frac{\partial T}{\partial t} + \rho c_p u\frac{\partial T}{\partial x} - \frac{\partial}{\partial x}\left(\lambda\frac{\partial T}{\partial x}\right) - \frac{\partial p}{\partial t} + \rho(\sum_k c_p Y_k V_k)\frac{\partial T}{\partial x} + \sum_k h_k W_k\omega_k = 0, \tag{2.8}$$

$$\rho\frac{\partial Y_k}{\partial t} + \rho u\frac{\partial Y_k}{\partial x} + \frac{\partial}{\partial x}(\rho Y_k V_k) - W_k\omega_k = 0, \quad k = 1, \cdots, K \tag{2.9}$$

The main difference between the present formulation and the previous steady problem [44] is the decomposition of the pressure (P) into the thermodynamic pressure (p_0) and acoustic pressure (p) as, $P = p_0 + p$. This is found to relieve the temporal stiffness arising from fast transients experienced in unsteady simulations. The equation of state then becomes

$$\rho = (p + p_0)\,\overline{W}/RT. \tag{2.10}$$

The radial pressure-curvature eigenvalue,

$$\Lambda(t) = \frac{1}{r}\frac{\partial p}{\partial r}, \tag{2.11}$$

is a time-dependent variable that is determined as part of the solution. The above system of equations is subject to the boundary conditions

$$\begin{aligned} x = 0: \quad & u = u_0(t), \quad V = V_0(t), \quad T = T_0(t), \quad Y_k = (Y_k)_0(t), \\ x = L: \quad & u = u_L(t), \quad V = V_L(t), \quad T = T_L(t), \quad Y_k = (Y_k)_L(t). \end{aligned} \tag{2.12}$$

In particular, in Chapters 4 and 5, the following form the $V_0(t)$ and $V_L(t)$ is used:

$$V_0(t) = V_{init}(1 + A\sin(2\pi f t)) = -V_L(t) \tag{2.13}$$

where V_{init} is the initial velocity, and A and f are the amplitude and frequency of velocity oscillation, respectively.

2.2.2 Numerical method

The unsteady opposed flame simulation is performed using the OPUS code, developed by Im *et al.* [47]. Equations (2.5) – (2.9) result in a system of differential-algebraic equations (DAE), which is solved numerically using DASPK [48]. A fully converged steady solution field obtained using modified version of OPPDIF [45] is used as the initial condition. The OPUS code is interfaced with CHEMKIN [42] and TRANSPORT [49] packages for computing detailed reaction rates, thermodynamic properties, and transport properties.

The DAE system formed by equations (2.5) – (2.9) along with the algebraic boundary conditions (2.12) has an index[1] of 3. This high index of the DAE system makes the system extremely stiff when the time-dependent boundary condition has frequency of a

[1] The index of a DAE system is the number of differentiations required to transform it into a system of ordinary differential equations. A DAE with a higher index is stiffer.

few thousand hertz. To alleviate this problem, the boundary condition is specified in its time-derivative form, tantamount to specifying the boundary conditions on u', V', T' and Y_k'. Here $'$ represents derivative with respect to time. This reduces the index and helps to substantially reduce the computation time required for the simulations.

2.3 KIVA-3v

KIVA is a FORTRAN program developed at Los Alamos National Laboratory over many years [50, 51] and is used extensively for internal combustion engine simulations [11, 25]. It can simulate two- or three-dimensional chemically reactive fluid flows with sprays. It is applicable to laminar or turbulent flows, subsonic or supersonic flows, and single-phase or dispersed two-phase flows. For turbulent flows it uses a RANS based solver. The underlying governing equations are given elsewhere [50] and are not shown here for brevity. The details of the spray model are also given in Ref. [50]. KIVA-3v uses a multi-block structured mesh and engine geometries containing complex inlet and outlet ports as well as vertical or canted valves can be modeled. In Chapter 6, KIVA-3v is used to model non-reacting flow in a 3D pentroof engine, to investigate turbulent mixing characteristics. Standard $k-\epsilon$ turbulence closure model is employed.

The numerical solution procedure for gas-phase is based on a finite volume method called the ALE (Arbitrary Lagrangian Eulerian) method [52, 53]. Spatial differences are formed on a finite-difference mesh that subdivides the computational region into a number of small cells that are hexahedrons. An operator splitting scheme is used to solve the governing equations. Further details of the numerical algorithm are given elsewhere [50].

2.4 Compressible Reacting Flow DNS

DNS is an important simulation tool as it is free from turbulence closure modeling assumptions, and therefore, provides a high-fidelity description of the complex turbulent reacting

flow system. In Chapter 7, DNS of a constant volume H_2-air mixture is conducted to investigate its autoignition characteristics in presence of mixture inhomogeneities. The mathematical formulation for the compressible reacting flow is described in detail elsewhere [54, 55]. The S3D code, originally developed at Sandia National Laboratories, Livermore, CA, is used for solving the full set of compressible Navier-Stokes, species, and energy equations for a reacting gas mixture. A fourth-order Runge-Kutta method for time integration and an eight-order explicit spatial difference scheme [56, 57] is employed. Detailed H_2-air chemical mechanism with 9 chemical species and 22 reactions developed by Mueller *et al.* [58] is used. Thermal conductivity, λ, is given as a function of temperature following Smooke and Giovangigli [59]. The mixture specific heat C_p is a function of local mixture composition, $C_p = \sum_k C_{p,k} Y_k$, where each $C_{p,k}$ is curve-fitted as a function of temperature using the CHEMKIN thermodynamic database [60]. The molecular viscosity is temperature dependent and constant Lewis numbers for individual species are used. The details of the computational mesh and the initial and boundary conditions are given in Chapter 7.

Chapter 3

Autoignition of Homogeneous H_2-Air Mixture subjected to Unsteady Temperature Fluctuations

In this Chapter, the effects of unsteady temperature fluctuation on the autoignition of homogeneous constant-volume hydrogen/air mixture is studied computationally with detailed chemical kinetics and theoretically using asymptotic analysis. As mentioned in the Introduction Chapter, this study is the first step towards understanding the complex interaction between turbulence and autoignition behavior that may exist in LTC engines. Turbulence has two folds effects on autoignition: It leads to fluctuations of scalars such as temperature which directly effect the reaction rate, and it also leads to fluctuations in scalar dissipation rate which results in fluctuations of transport losses of heat/radicals from the ignition kernel. By using a homogeneous configuration, we can isolate the former effect and study it seperately. Moreover, relevance of such a simplified model to practical LTC engine application can be further justified based on the following aspects. For both premixed or nonpremixed systems, the ignition kernel may be approximated as a homogeneous mixture pocket subjected to heat and mass transport with the surroundings, such that the subsequent evolution of the ignition event may be described by a Lagrangian description of an ignition kernel whose uniform thermodynamic conditions undergo temporal variations during the ignition delay period. The study is also of relevance from the point of view of fundamental combustion science as it attempts to build upon the classical Semenov's explosion criterion [61].

The governing equations and the functional form of imposed temperature oscillation

are given in Chapter 2. For computational solution, detailed hydrogen reaction mechanism [62] with 9 species and 19 reactions is used. This mechanism is same as the one used by previous related studies of hydrogen autoignition [21, 63]. Also the same rate constants were used in the reduced mechanism in Ref. [64], and the same will be used for the asymptotic analysis in high temperature regime to be presented in Section 3.1.2. In the following, the two distinct regimes of hydrogen autoignition: high temperature and low temperature ignition regimes, are described, and then asymptotic analysis is conducted using different methodologies in the two regimes to obtain closed formed solutions of ignition delay. Subsequently, the results from asymptotic analysis are compared with those obtained using direct numerical integration using detailed chemistry. Finally, physical explanations for the observed results are sought.

It is well known (see for example [65]) that the ignition behavior of a hydrogen-oxygen system is characterized by two distinct chemical paths depending on the relative dominance between the two competing reaction steps:

$$\mathrm{H} + \mathrm{O_2} = \mathrm{O} + \mathrm{OH} \tag{R1}$$

$$\mathrm{H} + \mathrm{O_2} + \mathrm{M} = \mathrm{HO_2} + \mathrm{M} \tag{R9}$$

where the reaction number follows that in Ref. [62]. The crossover temperature, T^*, is defined as the temperature at which the rates of R1 and R9 becomes equal, and is a function of pressure. In the high temperature regime ($T > T^*$), ignition is characterized by the chemical branching with little thermal feedback. In the low temperature regime ($T < T^*$), R9 dominates and ignition is caused by the accumulation of HO_2 which in turn leads to eventual chain branching through:

$$\mathrm{HO_2} + \mathrm{H_2} = \mathrm{H_2O_2} + \mathrm{H} \tag{R17}$$

$$H_2O_2 + M = OH + OH + M \tag{R15}$$

The ignition process in the low temperature regime involves a larger thermal feedback than in the high temperature regime. Therefore, in an attempt to derive closed-form solutions, a different analysis is needed for each regime in order to account for the distinct chemical and thermal characteristics. Description of the asymptotic analysis for both regimes are given as follows.

3.1 Asymptotic Analysis

3.1.1 Low Temperature Regime

In this regime, induction period for chemical branching is comparable and coupled with thermal induction process. Therefore, it is expected that the ignition behavior in response to imposed temperature fluctuations can be described by a thermal explosion problem with simple chemistry. We first define nondimensional variables as $\widetilde{T} = (c_v\rho_0/Q_c c_{F,0})T = (c_v/q_c Y_{F,0})T$ for temperature and $\widetilde{c_F} = c_F/c_{F,0}$ for the molar fuel concentration, where c_v is the specific heat at constant volume, Q_c is the heat of combustion, and subscript 0 denotes the initial condition. A proper nondimensionalization for the time variable will be determined in the following through the analysis. The governing equations for one-step overall reaction in a constant volume reactor are derived as:

$$\frac{d\tilde{T}}{dt} = B\tilde{c}_F exp(-\tilde{T}_a/\tilde{T}) + \frac{d\tilde{T}_I}{dt} \tag{3.1}$$

$$\frac{d\tilde{c}_F}{dt} = -B\tilde{c}_F exp(-\tilde{T}_a/\tilde{T}) \tag{3.2}$$

where B and T_a are appropriately chosen pre-exponential factor and activation temperature of the global reaction step respectively. $\tilde{T}_I(t)$ is the imposed unsteady temperature oscillation given in Eq. (2.3). In the present study, we will only consider a small amplitude temperature oscillation, such that amplitude of temperature oscillation, $A = O(\epsilon)$, where

$\epsilon = \tilde{T}_0^2/\tilde{T}_a$ is a small parameter to be used in the asymptotic expansion. This is considered a reasonable assumption because in most practical LTC engines there is sufficient time for mixing prior to ignition phase.

Equations (3.1) and (3.2) can be combined by defining the coupling function:

$$\frac{d}{dt}(\tilde{T} - \tilde{T}_I + \tilde{c_F}) = 0 \tag{3.3}$$

which can be easily integrated with the initial condition of $(\tilde{T} - \tilde{T}_I)_{t=0} = 0$ and $(\tilde{c}_F)_{t=0} = 1$:

$$\tilde{T} - \tilde{T}_I = 1 - \tilde{c}_F. \tag{3.4}$$

To determine the ignition criterion, we consider a small temperature perturbation with respect to the imposed oscillatory temperature:

$$\tilde{T} - \tilde{T}_I = \epsilon\theta(t) + O(\epsilon^2) \tag{3.5}$$

with the initial condition of $\theta(0) = 0$. Equations (3.4) and (3.5) imply that

$$\tilde{c}_F = 1 - \epsilon\theta + O(\epsilon^2) \tag{3.6}$$

suggesting that the reactant consumption is negligible during the induction period. Substituting Equation (3.5) into (3.1) and using the Taylor expansion for the terms inside the exponential function for $A \ll 1$ and $\epsilon \ll 1$, the leading order equation is derived as:

$$\frac{d\theta}{dt} = \frac{B}{\epsilon} e^{-T_a/T_0} e^{\theta} e^{(\tilde{T}_I - \tilde{T}_0)/\epsilon}. \tag{3.7}$$

In the absence of the imposed temperature fluctuation, $\tilde{T}_I = \tilde{T}_0$, and the equation degenerates to the classical homogeneous explosion problem [61], for which the ignition delay is $t_{ign}^0 = \epsilon/(Be^{-T_a/T_0})$. This introduces an appropriate way to nondimensionalize the time

variable as $\tilde{t} = t/t^0_{ign}$, such that Equation (3.7) becomes:

$$\frac{d\theta}{d\tilde{t}} = e^{\theta} e^{(\tilde{T}_I - \tilde{T}_0)/\epsilon}. \tag{3.8}$$

Equation (3.8) can be integrated with the initial condition $\theta(\tilde{t} = 0) = 0$ to yield

$$\theta = -ln(1 - I(\tilde{t})) \tag{3.9}$$

where

$$I(\tilde{t}) = \int_0^{\tilde{t}} e^{(\tilde{T}_I - \tilde{T}_0))/\epsilon} d\tilde{t} \tag{3.10}$$

Ignition is identified as time at which $\theta \to \infty$, which occurs as $I(\tilde{t}) \to 1$. Therefore, the integral equation $I(\tilde{t}) = 1$ is solved to determine the ignition delay $\tilde{t}_{ign}$. It is interesting to note that the well-known Semenov's classic homogeneous explosion analysis [61] can be extended to account for imposed unsteady oscillations in temperature by a simple modification in the formula.

Since the asymptotic analysis uses a one-step chemistry, the effective activation temperature must be determined. This is done by computing homogeneous ignition cases with detailed hydrogen/air mechanism [62] at various initial temperatures, and curve-fitting the slope of $\ln t_{ign}$ versus $1/T_0$. The activation temperature is found to be 25,000 K for the initial pressure of 10 atm. The integral equation is computed numerically, and the results will be compared with the results of direct calculations with detailed chemistry in Section 3.2.

3.1.2 High Temperature Regime

When $T > T^*$, ignition is described primarily by the chain branching mechanism dominated by (R1). When the temperature is moderately higher than T^*, the competition by (R9) in consumption of the H radical becomes a key factor that determines the overall ignition response. Following previous studies [64, 66, 67], the radical-induced ignition process

is analyzed based on the 3-step reduced mechanism:

$$\mathrm{I} : 3\mathrm{H_2} + \mathrm{O_2} = 2\mathrm{H} + 2\mathrm{H_2O},\ \omega_{\mathrm{I}} = \omega_{1\mathrm{f}} \tag{3.11}$$

$$\mathrm{II} : \mathrm{H} + \mathrm{O_2} + \mathrm{M} = \mathrm{HO_2} + \mathrm{M},\ \omega_{\mathrm{II}} = \omega_9 \tag{3.12}$$

$$\mathrm{III} : \mathrm{H_2} + \mathrm{O_2} = \mathrm{H} + \mathrm{HO_2},\ \omega_{\mathrm{III}} = \omega_{10\mathrm{b}} \tag{3.13}$$

The reaction rate constants for ω_{1f}, ω_9 and ω_{10b} are taken from Ref. [62]. The contribution from step III is usually very small but it is necessary to initiate the ignition. The ignition behavior of this system is described by the evolution of the H radical, whose governing equation is written in dimensional form as:

$$\begin{aligned}
\rho\frac{dY_H}{dt} &= W_H\sum_k(\nu''_{ik}-\nu'_{ik})\omega_k \\
&= W_H(2\omega_{1f}-\omega_9+\omega_{10b}) \\
&= W_H(2k_{1f}[\mathrm{H}][\mathrm{O_2}]-k_9[\mathrm{H}][\mathrm{O_2}][\mathrm{M}]+k_{10b}[\mathrm{H_2}][\mathrm{O_2}]) \\
&= W_H\left\{2k_{1f}\rho^2\frac{Y_H}{W_H}\frac{Y_{O_2}}{W_{O_2}}-k_9\rho^2\frac{Y_H}{W_H}\frac{Y_{O_2}}{W_{O_2}}[\mathrm{M}]+k_{10b}\rho^2\frac{Y_{H_2}}{W_{H_2}}\frac{Y_{O_2}}{W_{O_2}}\right\} \\
&= \rho^2\frac{Y_{O_2}}{W_{O_2}}k_{1f}(2-\kappa)Y_H+\rho^2\frac{W_H}{W_{H_2}W_{O_2}}k_{10b}Y_{H_2}Y_{O_2} \\
&= \Delta_{\mathrm{I}}(t)Y_H+\Delta_{\mathrm{II}}(t)
\end{aligned} \tag{3.14}$$

where

$$\begin{aligned}
\Delta_{\mathrm{I}}(t) &= \rho^2\frac{Y_{O_2}}{W_{O_2}}k_{1f}(2-\kappa) : \text{chain branching termination} \\
\Delta_{\mathrm{II}}(t) &= \rho^2\frac{W_H}{W_{H_2}W_{O_2}}k_{10b}Y_{H_2}Y_{O_2} : \text{chain initiation} \\
\kappa &= \frac{k_9[\mathrm{M}]}{k_{1f}}
\end{aligned}$$

Equation (3.14) can be integrated to determine Y_{H}:

$$Y_H(t) = e^{\int_0^t \Delta_{\mathrm{I}}(t)dt} \int_0^t \Delta_{\mathrm{II}}(t) e^{-\int_0^{t'} \Delta_{\mathrm{II}}(t')dt'} dt \tag{3.15}$$

Throughout the ignition process, the thermal feedback need not be considered in this high-temperature regime. Nonetheless, the effect of temperature fluctuation is manifested through the fluctuations in reaction rate of the radical pool formation. As such, a proper definition of ignition based on H radical buildup is needed in contrast to the thermal run-away criterion adopted in the low temperature regime analysis. Following Im *et al.* [66], ignition is defined to occur at the time at which the H radical builds up to:

$$Y_H = O\left(\epsilon_h \frac{2-\kappa}{q_{\mathrm{I}} + \kappa q_{\mathrm{II}}}\right), \tag{3.16}$$

such that the ignition delay is determined by solving the following integral equation:

$$e^{\int_0^{t_{ig}} \Delta_{\mathrm{I}}(t)dt} \int_0^{t_{ig}} \Delta_{\mathrm{II}}(t) e^{-\int_0^{t'} \Delta_{\mathrm{II}}(t')dt'} dt = \epsilon_h(t_{ig}) \frac{2-\kappa(t_{ig})}{q_{\mathrm{I}} + \kappa(t_{ig}) q_{\mathrm{II}}} \tag{3.17}$$

where $\epsilon_h = \tilde{T}^2/\tilde{T}_{a,I}$, and $\tilde{T}_{a,I}$ is the non-dimensional activation temperature of reaction I. Temperature is non-dimensionalized using the heat of combustion and specific heat. q_{I} and q_{II} are the fractional enthalpy release for reactions I and II, respectively ($q_{\mathrm{I}} + q_{\mathrm{II}} = 1$). Equation (3.17) is solved numerically and the results of ignition delay are presented in comparison with those from direct numerical integration with detailed chemistry in the next section.

3.2 Results and Discussion

For all the parametric studies, the initial temperature, T_0, is fixed at 1000K, and the initial system pressure, p_0, is varied in order to explore the behavior in two distinct ignition regimes. For the reaction mechanism used [62], the crossover pressure is found to be at p^*

= 2.3 atm. For both ignition regimes, the initial equivalence ratio of the mixture is fixed at 0.1, and the amplitude of the temperature oscillation is set at $A = 0.02$, which is equivalent to the actual temperature variation by $\pm$20 K. In the following, the results of asymptotic analysis will first be validated against numerical results, in terms of the ignition delay as a function of the frequency of the temperature oscillation. Subsequently, detailed examinations will be given in order to explain the observed ignition delay behavior for both ignition regimes.

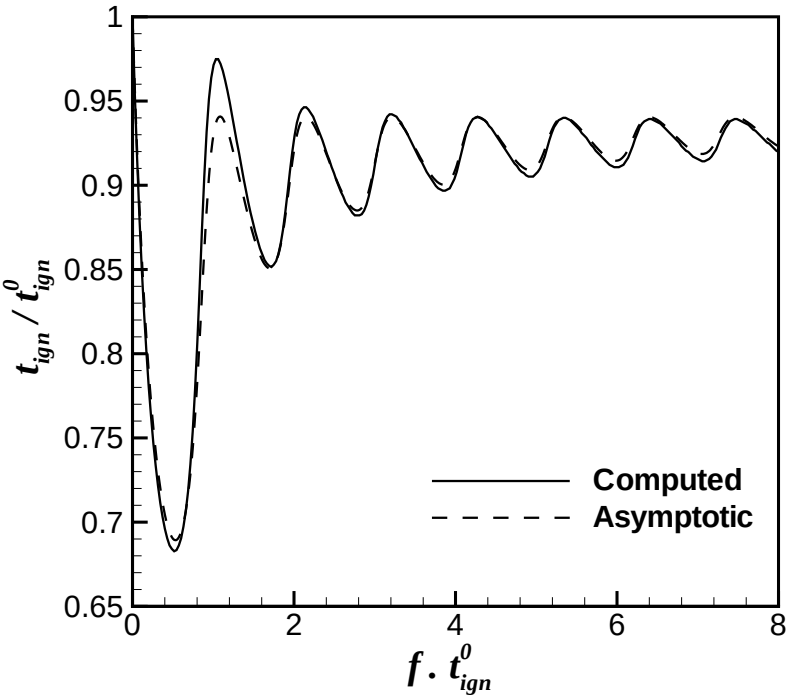

Figure 3.1: Non-dimensional ignition delay as a function of non-dimensional frequency of temperature oscillation for the low temperature regime, for $T_0 = 1000$ K and $p_0 = 10$ atm. Results from the asymptotic analysis and direct numerical integration are compared.

3.2.1 Comparison of Analytical and Numerical Results

For $T_0 = 1000$K and $A = 0.02$, the comparisons between analytical and numerical predictions of the ignition delay are conducted for the low and high temperature regimes. Figs. 3.1 and 3.2 show the comparison of the ignition delay as a function of the imposed

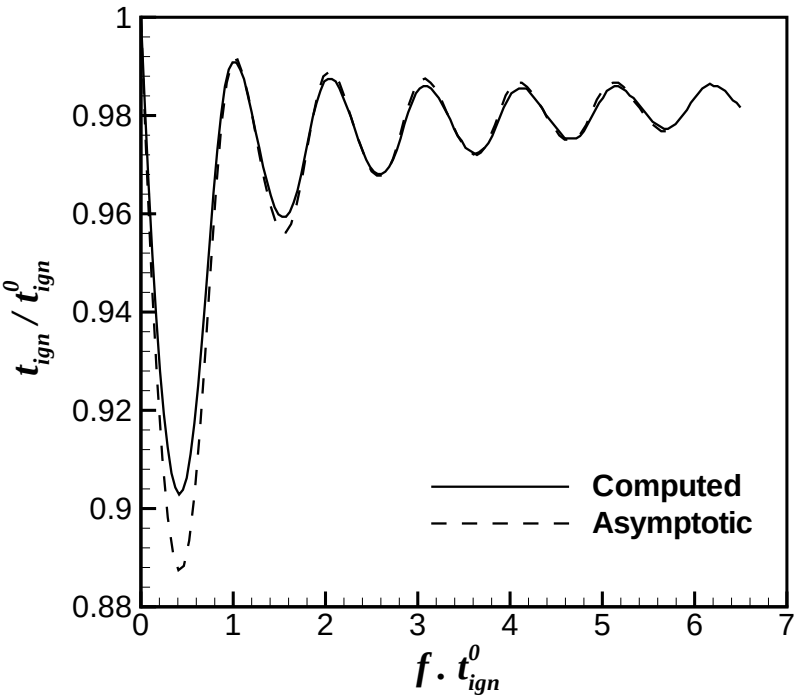

Figure 3.2: Non-dimensional ignition delay as a function of non-dimensional frequency of temperature oscillation for the high temperature regime, for $T_0 = 1000$ K and $p_0 = 0.01$ atm. Results from the asymptotic analysis and direct numerical integration are compared.

frequency for $p_0 = 10$atm ($T < T^*$) and $p_0 = 0.01$atm ($T > T^*$), respectively. In both the figures, ignition delay and frequency are non-dimensionalized with the reference ignition delay (ignition delay for f = 0 Hz). In the high temperature regime, the reference ignition delay is somewhat different for asymptotic analysis and detailed computation (t^0_{ign} = 11.4 msec and 20.69 msec respectively). Therefore, in Fig. 3.2 their respective reference ignition delays are used to non-dimensionalize ignition delay and frequency. To be consistent with the asymptotic analysis, the ignition delay for numerical calculations is defined as time upto maximum rate of growth of $Y_{\rm H}$ for the low temperature ignition regime, and the time required for $Y_{\rm H}$ to reach a value of 0.0003 for high temperature ignition regime. For both ignition regimes, the ignition delay shows a harmonic response to the imposed frequency, while the amplitude in the excursion gradually damps out as the frequency in-

creases. Another interesting observation is that for both the regimes igntion delay for any frequency of temperature oscillation is less than the reference ignition delay for the steady case, i.e. ignition is always enhanced if the temperature of the mixture is oscillated in the prescribed way. The asymptotic results for both regimes capture this behavior with excellent agreement, thereby verifying that the dominant driving mechanism for ignition in the low temperature (thermal runaway) and high temperature (radical runaway) regimes are properly accounted for. While the two figures exhibit qualitatively similar behavior, it is noted that the ignition delay excursion in the low temperature regime is found to be more sensitive to the same level of temperature fluctuation: the largest reduction in the ignition delay during the first harmonic is approximately 30% (for the low temperature regime) and 10% (for the high temperature regime). This further confirms that the low temperature ignition regime is driven by thermal feedback and thus is more sensitive to the fluctuations in the mixture temperature.

3.2.2 Unsteady Ignition Response

The previous section demonstrated that ignition characteristics in the low and high temperature regimes are properly simplified by capturing the essential chemical and/or thermal mechanisms. While Equations (3.10) and (3.17) provide convenient closed-form solutions to the ignition criteria for a wide range of parameters, more in-depth analysis is required in order to explain the observed ignition delay response shown in Figs. 3.1 and 3.2. Therefore, the following results were generated by direct numerical integration of the equations with detailed chemistry. Only the low temperature regime will be discussed here, as we have found that the same explanation applies to the ignition behavior in the high temperature regime.

First, to assess the effect of the system pressure, computation was carried out at various initial pressures: p_0 = 10, 15, 20, and 25 atm, for which the reference ignition delay is found to be t_{ign}^0 = 14.34, 12.05, 10.29, and 8.975 msec, respectively. Fig. 3.3 shows

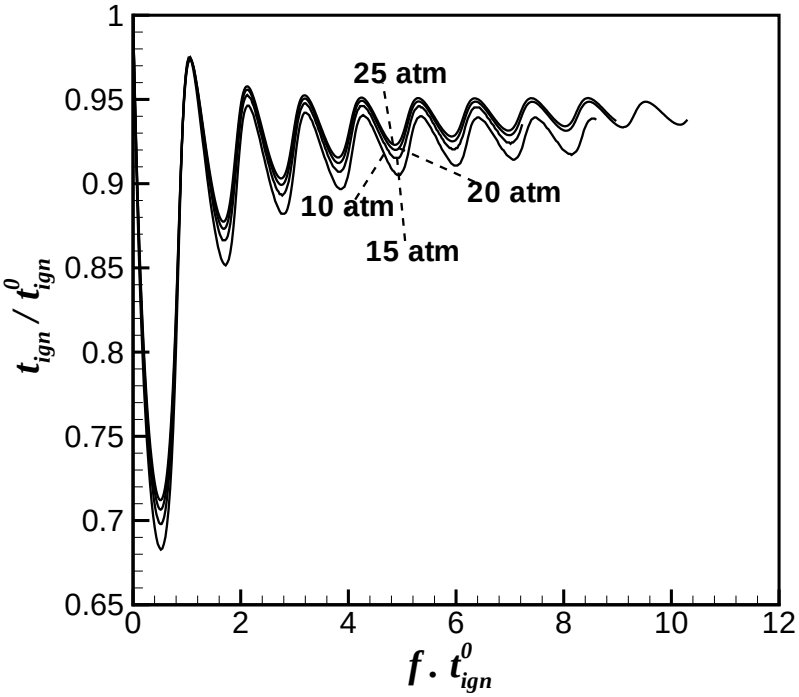

Figure 3.3: Non-dimensional ignition delay as a function of non-dimensional frequency at various initial pressures in the low temperature regime.

the plots of non-dimensional ignition delay against non-dimensional frequency for the four different pressure cases. Apart from slight quantitative differences, the harmonic response and damping behavior collapse very well for a wide range of pressure. As the pressure increases, the curves approach an asymptotic limit because the system is further away from the crossover condition at which the competition between the branching (R1) and termination (R9) reactions become pronounced.

Next, explanation of the observed unsteady ignition behavior is sought. When the system temperature fluctuates during the ignition event, one might first conjecture that the resultant ignition delay may be related to the average temperature during the induction period prior to ignition. To verify this postulate, the mean temperature up to ignition is determined by:

$$T_{mean} = \frac{1}{t_{ign}} \int_0^{t_{ign}} T dt \tag{3.18}$$

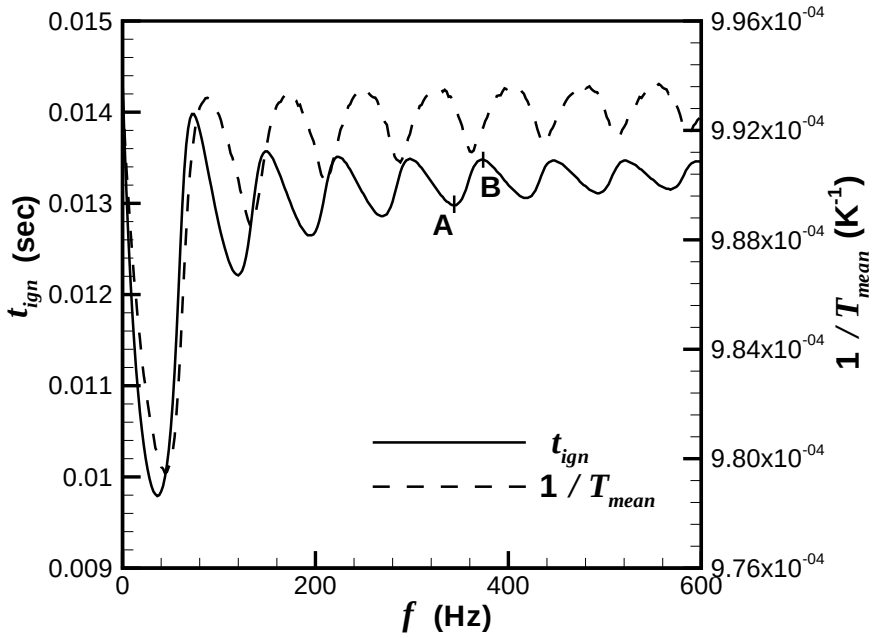

Figure 3.4: Ignition delay (left axis) and $1/T_{mean}$ (right axis) as a function of frequency for $p_0 = 10$ atm.

Figure 3.4 shows the ignition delay and the inverse of the mean temperature as a function of frequency for $p_0 = 10$ atm. For the postulate to be valid, the two curves must be in phase at all frequencies. The results show that this is the case only during the first harmonic. In other words, the ignition behavior correlates strongly with the cumulative temperature history only up to the first harmonic, that is, if ignition occurs before the harmonic temperature oscillation completes one cycle. In fact, for higher frequencies it can be seen that the two curves become totally out of phase. To further substantiate this point, another set of computations was done for the case of p_0 = 10 atm, but now the temperature oscillation is 180 degrees out of phase compared to that given in Eq. (2.3). In other words, now in the first cycle temperature first decreases and subsequently increases. The ignition delay results for various frequencies together with $(T_{mean})^{-1}$ are shown in Fig. 3.5. Again, it is seen that

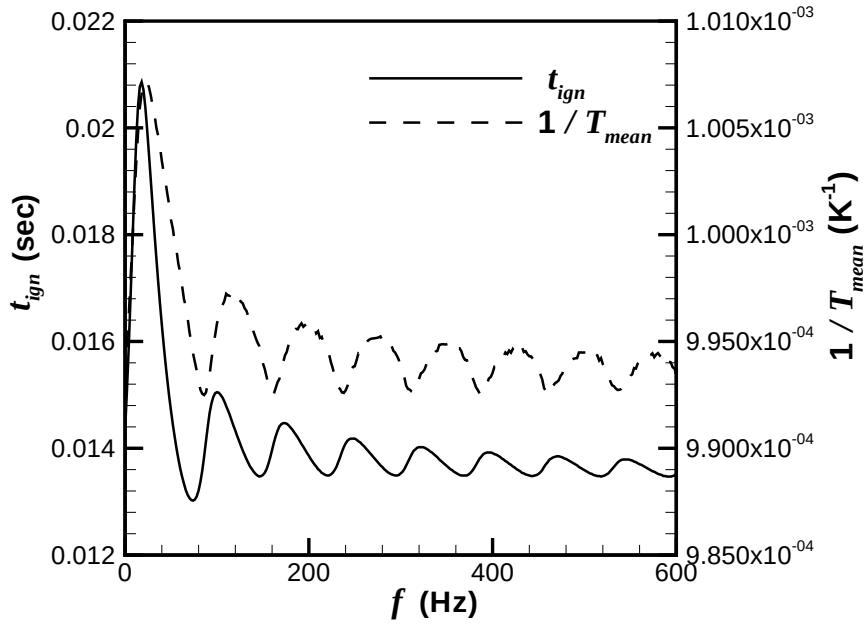

Figure 3.5: Ignition delay (left axis) and $1/T_{mean}$ (right axis) as a function of frequency for $p_0 = 10$ atm (with the phase of temperature oscillation shifted by 180 degrees).

ignition delay correlates with inverse of mean temperature only for the first harmonic.

For all frequencies larger than the first harmonic, the ignition delay response is rather uncorrelated with $1/T_{mean}$. In these cases, an alternative explanation is required. To this end, we inspect the instantaneous gradient of temperature excursion near the onset of ignition. As representative cases, we pick two frequencies, f = 344 and 374 Hz (points marked by A and B respectively, in Fig. 3.4), at which t_{ign} reaches the trough and peak values, respectively. Figure 3.6 shows the time evolution of temperature and mass fraction of H species, which is the key radical species that demarcates ignition, for the two frequencies. The sharp peaks in H mass fraction and the steep temperature rise that occur at ignition are a characteristic of low temperature ignition which is dictated by thermal runaway; for high temperature ignition, the temperature rise is more gradual. The evolution of

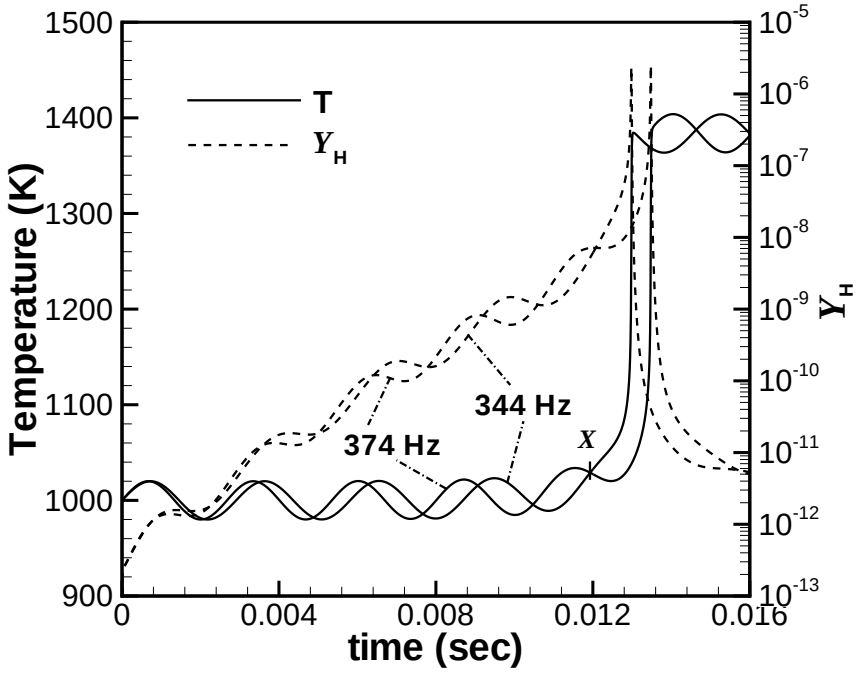

Figure 3.6: Temporal evolution of temperature and Y_{H} for f = 344 Hz and f = 374 Hz, for $T_0 = 1000$ K and $p_0 = 10$ atm

Y_{H} (shown in log scale) indicates that the cumulative effect of temperature fluctuations is of little significance during a large fraction of the induction period because the radical pool develops in an exponential manner. Instead, when the temperature oscillation undergoes a number of cycles during the induction period, the chemical-thermal runaway behavior is dominated by the temperature gradient near the onset of ignition when the mixture is highly reactive with the formation of radical pool. Comparing the two frequency cases, it is evident that the instantaneous temperature gradient of the temperature excursion just prior to ignition (at point marked X in Fig. 3.6) appears almost opposite ($dT/dt > 0$ for 344 Hz and $dT/dt < 0$ for 374 Hz), despite the similarities in the cumulative average of the temperature throughout the bulk of the induction period.

To be specific and quantitative, for a range of frequencies we monitored the temporal gradient of temperature, dT/dt, at a half cycle prior to ignition, $t_{crit} = t_{ign} - 0.5/f$. Fig. 3.7

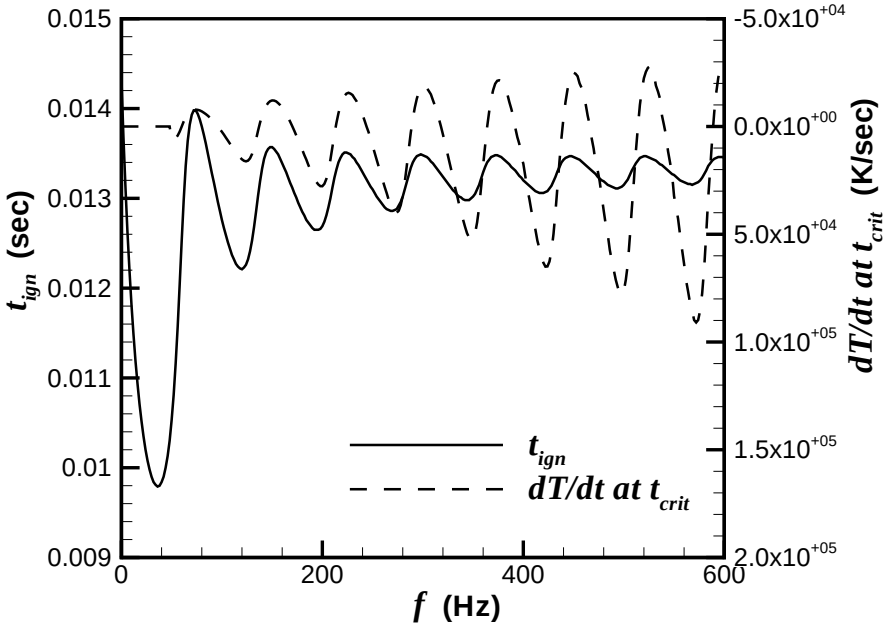

Figure 3.7: Ignition delay and dT/dt at t_{crit} (axis reversed) as a function of frequency for $T_0 = 1000$ K and p_0 = 10 atm

.

shows the plot of dT/dt measured at t_{crit} as a function of frequency, plotted together with ignition delay. The axis for dT/dt is reversed such that $dT/dt > 0$ would correlate with the reduction in the ignition delay. Except for the first harmonic, the two curves are found to be completely in phase, thereby demonstrating that the ignition behavior is determined by the instantaneous temperature gradient at the onset of ignition.

To summarize, effects of unsteady temperature fluctuation on autoignition of homogeneous hydrogen/air mixture were studied computationally and also theoretically. Excellent agreement was obtained between computational results with detailed chemistry and theoretical results using asymptotic analysis. For low frequencies (frequencies less than the first harmonic of ignition delay response), ignition behavior is quasi-steady and correlates

well with the cumulative mean temperature in the induction period. Whereas, for higher frequencies, ignition delay correlates well with instantaneous temperature gradient of the imposed temperature oscillation at the onset of ignition.

Having understood the direct effects of temperature fluctuation on the autoignition behavior in a homogeneous reactor configuration, in the next two Chapters we study the effects of fluctuations in scalar dissipation rate on autoignition behavior. Hydrogen and n-heptane autoignition are studied in Chapters 4 and 5, respectively.

Chapter 4

Effects of Unsteady Scalar Dissipation Rate on Nonpremixed Hydrogen/Air Autoignition

In this Chapter, the effects of scalar dissipation rate fluctuation on the autoignition of a nonpremixed hydrogen/air mixture is studied using detailed chemistry in a counterflow configuration. In particular, the response of ignition delay to the frequency of scalar dissipation rate fluctuation is sought. As mentioned in the Introduction, this study is based on the viewpoint that the turbulent eddies at different scales have different characteristic $timescales$; smaller eddies, which are often more effective in influencing the ignition kernels, are at shorter time scales such that one may need to consider multiple repeated attacks of such eddies during the ignition delay. The study thus helps in improving the understanding of turbulence-autoignition interaction. The primary objective of this study is to obtain a unified description of ignition delay response to the unsteadiness in scalar dissipation rate.

Detailed hydrogen mechanism with 19 reactions and 9 species [62] is used in this study. For all the results presented in this study, H_2 (50 $\%$) diluted with N_2 (50 $\%$) is supplied from one nozzle, impinging against air (N_2 - 79 $\%$ and O_2 - 21 $\%$) stream from the other nozzle 0.5 cm apart. The pressure is fixed to 2 atm. Fuel side temperature is fixed to 300 K and air side temperature is fixed to 1020 K. The crossover temperature, at which the rates of branching and termination reactions are equal [65], is found to be 985 K at this pressure. The imposed oxidizer temperature results in the ignition kernel temperature higher than the crossover value, and therefore the condition corresponds to that of high temperature ignition regime.

To compute the ignition delay, a nonreactive steady solution is first obtained while suppressing all reaction rates. This generates a converged initial solution for the unsteady computation. The unsteady calculation is then performed with reactions turned on at t = 0. Temporal fluctuation of the scalar dissipation rate is imposed by oscillating the velocity at the nozzle inlet sinusoidally. The functional form of velocity oscillation at the nozzle is given in Eq. 2.13 of Chapter 2. In the following we first study autoignition behavior in a steady scalar dissipation rate field. Subsequently, effects of unsteady scalar dissipation rate are studied.

4.1 Ignition Response to Steady Scalar Dissipation Rate

As a reference, the response of the ignition delay to steady scalar dissipation rate is first studied. In this case, the velocity at the nozzle is fixed constant. For all the results presented in this study, mixture fraction is defined using Bilger's [68] definition as:

$$Z = \frac{Y_{\mathrm{H}}/2W_{\mathrm{H}} - (Y_{\mathrm{O}} - Y_{\mathrm{O,air}})/W_{\mathrm{O}}}{Y_{\mathrm{H,fuel}}/2W_{\mathrm{H}} + Y_{\mathrm{O,air}}/W_{\mathrm{O}}} \tag{4.1}$$

and the scalar dissipation rate is defined as:

$$\chi = 2D\left(\frac{\partial Z}{\partial x}\right)^2 \tag{4.2}$$

where D is the thermal diffusivity. For this Chapter, unless stated otherwise, the scalar dissipation rate (χ) is determined at the ignition kernel, which is defined as the location of the maximum heat release rate. The onset of ignition is defined as the instant at which rate of change of the peak temperature in the domain becomes maximum.

Figure 4.1 shows the ignition delay and maximum steady state OH mass fraction in the domain as a function of the nozzle inlet velocity. The solid line in maximum Y_{OH} plot represents the computed lower branch of the standard S-curve of flame response. The dashed line in the same plot shows the hand-drawn continuation of lower branch to unstable

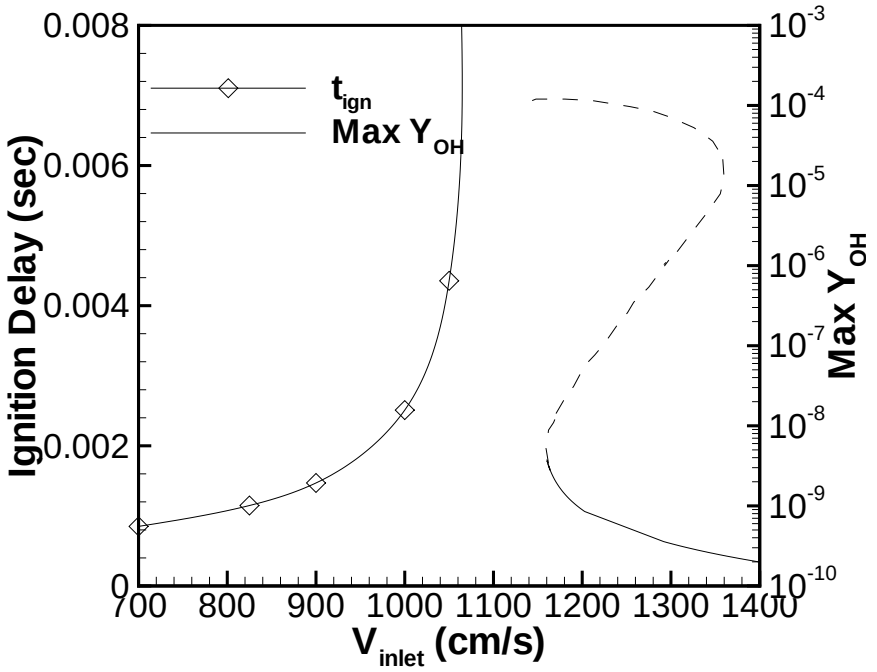

Figure 4.1: Ignition delay and max Y_{OH} as a function of velocity at nozzle inlet

and fully burning branches. The inlet velocity gives a measure of scalar dissipation rate determined at the ignition kernel. As the inlet velocity is decreased, the frozen steady state solution reaches the steady turning point near the velocity at 1155 cm/s. At this steady ignition limit, the corresponding scalar dissipation rate at the ignition kernel is found to be χ_s^* = 47 s^{-1}, where subscript s denotes the steady limit. The mixing layer is ignitable for $\chi < \chi_s^*$. If this condition is met, the ignition delay gradually increases as χ increases as a result of increased loss of radicals and heat from the ignition kernel. Note that ignition delay plotted on the left axis is obtained from the unsteady computation, whereas the maximum OH mass fraction plotted on the right axis is obtained from steady computation. These ignition results under the steady scalar dissipation rate conditions will be used to explain the results for unsteady scalar dissipation rate cases to be presented in the next section.

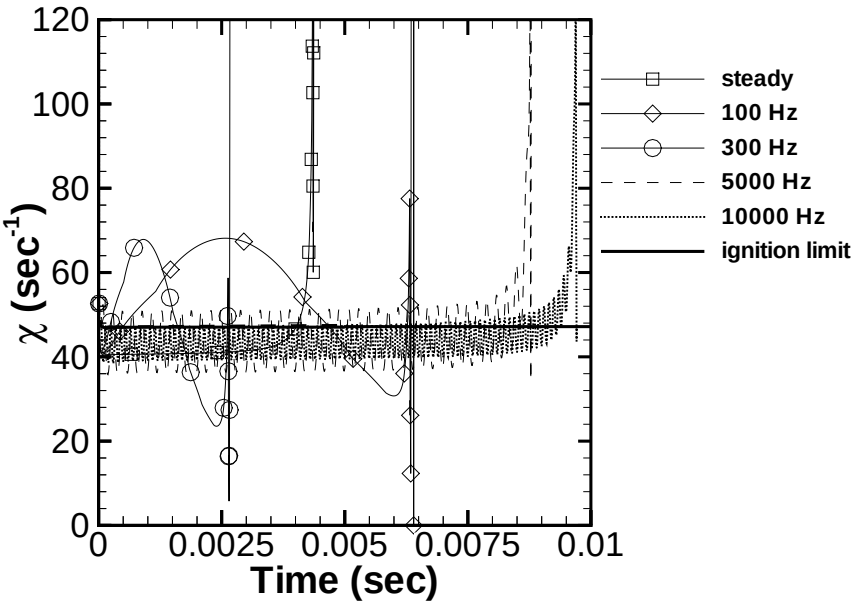

(a) Case A

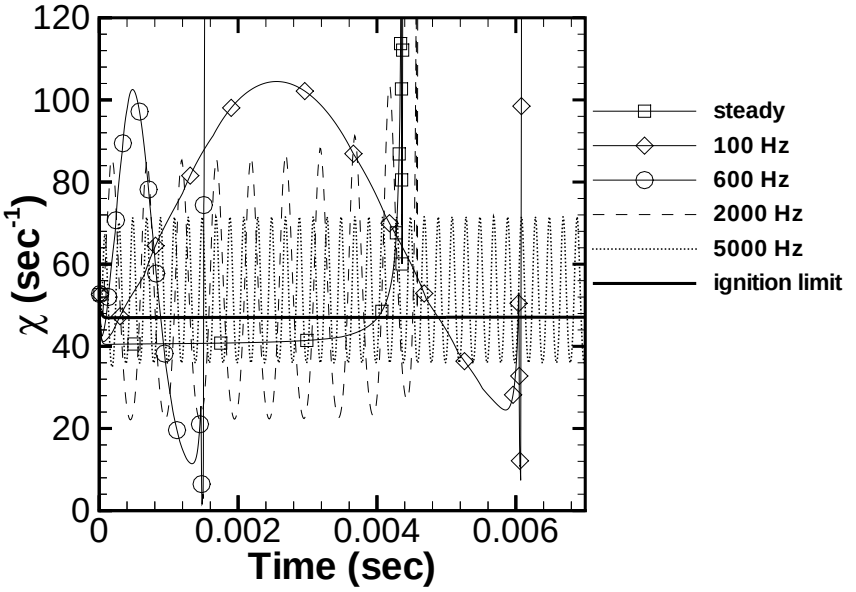

(b) Case B

Figure 4.2: Scalar dissipation rate at the ignition kernel as a function of time for different frequencies of velocity oscillation at the nozzle inlet, for (a) Case A and (b) Case B

4.2 Ignition Response to Unsteady Scalar Dissipation Rate

The response of ignition delay to unsteady scalar dissipation rate is now examined. The initial value (V_{init}) of velocity oscillation at the nozzle inlet is fixed at 1050 cm/s. Two different amplitudes of velocity oscillation are considered: $A = 0.4$ (Case A) and 0.8 (Case B). At both nozzle inlets velocity oscillates with the same magnitude and in phase. Since V_{init} is close to the steady ignition limit, for both cases the nozzle velocity becomes significantly greater than the steady ignition limit during the oscillatory cycle. The main consideration is the effect of frequency of oscillation on the overall ignition delay.

Figures 4.2(a) and 4.2(b) show the temporal variation in χ for Cases A and B, respectively, for various frequencies of oscillation. It is seen that χ responds sinusoidally, while its amplitude of oscillation becomes attenuated as the frequency increases. In both figures, the steady ignition limit (χ_s^*) is also plotted as a bold line. It appears that the ultimate fate of the mixture (whether it ignites or not) strongly depends on the overall mean scalar dissipation rate ($\overline{\chi}$) during the induction period. A rational definition of the mean scalar dissipation rate is given by:

$$\overline{\chi} = \frac{1}{t_{ign}} \int_0^{t_{ign}} \chi \, dt \tag{4.3}$$

where t_{ign} is the ignition delay for each frequency condition. For low frequencies, $\overline{\chi}$ depends on the initial phasing and frequency of the oscillation, while it converges to an asymptotic value at higher frequencies as a large number of oscillatory cycles occur during the induction period.

Comparing Figures 4.2(a) and 4.2(b), it is evident that the system in Case A ignites for all frequencies as $\overline{\chi}$ always falls below χ_s^*. For Case B, however, $\overline{\chi}$ exceeds χ_s^* at high frequencies and hence the system fails to ignite at high frequencies.

Figures 4.3(a) and (b) show the ignition delay and $\overline{\chi}$ as a function of frequency for Cases A and B, respectively. For Case A, the ignition characteristics are categorized into

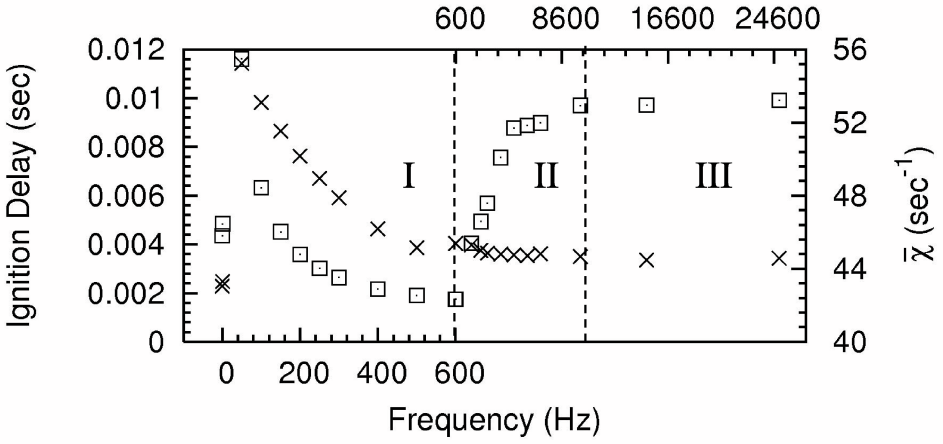

(a) Case A

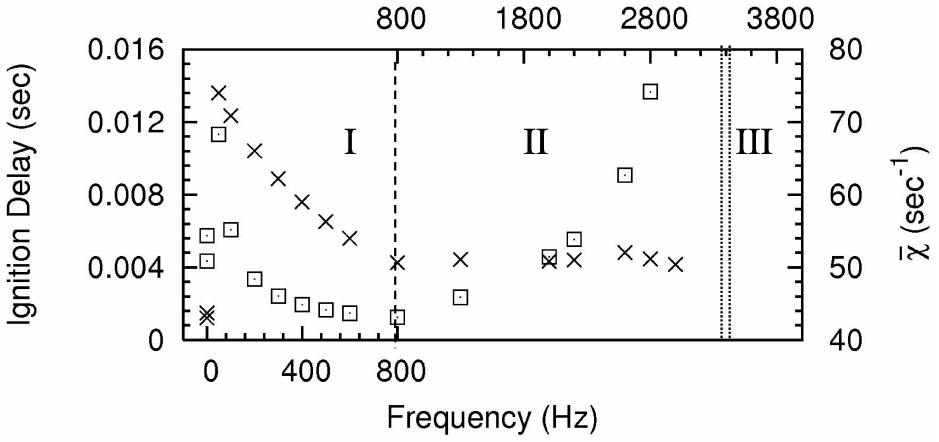

(b) Case B

Figure 4.3: Ignition delay (□) and $\overline{\chi}$ (×) as a function of frequency for (a) Case A and (b) Case B. Note that the frequency scale is split between bottom and top axes.

three regimes. At low frequencies (Regime I), ignition occurs before one complete cycle of oscillation. In this case, the ignition behavior is characterized as a quasi-steady response such that the ignition delay is dictated by the mean scalar dissipation rate during the induction time. This is clearly confirmed by the strong correlation between the ignition delay and $\overline{\chi}$. At intermediate frequencies (Regime II), the ignition delay increases with frequency while $\overline{\chi}$ remains almost constant. In this regime, ignition depends on the detailed unsteady response of the ignition kernel throughout the induction period. This issue will be further investigated in the next section. Finally, at higher frequencies (Regime III), the ignition kernel no longer responds to the rapid oscillation and the system recovers the quasi-steady characteristics. As in Regime I, whether the mixture ignites or not again depends entirely on the mean scalar dissipation rate relative to the steady limit. For Case A, ignition occurs because $\overline{\chi} < \chi_s^*$, and in this quasi-steady regime it is clearly seen that both ignition delay and $\overline{\chi}$ remains almost constant over a wide range of frequencies. Figure 4.3(b) shows the results for Case B, for which $\overline{\chi}$ exceeds χ_s^* in the high frequency limit. As a result, all the trends are similar to those shown in Figure 4.3(a) except that ignition does not occur in the high frequency limit. Therefore, it is difficult to identify the boundary between Regime II and Regime III in Case B.

Note that for the chosen amplitudes of oscillation (A = 0.4 and 0.8 for cases A and B, respectively) the ignition delay in Regime I first increases and then decreases for both the cases. However, if the phase of oscillation is shifted by 180 degrees, such that scalar dissipation rate first decreases and then increases, then the ignition delay would first decrease as frequency increases in Regime I. Nonetheless, the quasi-steady concept would still be valid in Regime I in that the ignition delay will correlate with the mean scalar dissipation rate in the induction period. This behavior is consistent with the results for the previous study presented in Chapter 3 on the autoignition of homogeneous mixture subjected to unsteady temperature fluctuations [69], in which a strong correlation between the ignition delay and the mean temperature was found at low frequencies.

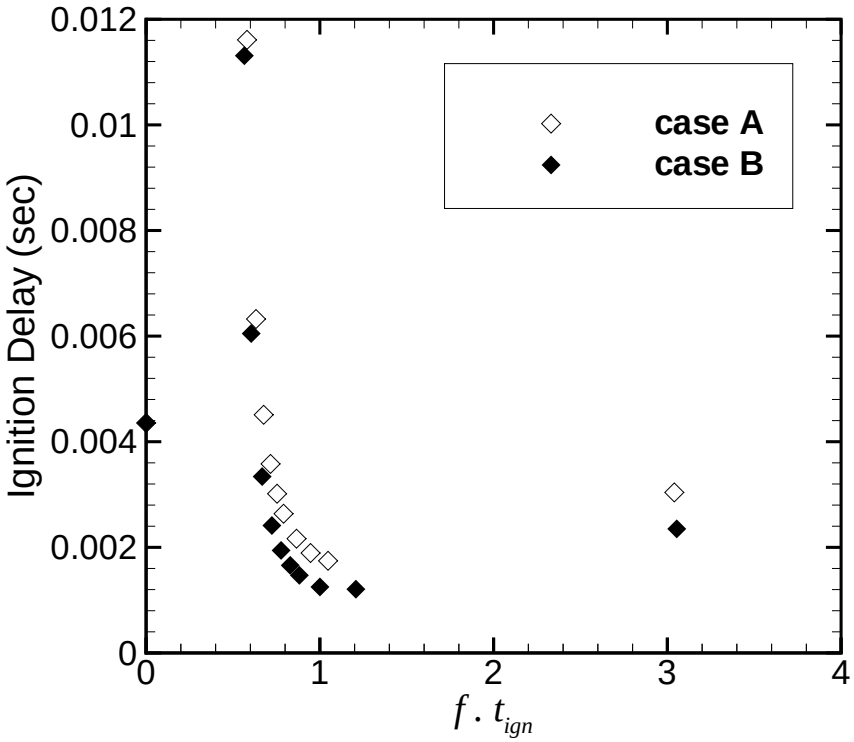

Figure 4.4: Ignition delay as a function of frequency*ignition delay for case A and case B

The transition from quasi-steady (Regime I) to unsteady (Regime II) ignition response depends on the ratio of characteristic time scale of unsteady fluctuation to the characteristic chemical time, which is the ignition delay. To confirm this point, ignition delay shown in Figures 4.3(a) and (b) is plotted against the normalized frequency, $f \cdot t_{ign}$. The normalized frequency represents the number of cycles in χ oscillation before ignition. Fig. 4.4 shows the results. The results for the two cases collapse very well, showing an initial abrupt rise and decay in the ignition delay. The minimum ignition delay is achieved at approximately $f \cdot t_{ign}$ = 1, which is considered the boundary between Regimes I and II. When the ignition kernel is exposed to more than one cycle of χ oscillation, the evolution of radical species in the ignition kernel undergoes excursions of loss and growth, and ignition event is a cumulative effect throughout the induction period. Thus the ignition response is no longer considered quasi-steady and the ignition delay does not correlate with $\overline{\chi}$. To describe the unsteady ignition behavior in the intermediate frequency range, the temporal history of the

Damköhler number at the ignition kernel needs to be considered.

4.2.1 Damköhler number response to oscillatory χ

Following a previous study [21], the kernel Damköhler number ($\mathrm{Da_H}$) is defined based on the hydrogen radical as:

$$\mathrm{Da_H} = \left| \frac{\dot{\omega}_\mathrm{H}}{\rho u(\partial Y_\mathrm{H}/\partial \mathrm{x}) + \partial(\rho Y_\mathrm{H} V_\mathrm{H}^D)/\partial \mathrm{x}} \right| \tag{4.4}$$

where V_H^D is the diffusion velocity of H radicals. As defined, $\mathrm{Da_H}$ at the ignition kernel represents the ratio of chemical production ($\dot{\omega}_\mathrm{H}$) to the transport loss in the H radical. Therefore, $\mathrm{Da_H} > 1$ indicate that the ignition kernel is at a favorable condition to ignite.

Figures 4.5(a) and (b) show the temporal history of $\mathrm{Da_H}$ for a few representative frequencies in the intermediate frequency range for Cases A and B, respectively. For Case B, a high frequency of 5000 Hz for which no ignition occurs is also shown. It is seen that $\mathrm{Da_H}$ responds to the sinusoidal fluctuations in χ. Note that ignition can occur after a number oscillations even if $\mathrm{Da_H} < 1$ for a significant fraction of the induction period.

An alternative view of Fig. 4.5(b) is shown in Figure 4.6 in which $\mathrm{Da_H}$ and Y_H are plotted in the phase space for three different frequencies. For f = 1600 Hz, as $\mathrm{Da_H}$ oscillates around unity, Y_H gradually increases in time and eventually takes off. On the other hand, at higher frequencies (f = 3000 and 5000 Hz), the evolution in Y_H reaches a limit cycle and no ignition occurs.

The above results suggest that the ignition kernel can survive some momentary unfavorable conditions and eventually ignite depending on the cumulative history of the kernel Damköhler number. It is conjectured that ignition can occur if the favorable condition ($\mathrm{Da_H} > 1$) is maintained for a duration longer than a critical value. To derive a rational criterion, we first determine the fraction of the time duration for which $\mathrm{Da_H} > 1$ during the

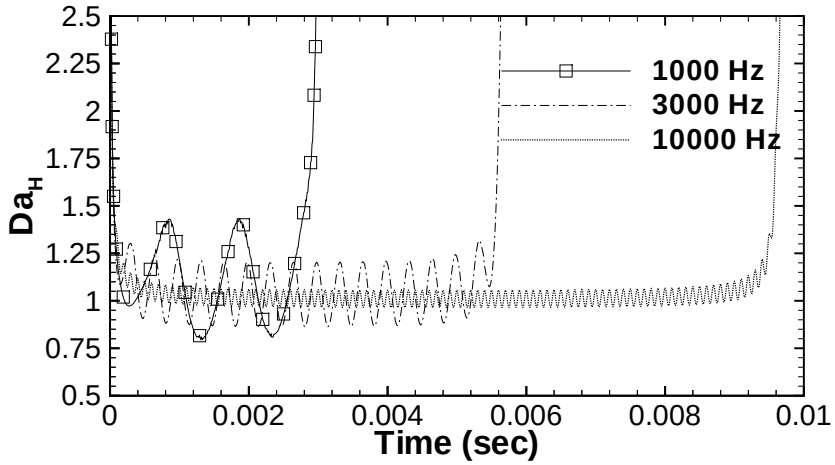

(a) Case A

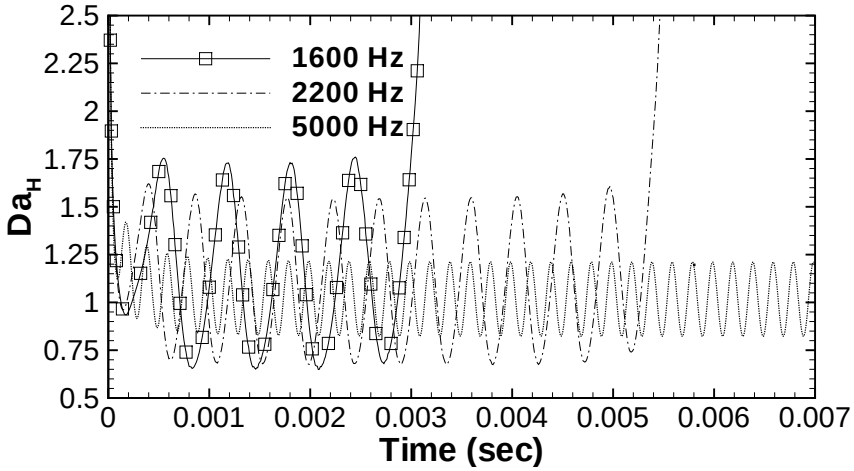

(b) Case B

Figure 4.5: Temporal history of Damköhler number for different frequencies in the intermediate frequency range for (a) case A, and (b) case B

ignition delay, given by:

$$\Delta_t = \frac{\text{time}(\text{Da}_\text{H} \geq 1)}{t_{ign}} \tag{4.5}$$

In other words, Δ_t represents the fractional duration of favorable condition for ignition. For the cases in which ignition does not occur, we replace the denominator in Eq. (4.5) by a sufficiently long time such that Δ_t converges. Subsequently, the mean kernel Damköhler

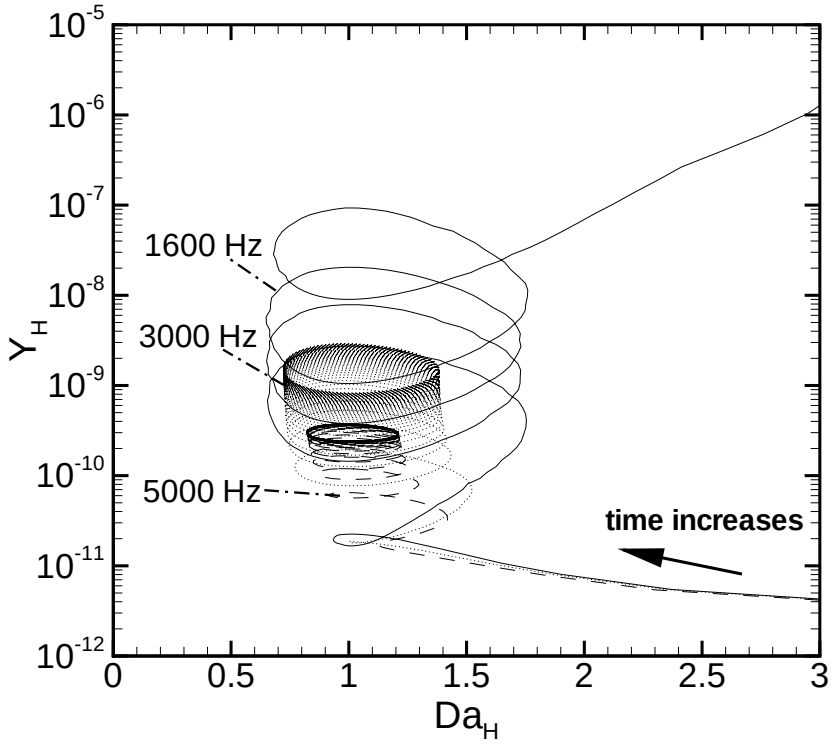

Figure 4.6: Transient evolution of $\mathrm{Da_H}$ and Y_H as the ignition event takes place, at various frequencies for case B

number is defined similar to Eq. (4.3) as:

$$\overline{\mathrm{Da}}_\mathrm{H} = \frac{1}{t_{ign}} \int_0^{t_{ign}} \mathrm{Da_H}\ \mathrm{dt} \tag{4.6}$$

Combining Eqs. (4.5) and (4.6), the ignitability (Γ) is defined as:

$$\Gamma\ = \overline{\mathrm{Da}}_\mathrm{H} \cdot \Delta_t \tag{4.7}$$

The ignitability parameter essentially accounts for the mean value of the kernel Damköhler number during the induction period as well as the fractional duration of the favorable condition for ignition. Figure 4.7 shows the plot of ignition delay as a function of Γ, for Cases A and B (lines + symbols) as well as for three additional cases (C to E) (lines) with different

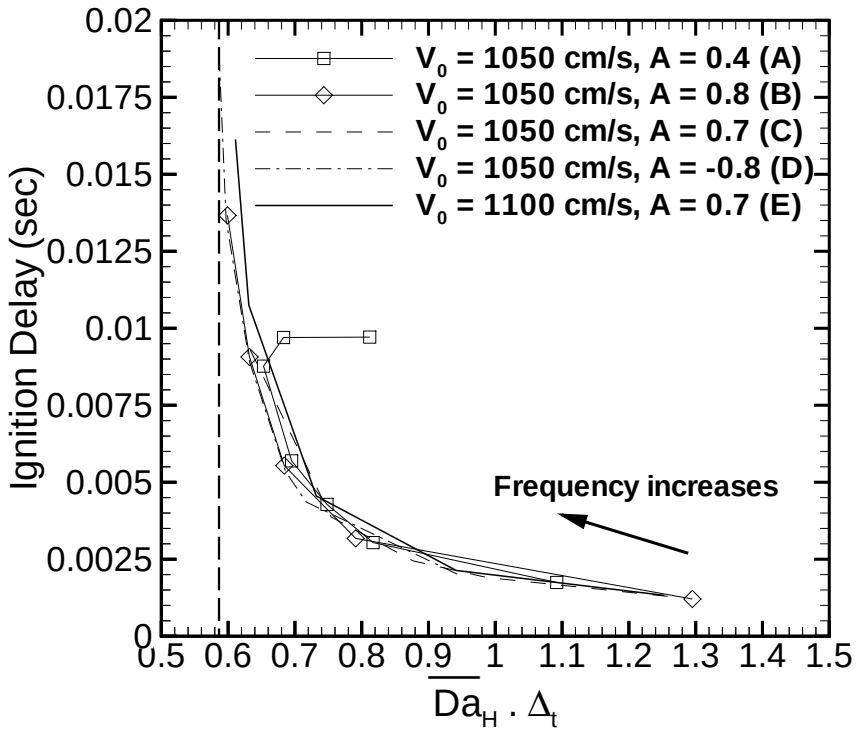

Figure 4.7: Ignition delay as a function of ignitability for cases A-E with different frequencies

values of initial velocity and amplitude. [V_{init}, A] = [1050, 0.7], [1050, -0.8] and [1100, 0.7], for Cases C, D, and E, respectively. The negative amplitude implies that the phase of velocity oscillation is shifted by 180 degrees. Cases C, D, and E all have converged $\overline{\chi} > \chi_s^*$ in the high frequency limit, similar to case B. Each data point in a given curve represents a result for a different frequency in Regime II. Since $\overline{\chi}$ differs for different cases, the range of frequency that corresponds to Regime II also differs. For example, the frequency range shown in the figure ranges from 1000 Hz and to 2800 Hz for Case B, while the range changes to 1300-2900 Hz for Case D. Nevertheless, the ignition delay versus Γ curves for all five cases collapse surprisingly well. The only exception is for Case A, which has a different high frequency limit ($\overline{\chi} < \chi_s^*$). In this case, the ignition delay levels off to a constant value in the high frequency limit (the data shown are for frequencies up to 10,000 Hz). As discussed before, at such high frequencies the ignition response becomes quasi-steady

again, and thus depends solely on either $\overline{\mathrm{Da}_{\mathrm{H}}}$ or $\overline{\chi}$. Note that, for all of the cases considered, no ignition was observed for Γ less than 0.59, which is denoted by a vertical dashed line in Fig. 4.7. Therefore, this ignitability parameter serves as a generalized ignitability criterion for a wide range of parametric conditions, and provides a unified description of the unsteady ignition phenomena.

Having obtained a unified description of autoignition response of nonpremixed hydrogen-air mixture to scalar dissipation rate fluctuations, in the next Chapter we study autoignition of more complex nonpremixed n-heptane-air mixture using a similar configuration. The ignitability parameter developed in this Chapter will be applied to n-heptane autoignition in the next Chapter.

Chapter 5

Effects of Unsteady Scalar Dissipation Rate on Nonpremixed *n*-Heptane/Air Autoignition

After obtaining significant insights and a unified description of nonpremixed hydrogen/air autoignition in unsteady scalar dissipation rate conditions in last Chapter, in this Chapter we study a more complex *n*-heptane/air system. As mentioned in the Introduction Chapter, one of the key distinctive features of *n*-heptane, which is most pronounced in diesel engine applications, is that they often exhibit two-stage ignition under the typical operating conditions. This behavior has been explained by the negative temperature coefficient (NTC) regime, due to a competition between recombination of isomerization products and the activation of radical branching through H_2O_2 at intermediate temperatures near 900K [24]. The computational methodology used in this study is similar to that employed for hydrogen autoignition study in Chapter 4 and the details are given in Chapter 2.

For the detailed reaction kinetics model, we adopt the *n*-heptane mechanism with 185 reactions and 43 species [22], which has been extensively validated to reproduce the two-stage ignition behavior over a wide range of conditions. For all cases considered, pre-vaporized *n*-Heptane (15 %) diluted with N_2 (85 %) is supplied from the nozzle at x = 0 cm and is impinged against air (N_2 - 79 % and O_2 - 21 %) injected from the other nozzle at x = 0.5 cm. The pressure is fixed to 40 atm. Unless otherwise stated, the fuel and oxidizer stream temperatures are set at 572 K and 827 K, respectively, following the previous study [22]; 572 K corresponds to the boiling temperature of *n*-heptane at 40 atm, and 827

K is obtained by the adiabatic compression of air at 300 K from 1 atm to 40 atm.

As in Chapter 4, unsteady scalar dissipation rate is imposed by specifying a time-varying velocity at both the nozzle inlets. The functional form of the velocity oscillation is given in Eq. 2.13 of Chapter 2. The initial condition for the unsteady calculations is generated by computing a steady solution with all the reaction terms suppressed. Then the unsteady computation is performed with reactions turned on at t = 0.

The ignition kernel is defined as the location of maximum OH mass fraction, which indicates region of intense chemical reaction. We will verify in subsequent discussion that an alternative definition of the ignition kernel (such as based on the maximum heat release) does not affect the results and conclusion of this study. The ignition delay is defined as the time at which the growth rate of peak temperature in the domain becomes maximum. In the presence of two-stage ignition, this always corresponds to the time of the second stage ignition.

Scalar dissipation rate χ, is defined in Eq. 4.2 in Chapter 4. Mixture fraction variable is again defined following Bilger's definition [68]. The values of χ at the stoichiometric mixture fraction, χ_{st}, as well as that at the ignition kernel, χ_k, are reported in the subsequent results and discussion.

5.1 Steady Ignition Behavior

As a baseline case, we first examine the temporal evolution of ignition for various steady scalar dissipation rates. Figure 5.1 shows the time evolution of the maximum temperature for various scalar dissipation rates at the stoichiometric mixture fraction, χ_{st}, in the frozen flow. At the chosen parametric conditions, distinct two-stage ignition behavior is clearly seen: at the first stage, low temperature chemistry associated with keto-heptyl peroxide (henceforth referred to as KET) brings the temperature up by approximately 100K, and the second stage ignition occurs after an additional delay.

As reported by Liu *et al.* [22], Fig. 5.1 confirms that the first stage ignition is rather in-

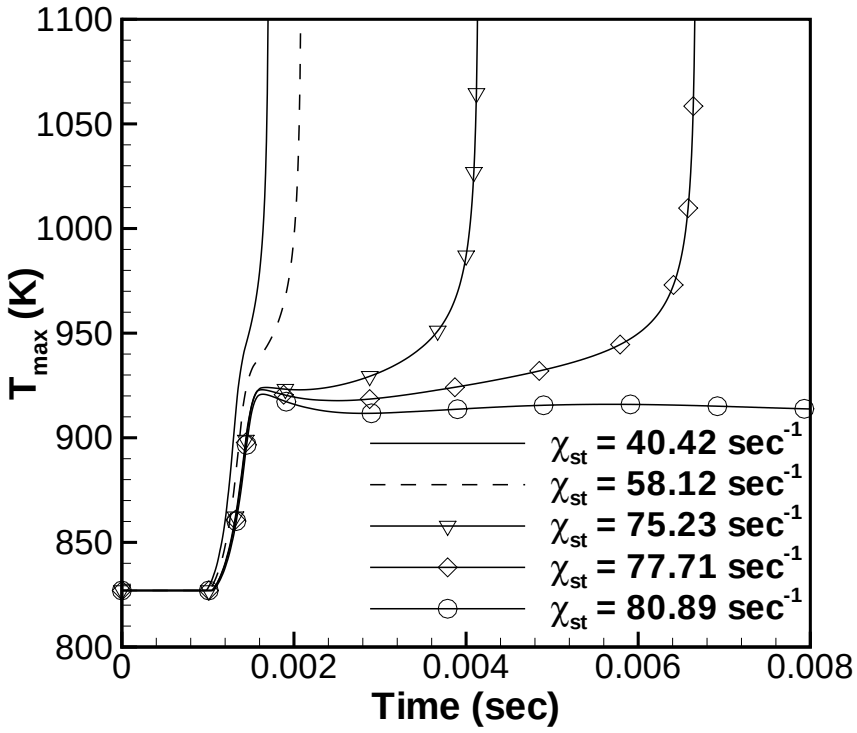

Figure 5.1: Time evolution of the maximum temperature for various steady values of χ_{st}

sensitive to the variations in χ_{st}, while the second stage ignition shows a strong sensitivity. For χ_{st} exceeding the steady ignition limit of 79 sec^{-1}, no second stage ignition is observed. While Liu *et al.*discussed in detail as to why this is so, here we offer an alternative, and perhaps simpler, explanation for this observed behavior. Figures 5.2 and 5.3 show the profiles of the OH mass fraction, which is the key radical species demarcating the ignition kernel location, and the corresponding scalar dissipation rate in the physical and mixture fraction coordinates, respectively, for χ_{st} = 75.23 s^{-1}. At t = 0.5 msec, it is clearly seen that the initial ignition kernel development due to the low-temperature chemistry occurs near the oxidizer side, at which the magnitude of the scalar dissipation rate is practically negligible. As the ignition progress further (t = 1.4 msec and later), only after the first-stage temperature rise has occurred, the ignition kernel moves into the mixing layer at which a significant level of the χ exists, hence becomes sensitive to the imposed scalar dissipation rate.

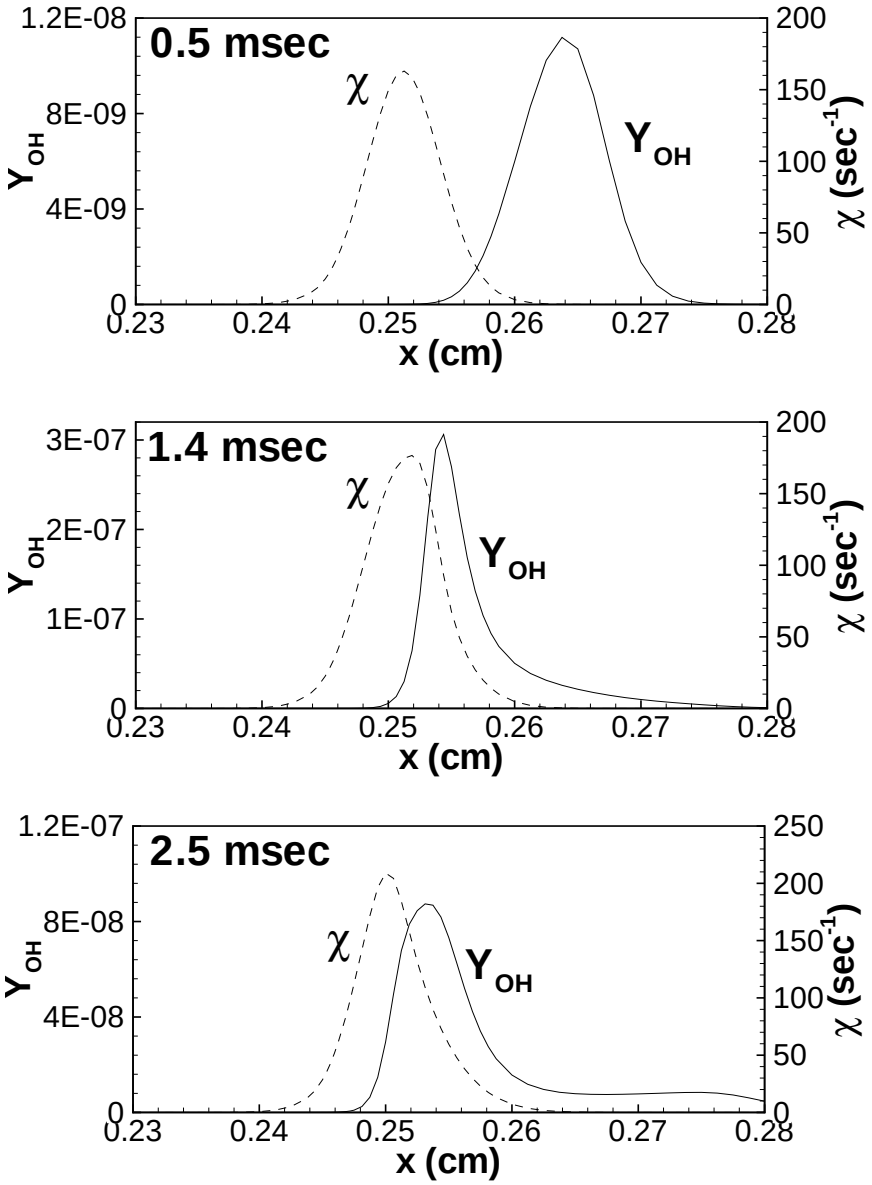

Figure 5.2: OH mass fraction and scalar dissipation rate versus axial location for $\chi_{st} = 75.23\ \mathrm{s}^{-1}$ at three different times during ignition: t = 0.5, 1.4, 2.5 msec.

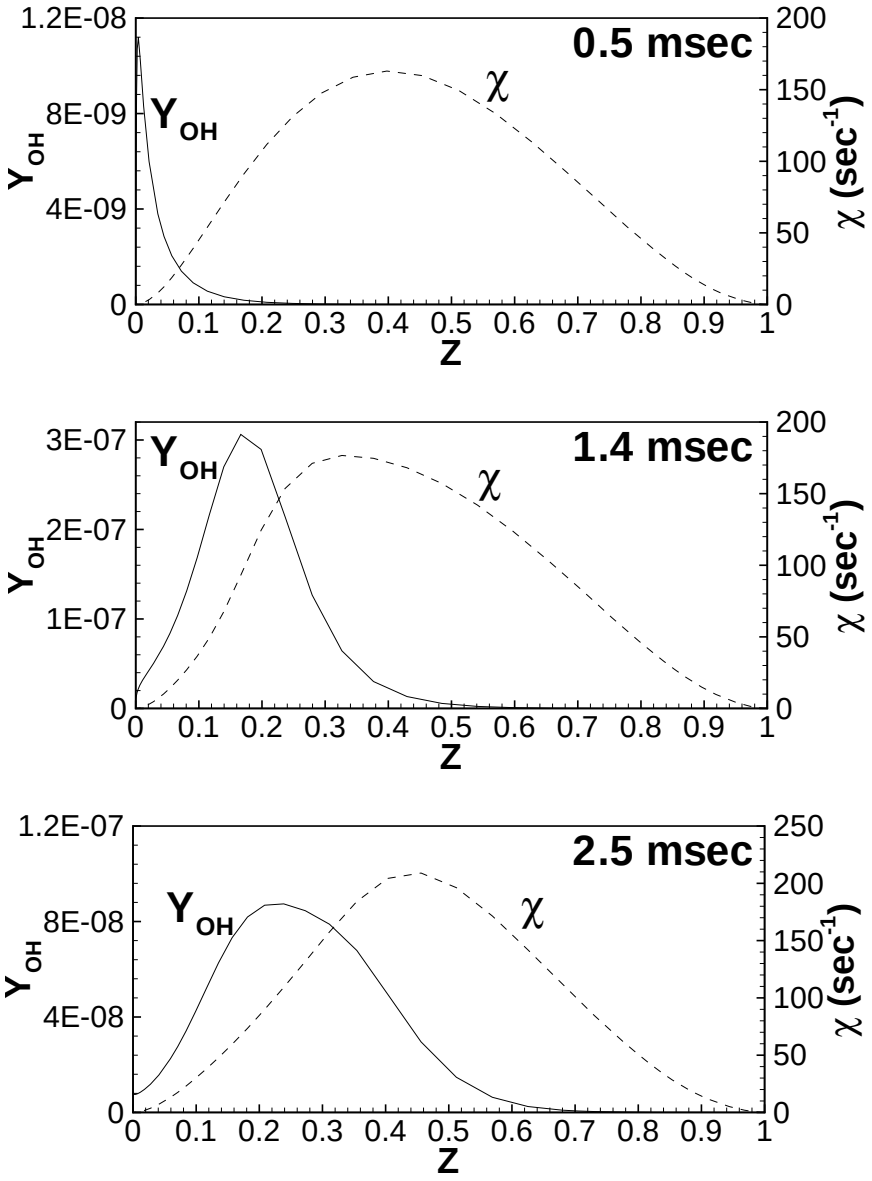

Figure 5.3: OH mass fraction and scalar dissipation rate versus mixture fraction for $\chi_{st} = 75.23\ \mathrm{s}^{-1}$ at three different times during ignition: t = 0.5, 1.4, 2.5 msec.

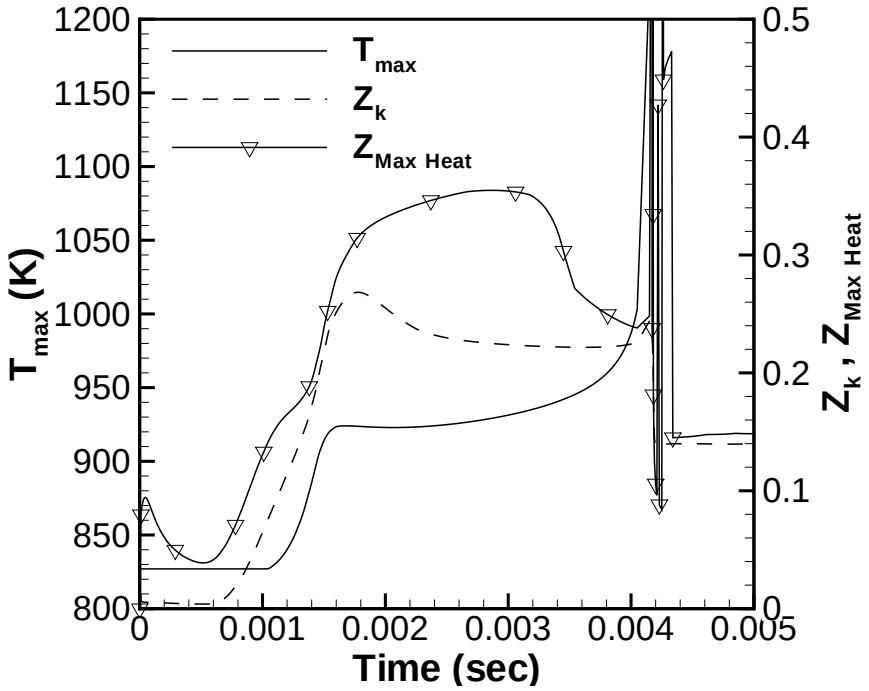

Figure 5.4: Temporal history of the maximum temperature, ignition kernel location and maximum heat release rate location in the mixture fraction space for χ_{st} = 75.23 s^{-1}.

Figure 5.4 shows the temporal evolution of the maximum temperature for χ_{st} = 75.23 s^{-1} along with the location of the ignition kernel in the mixture fraction space. Z_k is the ignition kernel location based on the peak OH mass fraction. Alternatively, the ignition kernel defined as the maximum heat release location, Z_{MaxHeat} is also plotted. For either definition, it is confirmed that the ignition kernel resides in the region of low χ throughout the first stage, and then migrates into a higher χ region only after a significant development into the second stage induction. Although not shown here, consistent behavior was observed even when the initial temperature field is completely uniform, indicating that the initial nonuniform temperature profile is not solely responsible this behavior. In summary, during the autoignition event in a mixing layer of higher hydrocarbon fuels and air, the first stage ignition in general occurs in the region of low scalar dissipation rate, thereby avoiding the sensitivity to the diffusive loss of radicals from the ignition kernel.

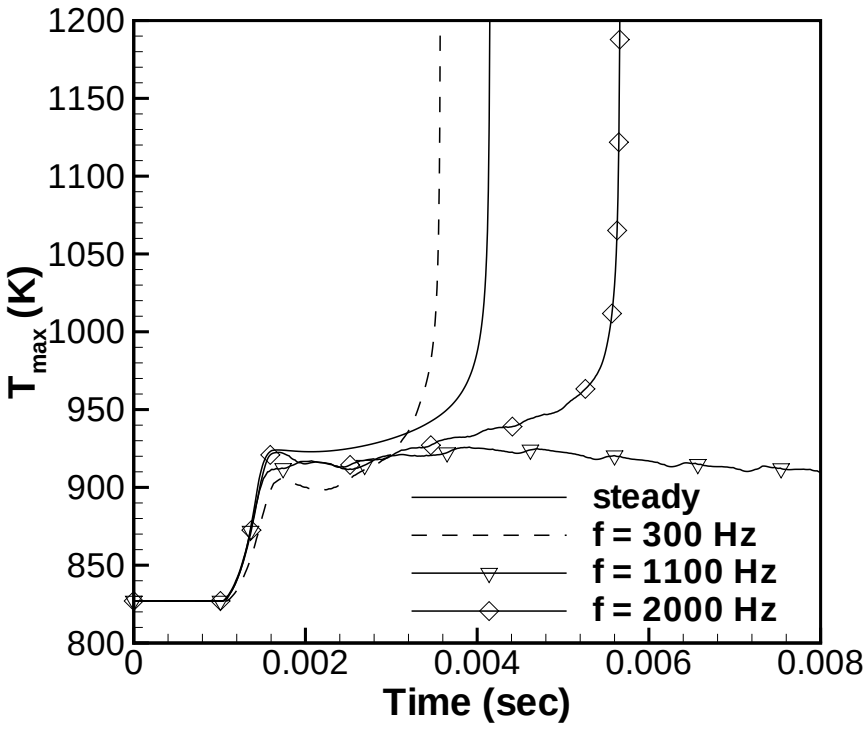

Figure 5.5: Time evolution of the maximum temperature for an oscillatory scalar dissipation rate at various frequencies. The steady case corresponds to χ_{st} = 75.23 s^{-1}.

5.2 Ignition Response to Oscillatory Scalar Dissipation Rate

Next, we study the effects of sinusoidal fluctuations of scalar dissipation rate, as prescribed by Eq. (2.13). The baseline steady case for χ_{st} = 75.23 s^{-1} in the previous section is chosen, which corresponds to the initial nozzle velocities of the fuel and oxidizer streams to be 65 cm/s and 90.7 cm/s, respectively. The amplitude of velocity oscillation at the boundary is fixed at A = 0.7, which is chosen such that the instantaneous χ exceeds the steady ignition limit for some duration during the induction period.

Figure 5.5 shows the maximum temperature versus time for the oscillatory scalar dissipation rate at various frequencies. Note that the effect of the unsteady χ fluctuation is not monotonic in frequency. At 300 Hz, the ignition delay is actually advanced in comparison to the steady reference condition. As frequency increases further, the mixture becomes completely non-ignitable (e.g. at 1100 Hz). At even higher frequency (2000 Hz), however,

the mixture becomes ignitable again with the ignition time delayed comparable to the reference steady condition. These results are summarized in Fig. 5.6(a), in which the ignition delay (t_{ign}) is plotted as a function of the frequency. It appears that, similar to the hydrogen study presented in the last Chapter, distinct ignition behavior is observed in three different frequency regimes: low frequency (0-625 Hz), intermediate frequency (650-1700 Hz), and high frequency ($>$ 1700 Hz). The characteristics of each regime will be described in the following.

In the low frequency regime up to 625 Hz, it was found that the χ oscillation barely completes one cycle during the second-stage ignition delay. In this quasi-steady regime, we found that the ignition delay correlates well with the mean scalar dissipation rate at the ignition kernel, $\overline{\chi_k}$, defined similar to the hydrogen study as:

$$\overline{\chi_k} = \frac{1}{t_{ign}} \int_0^{t_{ign}} \chi_k \, dt \tag{5.1}$$

Figure 5.6(b) shows the plot of $\overline{\chi_k}$ as a function of frequency. $\overline{\chi_k}$ appears to correlate very well with the ignition delay behavior shown in Fig. 5.6(a) for the low frequency regime. This result is consistent with that presented for the hydrogen/air autoignition [70] in Chapter 4, in which also $\overline{\chi_k}$ was found to correlate well with the ignition delay at low frequencies. Figure 5.6(b) also shows the mean scalar dissipation rate measured at the stoichiometric mixture fraction, $\overline{\chi_{st}}$ (defined similar to Eq. 5.1), which does not correlate as well as $\overline{\chi_k}$ does. Due to the complex chemistry of *n*-heptane oxidation, the ignition kernel location varies significantly during the two-stage ignition process, hence χ_{st} does not properly represent the effective dissipation rate that the ignition kernel experiences.

For intermediate frequencies (650-1700 Hz), ignition does not occur at all. As the imposed unsteady time scale becomes small, the duration for which the scalar dissipation rate is favorable for ignition is not long enough for the kernel to ignite in a quasi-steady manner. In this case, the $\overline{\chi_k}$ and $\overline{\chi_{st}}$ values are determined by extending the integral in

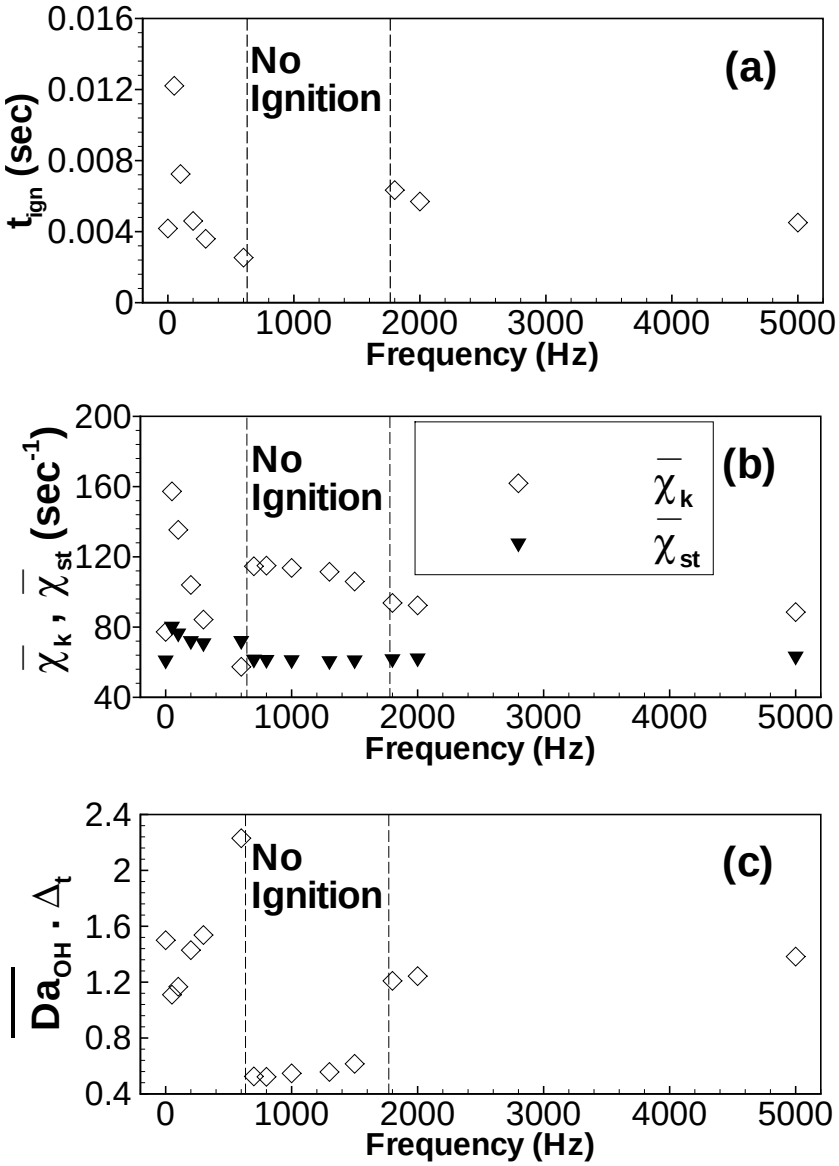

Figure 5.6: (a) Ignition delay, (b) $\overline{\chi_k}$ and $\overline{\chi_{st}}$, and (c) Γ as a function of frequency for the case shown in Fig. 4.

Eq. (5.1) to $t \rightarrow \infty$. The ignition behavior becomes fully unsteady and neither of these mean scalar dissipation rates adequately serve as a measure to determine ignitability of the mixture. To obtain a rational ignitability criterion, we follow the hydrogen autoignition study [70] presented in Chapter 4, and first define the kernel Damköhler number based on the OH radical as:

$$\mathrm{Da_{OH}} = \left| \frac{\dot{\omega}_{\mathrm{OH}}}{\rho u(\partial Y_{\mathrm{OH}}/\partial x) + \partial(\rho Y_{\mathrm{OH}} V^D_{\mathrm{OH}})/\partial x} \right|_k \tag{5.2}$$

where V^D_{OH} is the diffusion velocity of OH radicals. As defined, $\mathrm{Da_{OH}}$ at the ignition kernel represents the ratio of chemical production ($\dot{\omega}_{\mathrm{OH}}$) to the transport loss in the OH radical. Therefore, $\mathrm{Da_{OH}} > 1$ indicate that the ignition kernel is at a favorable condition to ignite.

Subsequently, the ignitability (Γ) is defined similar to Chapter 4 as:

$$\Gamma = \overline{\mathrm{Da}}_{\mathrm{OH}} \cdot \Delta_t \tag{5.3}$$

where

$$\overline{\mathrm{Da}}_{\mathrm{OH}} = \frac{1}{t_{ign}} \int_0^{t_{ign}} \mathrm{Da_{OH}}\, \mathrm{dt} \tag{5.4}$$

is the mean kernel Damköhler number defined similar to Eq. (5.1) and

$$\Delta_t = \frac{\mathrm{time}(\mathrm{Da_{OH}} \geq 1)}{t_{ign}} \tag{5.5}$$

represents the fractional duration of favorable condition for ignition. In case ignition does not occur, t_{ign} in Eq. (5.5) is replaced by a sufficiently long time for Δ_t to converge. The ignitability (Γ) thus accounts for both the mean value of the kernel Damköhler number during the induction period as well as the fractional duration of the favorable condition for ignition. Both of these parameters are independent and are important for correct prediction of ignition behavior as was demonstrated in the last Chapter. Fig. 5.6(c) shows Γ as a function of frequency. For intermediate frequencies for which ignition does not occur, Γ

value drops below 0.62. This is consistent with results presented in Chapter 4, in which the critical Γ value was found to be 0.59. Therefore, Γ is found to be an appropriate ignitability criterion for unsteady ignition even for *n*-heptane fuel.

At higher frequencies beyond 1700 Hz, the ignition kernel no longer responds to the rapid unsteady fluctuations in scalar dissipation rate, and the system recovers the quasi-steady characteristics. Therefore, as can be seen from Figs. 5.6(a) and (b), ignition delay again starts to correlate well with the mean scalar dissipation rate at the ignition kernel.

5.3 Unsteady Ignition at a Higher Temperature

Through the extensive parametric studies, we have also made an interesting observation at higher temperature conditions. In this case, for the same pressure at 40 atm, the initial frozen temperature field is fixed uniformly at 920 K which falls into the intermediate temperature regime where NTC chemistry becomes negligible. The initial χ_{st} is set at 277 s^{-1}, which corresponds to the initial nozzle velocities of the fuel and oxidizer streams to be 290 cm/s and 336.4 cm/s, respectively in the frozen flow, and an oscillatory velocity with A = 0.7 is imposed at various frequencies.

Figure 5.7 shows the maximum temperature evolution for various frequencies. At this high temperature condition, the reference steady ignition event (thin solid line) does not reveal noticeable two-stage ignition behavior. As the unsteady oscillation is imposed, however, the second stage ignition behavior reappears. This tendency is more pronounced at lower frequencies and the behavior gradually attenuates as the frequency increases (from 50 to 500 Hz). At frequencies beyond 500 Hz, the system becomes completely non-ignitable. Unlike the results in the previous section, the mixture does not return to ignitable state even at higher frequencies. The behavior in the high frequency limit can be simply explained based on the Γ parameter as discussed before, and is not repeated here. On the other hand, the re-emergence of the two-stage ignition at low frequencies needs further investigation and is discussed as follows.

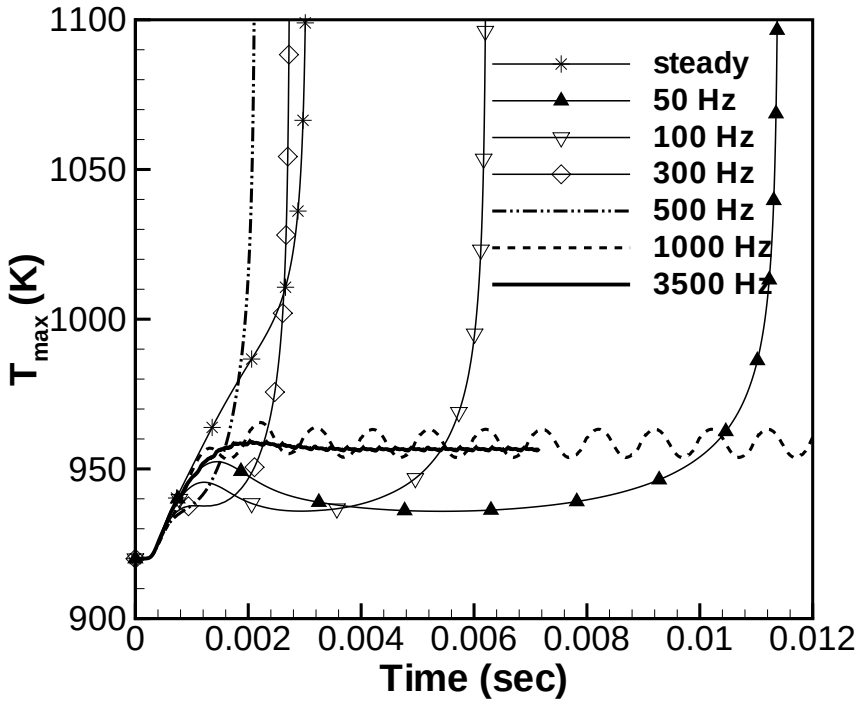

Figure 5.7: Time evolution of the maximum temperature for an oscillatory scalar dissipation rate at various frequencies: uniform initial temperature at 920K and χ_{st} = 277 s^{-1}.

For the large amplitude of oscillation as chosen in this case, the large instantaneous value of χ enhances the dissipation of radicals during the induction period, resulting in a widespread ignition kernel. Figure 5.8 shows the profiles of several intermediate species (KET and H_2O_2 respectively representing the key intermediates for the first and second stage ignition) at the time when the system is in the middle of the long second-stage delay (t = 0.002 s). It is seen that the OH peak is significantly separated from from the maximum KET or H_2O_2 regions, resulting in attenuation of the chemical reactivity at the ignition kernel. In summary, the mechanism for the two-stage ignition observed in Fig. 5.7 is attributed to enhanced transport losses, in contrast to the commonly observed two-stage ignition behavior which is due to the chemical competition (NTC regime). The latter is observed in both homogeneous and inhomogeneous systems, while the former is unique to the nonpremixed mixing layer where strong transport effects are present. This result pro-

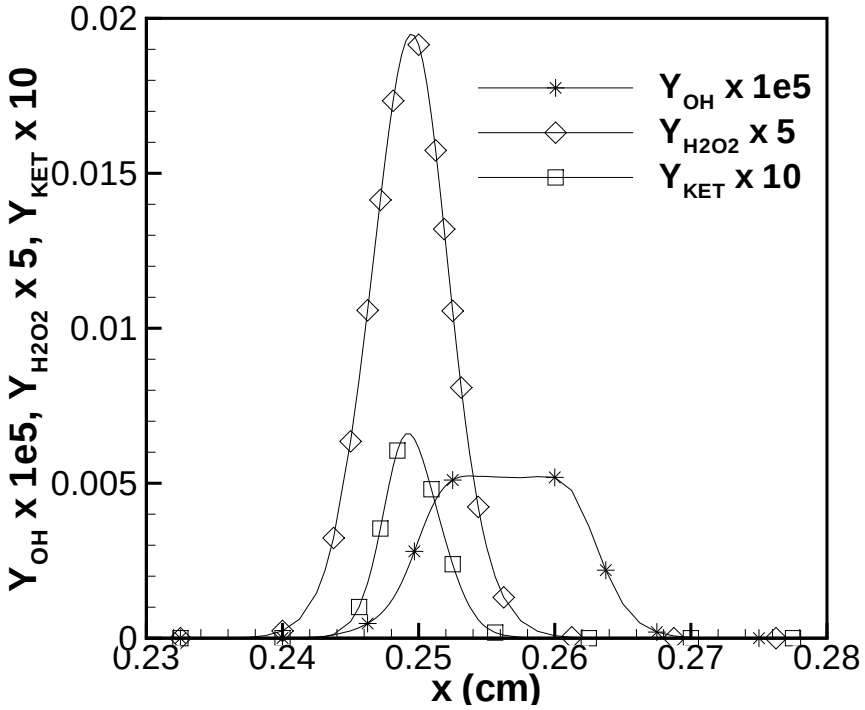

Figure 5.8: OH, H_2O_2 and KET mass fraction profiles at t = 0.002 s for f = 100 Hz, χ_{st} = 277 s^{-1}.

vides a practical implication that the occurrence of two-stage ignition in an IC engine may be promoted when there exist high levels of turbulence and mixture stratification.

5.4 Implications for Turbulent Combustion Modeling

The unsteady ignition behavior observed in this study provides insights into modeling of autoignition in turbulent reacting flows, especially in the context of the flamelet [29] or conditional moment closure [30] approaches. Using the space-time equivalence through the Taylor's hypothesis, the unsteady mixing layer under study may represent an igniting unsteady flamelet subjected to turbulent fluctuations. A cumulative plot of the scalar dissipation rate versus the mixture fraction variable through a number of oscillatory cycles is shown in Fig. 5.9, which resembles a typical scatter plot of turbulent reacting flow data. In the flamelet approach, the evolution of reactive scalars (ψ_i) is described by the *representa-*

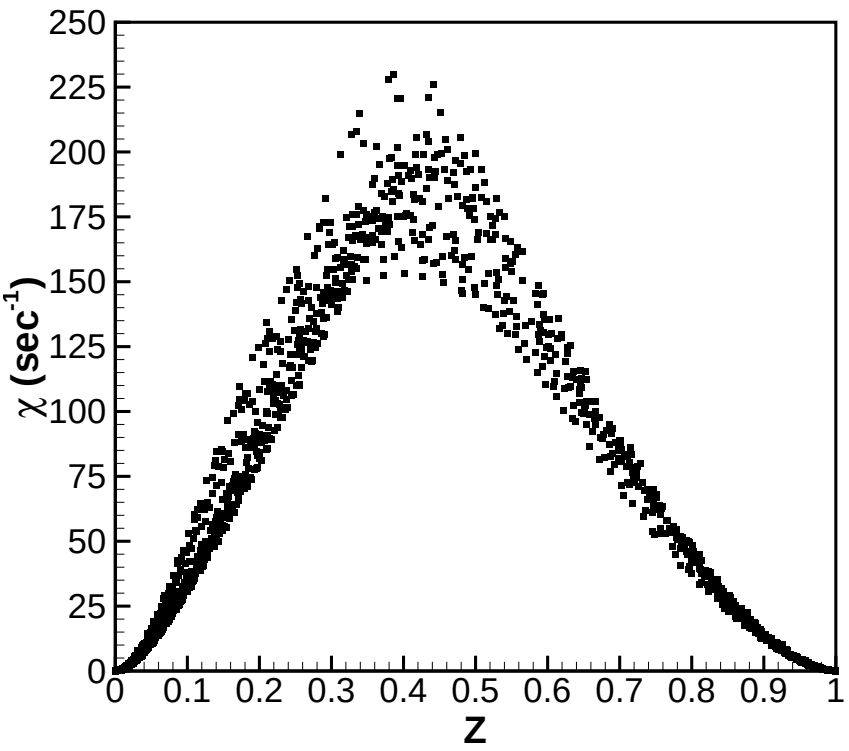

Figure 5.9: Scalar dissipation rate as a function of mixture fraction at various time instants for frequency = 1300 Hz and χ_{st} = 75.23 s^{-1} in frozen flow.

tive flamelet equation [29]:

$$\frac{\partial \psi_i}{\partial t} = \frac{\widetilde{\chi_Z}}{2}\frac{\partial^2 \psi_i}{\partial Z^2} + \frac{\omega_i}{\rho} \tag{5.6}$$

in which the conditional Favre mean value $\widetilde{\chi_Z}$ replaces the scalar dissipation rate as the key parameter of the equation. A similar equation is obtained for the first-order conditional moment closure model. This approach inherently assumes that reaction behavior is dictated only by the conditional mean scalar dissipation rate, while its fluctuations are neglected. The results shown in Fig. 5.6 suggest that this approximation is valid only if the fluctuation time scale is sufficiently longer or shorter than the ignition delay such that the ignition response can be considered quasi-steady. If it falls into the intermediate frequency regime, then an additional parameter (such as Δ_t defined in this study) accounting for the magnitude of fluctuation about the mean value must be considered, thereby further complicating the combustion submodels.

The results presented in Chapters 3 and 4 and the present Chapter on the effects of unsteady fluctuations in flow velocity/scalars on the autoignition behavior can be summarized as follows. Firstly, it should be noted that the results on the effects of temporal fluctuations in flow velocity/scalars presented in these chapters can be related to the effects of spatial inhomogeneities through a Lagrangian-Eulerian conversion. The following are the major conclusions of these chapters. At low frequencies of fluctuation, which correspond to large eddy turnover times, the response of ignition delay is always quasi-steady. In this regime, ignition delay is well correlated with the time-averaged value of the imposed oscillating variable. At very high frequencies of fluctuation, which correspond to small eddy turnover times, the system again recovers quasi-steady characteristics. In this high frequency regime, the ignition delay response to frequency levels off. However, it should be emphasized that the asymptotic value of ignition delay at high frequency limit might be different from the reference ignition delay (at zero frequency). The reason for this may be attributed to the inherent non-linearity of the phenomena. At intermediate frequencies, i.e. when the eddy turnover time is comparable to ignition delay, the ignition delay response is completely unsteady. In this regime, time averaged value of imposed oscillating variable is not sufficient to characterize the ignition delay response, and additional variables are required to describe the phenomena. In the homogeneous ignition study presented in Chapter 3, this variable was identified as the instantaneous gradient of temperature oscillation at the onset of ignition, whereas for the nonpremixed fuel-air ignition studies presented in Chapter 4 and the present Chapter an ignitability parameter was proposed for this purpose. In real turbulent flows, a range of eddies with a range of turnover times will be present and then the ignition delay response may be a represented by a combination of responses at different monochromatic frequencies.

Chapter 6

Turbulent Mixing in LTC Engine Environments

So far, we have investigated the effects of unsteadiness associated with some key scalar or flow velocity on autoignition behavior and ignition delay. The primary objectives for this and the next Chapter are to investigate the effects of spatial inhomogeneities in scalars such as temperature and equivalence ratio on the modes of combustion in realistic LTC engine environments. As mentioned in the Introduction Chapter, due to the presence of thermal and compositional inhomogeneities both volumetric and front-like combustion modes have been observed in experiments [13, 15, 16]. It is anticipated that depending on fuel-injection timing, wall heat loss, and exhaust gas recirculation (EGR), scalar fields with different levels on inhomgeneities and different patterns may exist prior to autoignition. Therefore, in this Chapter we investigate the different mixture formation patterns close to top-dead-center (TDC), prior to autoignition. Of particular interest is to identify the possible correlations between temperature and equivalence ratio fields prior to autoignition.

For this purpose, non-reacting simulations are conducted for a 3D 4-valve pentroof engine using KIVA-3V. The turbulence model is based on the Reynolds-Averaged-Navier-Stokes (RANS) approach, and the conventional $k - \epsilon$ model is adopted in this study. Table 6.1 lists the specifications and the operating conditions of the engine simulated. The mesh consists of about 50000 grid cells and is shown in Fig 6.1. Gasoline fuel is used to represent realistic spray evaporation behavior. Fuel is injected from the top of the cylinder head vertically downwards. The results obtained in this study will provide the representative scalar fields to be studied for autoignition and combustion behavior using direct

Bore	9.2 cm
Stroke	8.5 cm
Compression ratio	9.64
IVO	28 BTDC
IVC	66 ABDC
EVO	112 ATDC
EVC	28 ATDC
T_{head}	400 K
T_{piston}	400 K
$T_{cylinderwall}$	400 K
RPM	1500
Intake temperature	400 K

Table 6.1: Engine specifications and operating conditions.

numerical simulations in next Chapter.

Using the non-reacting simulations, the effects of fuel injection timing on mixture formation are studied. Towards this goal, two cases are studied with different fuel-injection timing. Case (kA) has a start of injection (SOI) timing of 270 degrees before TDC, and Case (kB) has SOI of 90 before TDC. Thus, Case (kA) represents an early-injection scenario and Case (kB) represents a late-injection scenario. In both cases, duration of injection was 48 crank angle degrees and the global equivalence ratio was fixed to 0.19. Both simulations were initiated at 375 degrees before TDC (BTDC) and the initial turbulence kinetic energy was 10% of kinetic energy based on mean piston speed.

The results for Case (kA), the early injection case, are first examined. Figure 6.2 shows the fuel mass fraction and temperature fields at 15 degrees BTDC, in a plane normal to the cylinder axis close to the top wall of the cylinder. It is observed that temperature is high in the middle and low close to the walls due to wall heat loss. It can be seen that apart from the slight negative correlation on the right boundary due to the evaporation cooling effect, the two fields are largely uncorrelated with each other. This is owing to the turbulence mixing and wall heat loss effects. This is further demonstrated in Fig. 6.3 which shows the scatter plot of fuel mass fraction and temperature also at 15 degrees BTDC. The scatter plot

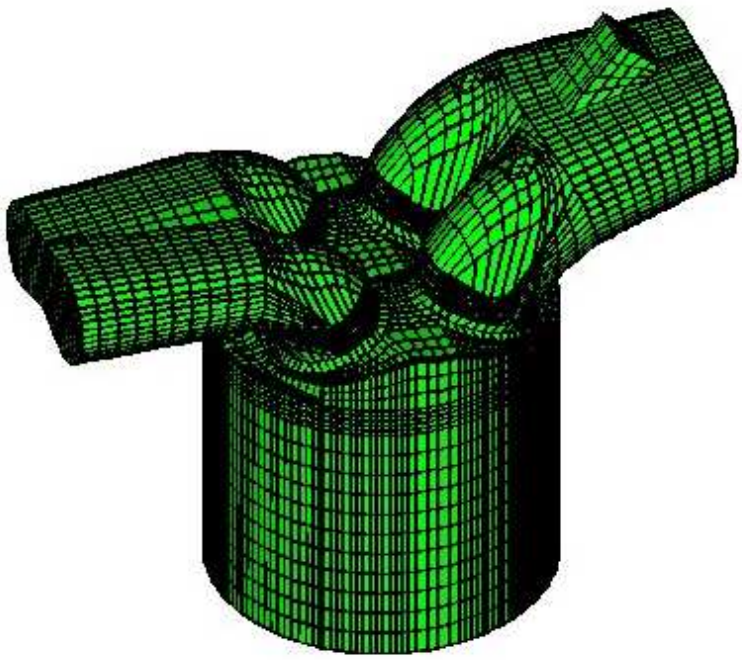

Figure 6.1: Pentroof engine mesh with about 50000 cells used for KIVA-3V simulations.

includes all the data points inside the engine cylinder and shows that the fields are mostly uncorrelated. For most of the cells in the cylinder, the temperature varies between about 700 K and 800 K, and the fuel mass fraction varies between 0 to about 0.03. The mass-based stoichiometric fuel to air ratio for gasoline is 0.0672, implying that the equivalence ratio in the cylinder varies between 0 to 0.46.

Next, the results for Case (kB), the late-injection case, are examined. Figure 6.4 shows the fuel mass fraction and temperature fields at 15 degrees BTDC, in the same cross-sectional plane of the cylinder as the previous case. Unlike Case (kA), the temperature and fuel mass fraction fields are negatively-correlated to a large extent. At a location slightly to the right of center, the fuel has evaporated and the temperature has reduced due to evaporative cooling effect. In the periphery of evaporated fuel region, temperature is high and fuel mass fraction is almost zero. Wall heat loss effects are again seen in the thin region near the wall where temperature is lower. Figure 6.5 shows the scatter plot of fuel mass fraction and temperature fields at 15 BTDC for Case (kB). All the cells within the cylinder are

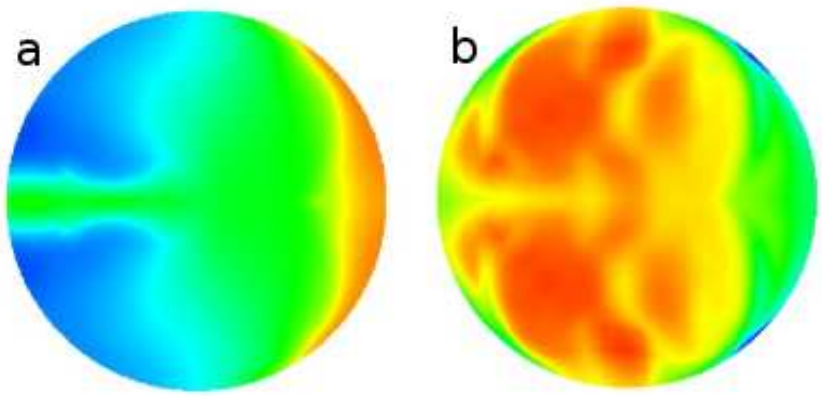

Figure 6.2: (a) Fuel mass fraction, levels ranging from 0 (blue) to 0.03 (red), (b) temperature, levels ranging from 680 K (blue) to 820 K (red) for Case (kA). Shown in a plane normal to cylinder axis close to top wall of cylinder, 15 degrees BTDC.

represented in this scatter plot. It is evident that there exists a strong negative correlation between the two fields. The lower constant temperature branch of the scatter plot represents the thermal boundary layer near the walls where the temperature is lower due to heat loss. In this case, since the fuel is injected very late, there is still a large variation in fuel mass fraction field at 15 degrees BTDC, with the equivalence ratio varying from 0 to 1.47 inside the cylinder. Note that about 60% of the fuel is evaporated at 15 BTDC in this case. Temperature again varies from about 700-800 K for majority of cells within the cylinder. Due to late fuel injection there is not enough time for turbulence mixing to modulate the effects of evaporative cooling and this causes the temperature and equivalence ratio fields to be negatively correlated.

Apart from these two cases, exhaust gas recirculation (EGR) can also result in a negatively correlated equivalence ratio and temperature fields for an early-injection or port-fuel injection case. This can happen when the overall mixture is lean and the hot EGR stream contains large levels of oxygen. Incomplete mixing between hot EGR stream and fresh charge then results in hot pockets with excess oxygen and cold pockets with lower levels of oxygen. This creates a negatively correlated temperature-equivalence ratio field. An illustration of this is shown in Babajimopolous *et al.* [11] (See Fig. 3 of Ref. [11]).

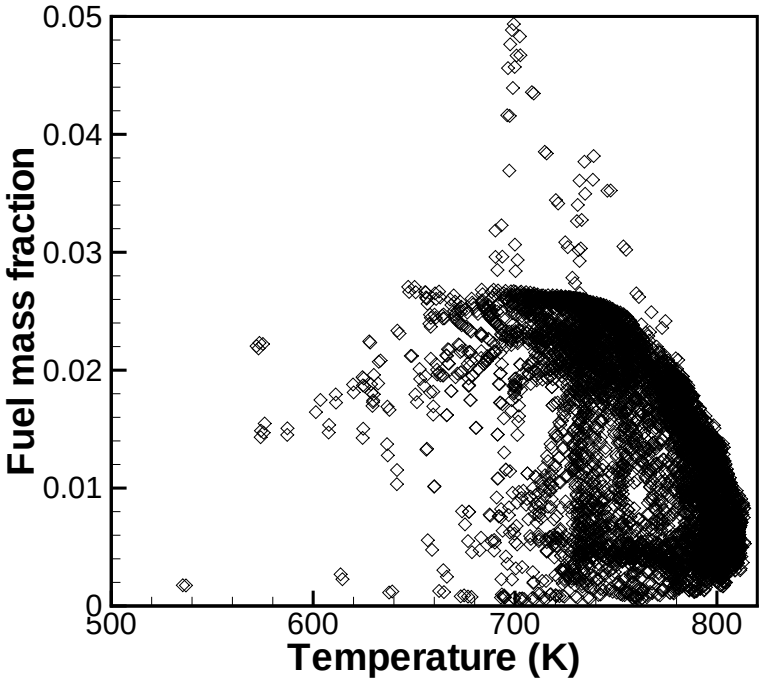

Figure 6.3: Scatter plot of temperature against fuel mass fraction at 15 degrees BTDC for Case (kA).

Having understood the different mixture formation scenarios that might exist in a real engine prior to autoignition, in the next Chapter we study the small-scale implications of these different T-ϕ correlations on autoignition and subsequent front propagation using high-fidelity DNS. There remains a question as to whether the large scale correlations observed in the RANS simulations will result in the same degree of small subgrid-scale correlations. Considering turbulent mixing characteristics, it is reasonable to assume that uncorrelated large scales will result in uncorrelated small scales. On the other hand, even if large scales are correlated, small scales might still be uncorrelated to some extent due to turbulence mixing at small scales. Further investigation is needed to provide insights into this issue.

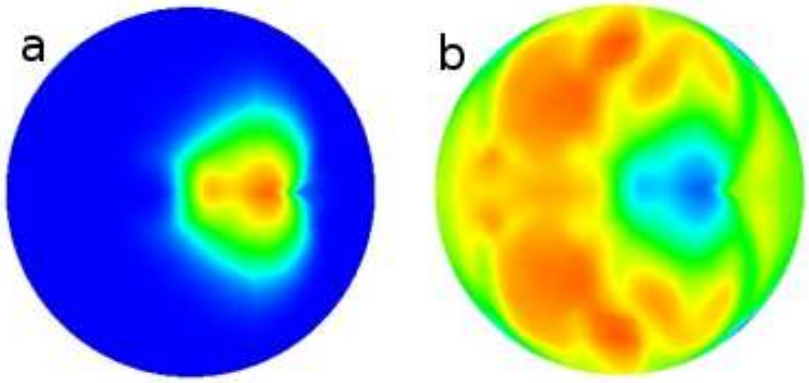

Figure 6.4: (a) Fuel mass fraction, levels ranging from 0 (blue) to 0.08 (red), (b) temperature, levels ranging from 700 K (blue) to 840 K (red) for Case (kB). Shown in a plane normal to cylinder axis close to top wall of cylinder, 15 degrees BTDC.

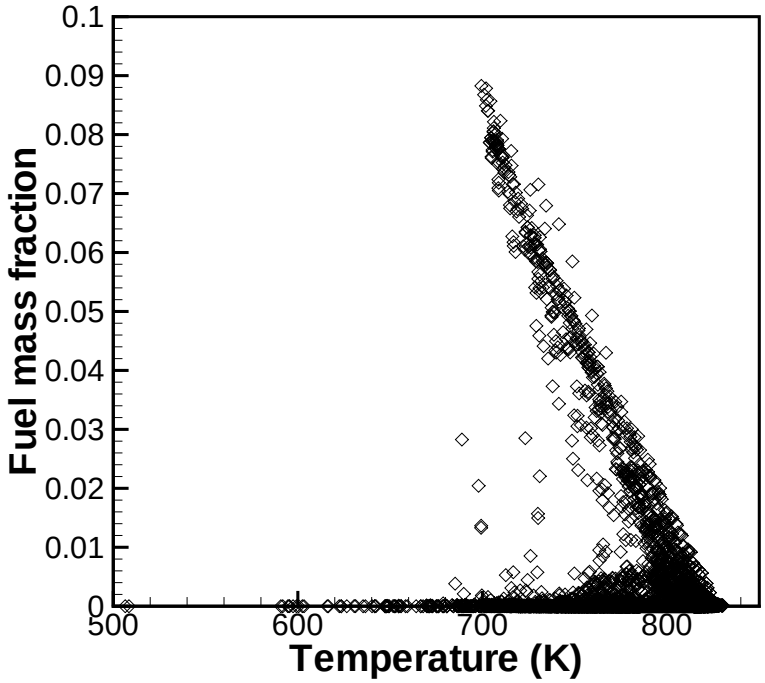

Figure 6.5: Scatter plot of temperature against fuel mass fraction at 15 degrees BTDC for Case (kB).

Chapter 7

DNS of Autoignition and Front Propagation in LTC Engine Environments

The non-reacting engine simulations conducted in the last Chapter provide guidance to representative initial scalar fields to be studied for the autoignition characteristics. In this Chapter we study the ignition and front propagation events using two-dimensional (2D) direct numerical simulation (DNS) with detailed chemistry. Based on the insights gained from non-reacting engine simulations in last Chapter, three cases with different initial conditions are studied using DNS: Case (A) is the baseline case with only temperature inhomogeneities and a uniform equivalence ratio; Case (B) is uncorrelated temperature and equivalence ratio fields; and Case (C) is negatively correlated temperature and equivalence ratio fields. Detailed spatial and temporal evolution of ignition and front propagation event as well as the integrated heat release rate behavior is examined for the three cases.

As mentioned in the Introduction Chapter, autoignition in inhomogeneous mixtures can lead to a mixed mode combustion with simultaneous presence of volumetric- and wave-like modes. Furthermore, the wave-like modes can either be a normal premixed deflagration or a spontaneously propagating ignition front [17]. Therefore, in the latter part of this Chapter, a diagnostic criterion is developed which can quantitatively distinguish between the different

modes of heat release.

7.1 Initial Conditions for DNS

In this section, we present the initial conditions and computational mesh details for DNS. Periodic boundary conditions are employed at all the boundaries to represent the constant volume ignition process. The computational domain is a 4.1 mm x 4.1 mm square with 960 x 960 grid points, which gives the grid resolution of 4.3 μm. Such a fine resolution is required for resolving the thin propagating fronts which result due to the high pressure conditions employed in this study. The 2D grid used is similar to the one used in previous studies [26, 27].

The mean flow velocities for all cases are set to 0 cm/s initially. At initial time, turbulence velocity fluctuations are superimposed on the stationary mean velocity field based on the Passot-Pouquet turbulent kinetic energy spectrum function [71]:

$$E(k) = \frac{32}{3}\sqrt{\frac{2}{\pi}}\frac{u'^2}{k_e}\left(\frac{k}{k_e}\right)^4 \exp\left[-2\left(\frac{k}{k_e}\right)^2\right] \tag{7.1}$$

where k is the wave number magnitude, k_e is the most energetic wave number and u' is the rms velocity fluctuation. In all the cases, the mean initial temperature is 1070 K, mean hydrogen-air equivalence ratio is 0.1 and the uniform initial pressure is 41 atm. Random temperature and composition fields are superimposed on the mean temperature and composition fields respectively. The temperature and equivalence ratio spectrums similar to turbulence kinetic energy spectrum are used to specify the characteristic scales of initial hot/cold spots and initial rich/lean fuel pockets respectively.

The initial autocorrelation integral length scale of the velocity fluctuations ($L_{11,u}$) is 0.34 mm and the most energetic length scale ($L_{e,u}$) is 1.0 mm. The velocity RMS (u') is 0.5 m/s. This gives integral time scale ($t_{11} = L_{11,\mathrm{u}}/u'$) of turbulent fluctuations as about 0.7 ms, and the integral scale Reynolds number of 51. In a typical engine, u' values are found to be of the order of 5 m/s, and $L_{11,\mathrm{u}}$ is of the order of 6 mm [72]. This gives the

turbulent integral time scale as 1.2 ms and the integral scale Reynolds number as 9000 for a typical engine. Thus the integral time scale employed in DNS is comparable to that of a real engine, while the integral scale Reynolds number is about 180 times smaller than that in an engine. The homogeneous ignition delay time for hydrogen ignition computed at mean temperature of 1070 K and mean equivalence ratio of 0.1 is found to be 2.46 ms, which is also comparable to ignition delay times in a typical engine. In studies of autoignition subjected to strain rate fluctuations [70, 73] presented in Chapters 4 and 5, it was found that the turbulence eddy which has a turnover time comparable to ignition delay has maximum interaction with the ignition chemistry. Since the turbulence integral time scale employed in DNS is comparable to ignition delay, the integral scale eddies are the ones that primarily interact with ignition chemistry.

The temperature and equivalence ratio fields have an RMS fluctuation of 15 K and 0.05, respectively. The autocorrelation integral length scale and most energetic length scale are 0.45 mm and 1.32 mm, respectively, for both temperature and equivalence ratio fields. Note that, as specified, $T'/\overline{T}$ (= 0.014) is much smaller than $\phi'/\overline{\phi}$ (= 0.5). This way ignition delay variation due to temperature fluctuation alone is comparable to that due to equivalence ratio fluctuation alone, considering the much stronger exponential dependence of ignition delay on temperature.

The length scales of hot spots [13] and rich fuel pockets observed in an engine are approximately five times larger than those specified in the present DNS study. However, as mentioned before, the key turbulence mixing time scale, i.e. the integral time scale, is matched with that in a typical engine. Furthermore, the level of variation in temperature (about 100 K) considered in DNS is comparable with that obtained in engine simulation results in the previous section, suggesting that T' may be comparable between DNS and a typical engine. Experimental measurements of T' in a typical LTC engine are required to further confirm this. If the key mixing time scale and T' are matched between DNS and a typical engine, local temperature gradients will also be comparable between DNS and a

typical engine (see the definition of mixing time scale in Eq. (10) of Ref. [27]). In a previous study [26], local temperature gradient is shown to be the key parameter affecting molecular transport in high heat release regions. Thus, as demonstrated by Hawkes *et al.* [28], a change in initial length scales may not affect the heat release behavior if the turbulence mixing time scale and T' are kept fixed. Based on this reasoning, the heat release behavior observed in the present DNS study is expected to be relevant in a real engine. The larger Reynolds number present in the engine will only contribute towards producing a larger range of scales.

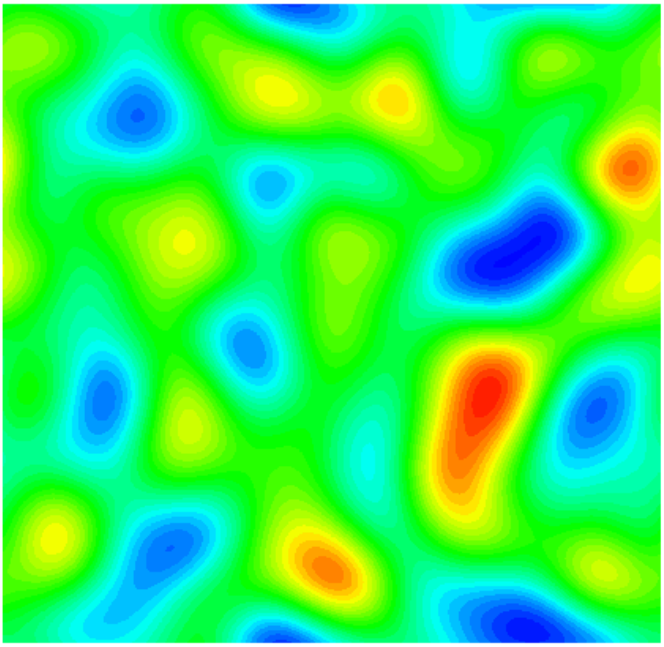

Figure 7.1: Initial temperature field for Cases (A), (B), and (C), levels ranging from 1033 K (blue) to 1116 K (red).

Three cases with different initial conditions are studied using DNS. Case (A) is the baseline case with only temperature inhomogeneities and a uniform equivalence ratio of 0.1; Case (B) is uncorrelated temperature and equivalence ratio fields; and Case (C) is negatively correlated temperature and equivalence ratio fields. Figure 7.1 shows the initial temperature field which is same for all three cases. The figure shows how the hot and cold

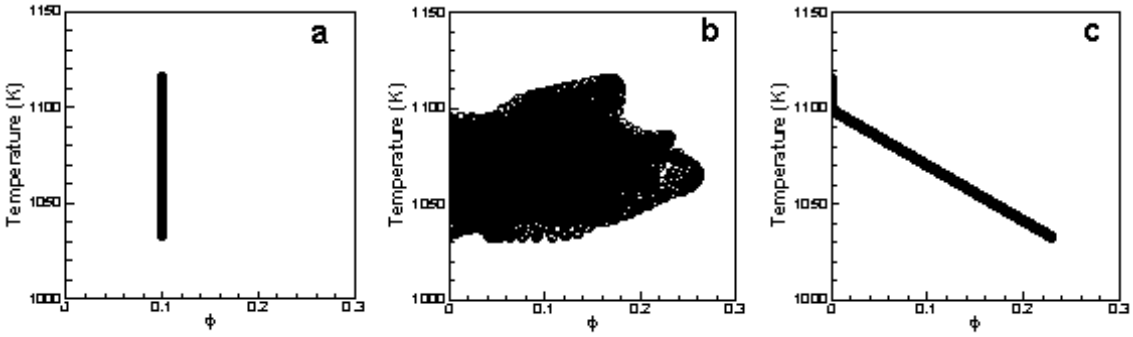

Figure 7.2: Temperature-equivalence ratio scatter plot at initial time for a: Case (A), b: Case (B), and c: Case (C).

spots of different length scales are superimposed on the mean temperature field. Figure 7.2 shows the scatter plot of initial equivalence ratio and temperature fields for the three cases. Note that in Cases (B) and (C) the equivalence ratio distribution has to be slightly truncated at the lean end to prevent it from becoming negative. The variation in equivalence ratio specified in Cases (B) and (C) is smaller than that observed in non-reacting engine simulations in the last Chapter. If equivalence ratios greater than one are present, which is more probable for the late-injection case, there is a possibility of formation of diffusion flames in the engine. High equivalence ratios are not employed in DNS because in high pressure hydrogen-air mixture there is a tendency to form shock waves at high equivalence ratios which the present DNS grid may not resolve.

7.2 DNS Results

As mentioned in last section, results for three different cases are presented here. Case (A) is the baseline case with just temperature inhomogeneities and a uniform equivalence ratio of 0.1. Case (B) is the case with initially uncorrelated temperature and equivalence ratio fields. This case represents the early-injection scenario shown in Chapter 6. Finally, Case (C) is the case with initially negatively correlated temperature and equivalence ratio fields, representing the late-injection scenario of Chapter 6.

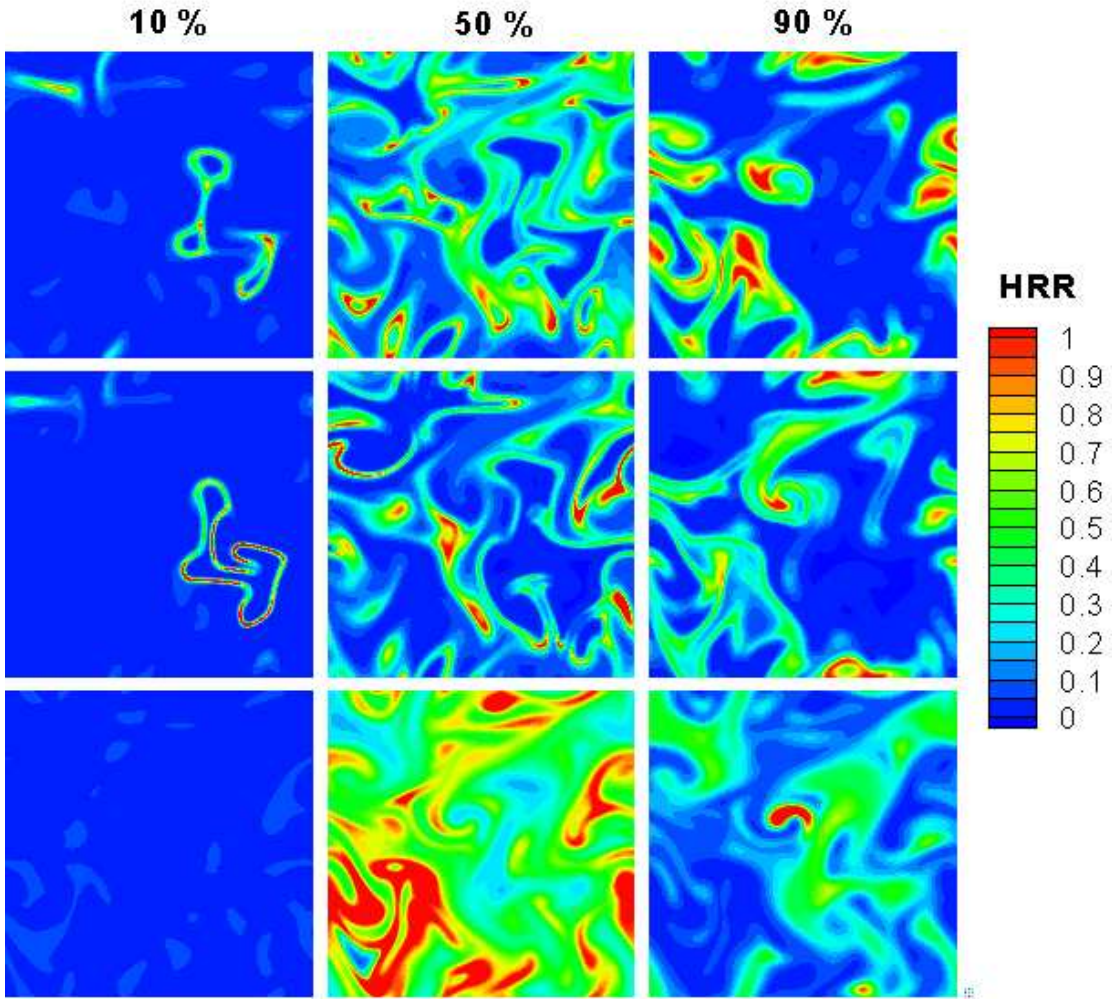

Figure 7.3: HRR contours at 10%, 50% and 90% heat release points. Top row: Case (A), middle row: Case (B), bottom row: Case (C). Levels ranging from 0 (blue) to 1 (red).

Figure 7.3 shows the normalized heat release rate (HRR) contours for the three cases (A), (B) and (C) at three different time instants corresponding to 10%, 50% and 90% of total heat release. The normalization is done by the maximum heat release rate for a zero-dimensional ignition case with initial conditions as the mean initial conditions taken in 2D DNS, i.e. T_0 = 1070 K, ϕ_0 = 0.1, and P = 41 atm. All the plots shown in this figure have same color scheme and the HRR levels vary from 0 (blue) to 1 (red). The top row shows the contours for Case (A). At 10% heat release, thin reaction fronts are observed and a weak ignition kernel is also seen at top left corner of the domain. The fronts are initiated from ig-

nition kernels at high temperature locations, and expand and consume neighboring charge. The constant volume simulation causes the pressure to rise as the fronts expand. At 50% heat release point, a large number of reaction zones are developed and heat release occurs in both thin front like regions and thick blobs. Finally, at 90% heat release, mostly thick reaction zones are seen, at which time the end charge is consumed almost homogeneously.

The middle row of Fig. 7.3 presents the results for Case (B). The development of ignition kernel and subsequent front propagation is similar to Case (A). Case (B), however, shows a much more connected reaction front at 10% heat release point. At 50% heat release point, most of the heat release occurs in thin front-like regions. At 90% heat release point, heat release is more widespread in both thin and thick regions. Thus, both Case (A) and Case (B) exhibit a mixed mode combustion with both front-like propagation and homogeneous ignition blobs simultaneously present in the domain at various stages of the ignition event.

Finally, the bottom row shows the results for Case (C), which shows a drastically different ignition event. At 10% heat release, no front-like propagation is seen, and heat release occurs homogeneously. At 50% heat release, thick structures are seen, implying that the heat release occurs almost homogeneously. Such a homogeneous evolution of heat release is sustained throughout the ignition event. Therefore, it is evident that Case (C) represents a typical homogeneous ignition mode without any front propagation. This is because the hot temperature regions have very low fuel available due to the initial negative T-ϕ correlation. Therefore, the radical build-up slowly starts outside of the hot temperature zones in the bulk of the mixture, and eventually the diffusion of fuel and radicals leads the hotter temperature zones to ignite subsequently.

Figure 7.4 shows the temperature contours for the three cases (A), (B) and (C) at the same time instants as those in Fig. 7.3. It can be seen that large temperature gradients exist in the domain for cases (A) and (B), whereas largely homogeneous temperature field is observed for case (C). This follows the discussion on Fig. 7.3 above, in that thin reaction

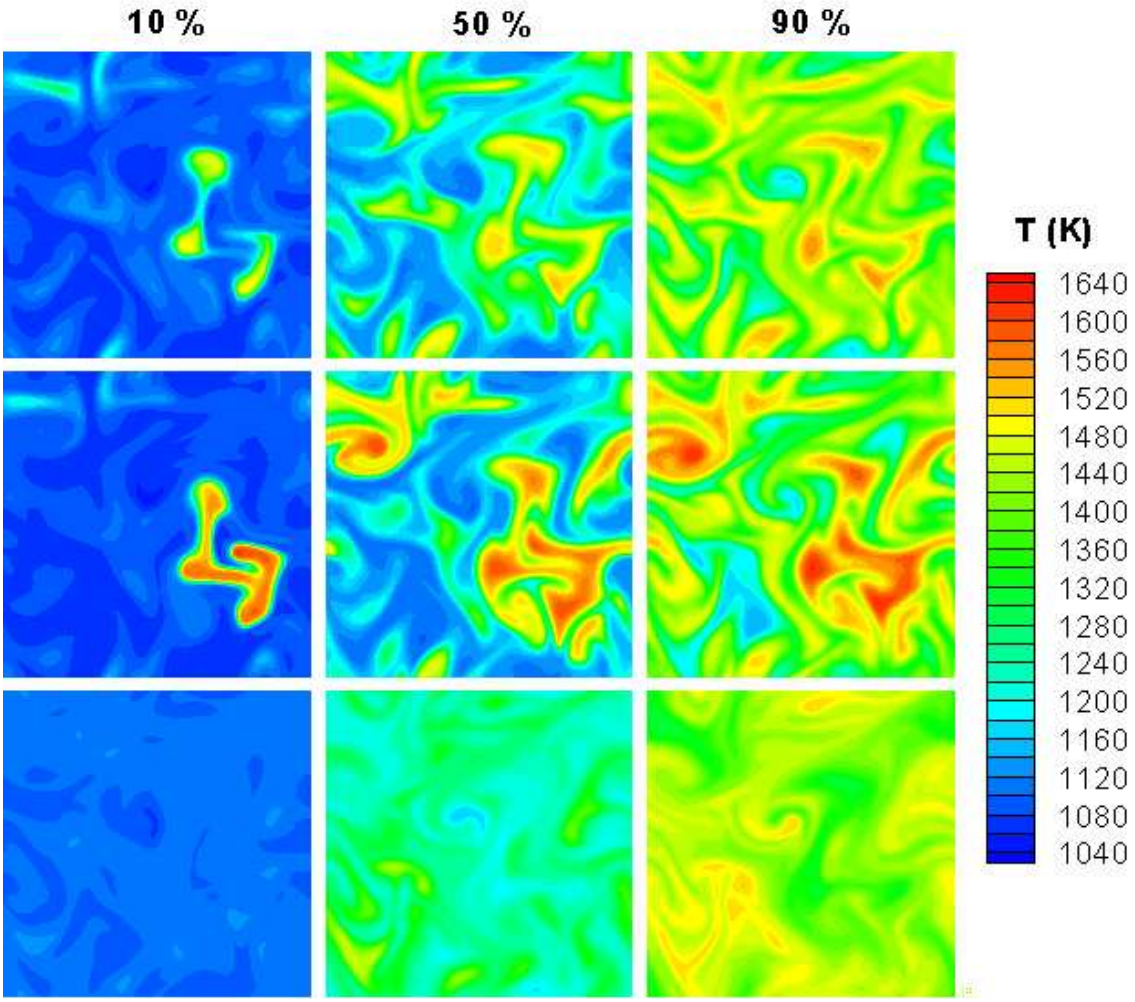

Figure 7.4: Temperature contours at 10%, 50% and 90% heat release points. Top row: Case (A), middle row: Case (B), bottom row: Case (C). Levels ranging from 1040 (blue) to 1640 (red).

fronts are observed in cases (A) and (B), whereas largely homogeneous autoignition is observed in case (C).

Figure 7.5 shows the normalized integrated heat release rate as a function of time for the three cases. Again, the normalization is done by the maximum integrated heat release rate of the same zero-dimensional (0D) case as before, with domain dimensions same as that for 2D DNS. Figure 7.5, also shows the plot for the zero-dimensional case, for comparison. Compared to Case (A), the ignition delay is advanced for Case (B) and delayed for Case

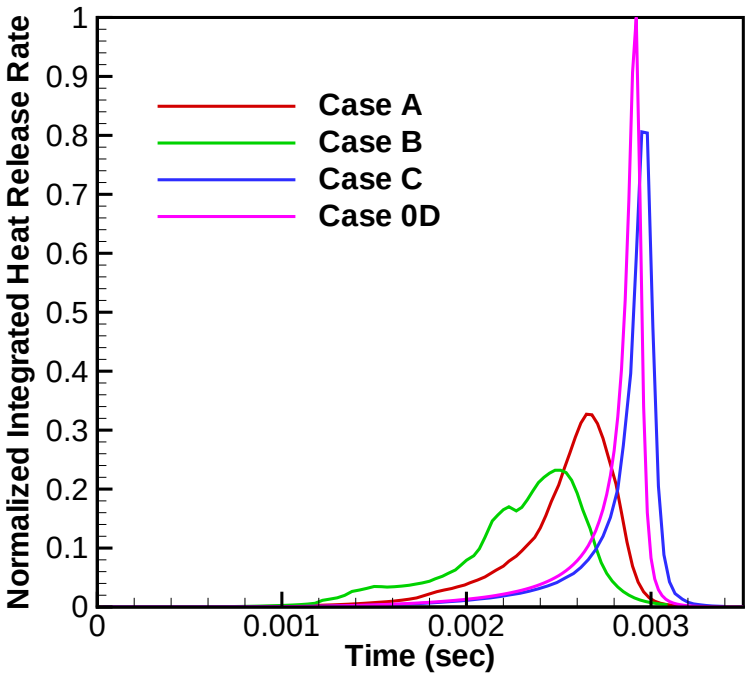

Figure 7.5: Normalized integrated heat release rate as a function of time for Cases (A), (B) and (C). 0D case is also shown for comparison.

(C). In Case (B), since the temperature and equivalence ratio are uncorrelated, there are regions in the domain which have high temperature as well as high equivalence ratio. This causes the ignition in these regions to initiate very early. On the other hand, in Case (C) there is a prolonged ignition delay since ignition is initiated outside of the local hot spots. The duration of heat release is also increased for Case (B) and decreased for Case (C) compared to Case (A). Consequently, peak heat release rate is high for Case (C) and low for Case (B). It is observed that the plot for Case (C) is very similar to that for 0D case, which is expected since Case (C) is found to ignite pretty much homogeneously.

7.3 Numerical Diagnostics

In this section, several one-dimensional (1D) simulations are conducted to develop a quantitative criterion for demarcating the three different modes of heat release: homogeneous

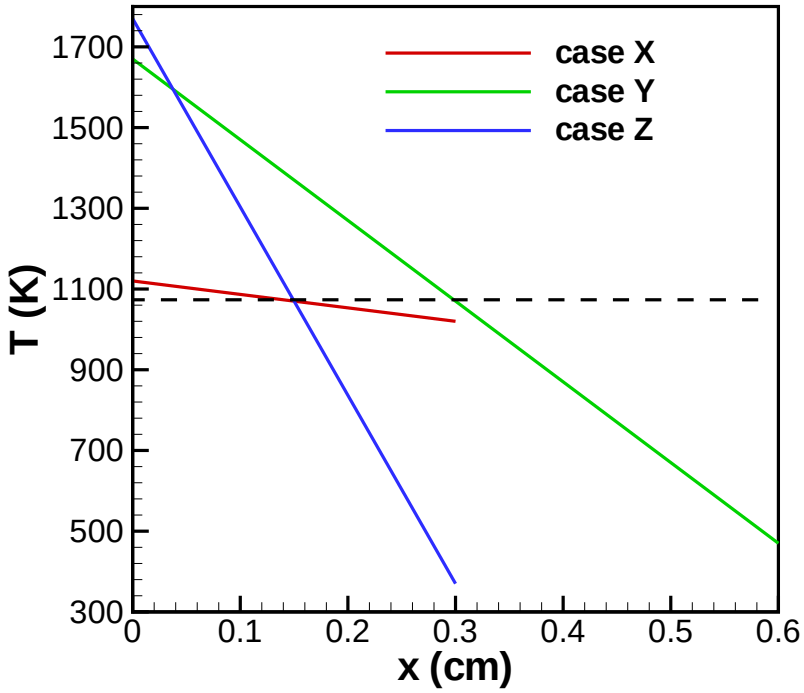

Figure 7.6: Initial temperature profiles for cases (X), (Y), and (Z)

autoignition, spontaneous ignition front propagation, and premixed deflagration. Ignition and front-propagation regimes in non-homogeneous 1D configuration has been investigated in some previous studies [74–76]. Three cases with different initial temperature profiles as shown in Fig. 7.6 are studied. A linear temperature field with different temperature gradients (case (X) - 33.34 K/mm ; case (Y) - 200 K/mm; and case (Z) - 466.67 K/mm) is imposed on the mean temperature field at initial time. For all cases, mean temperature, pressure and hydrogen-air equivalence ratio are fixed to 1070 K, 41 atm, and 0.1, respectively. The computational domain size is 0.3 cm for cases (X) and (Z), and 0.6 cm for case (Y) in order to capture a comparable duration of computation with its faster front propagation speed.

Fig. 7.7 shows the time sequence of normalized heat release rate (HRR) profiles for the three cases, with increasing numbers representing increasing time. The normalization

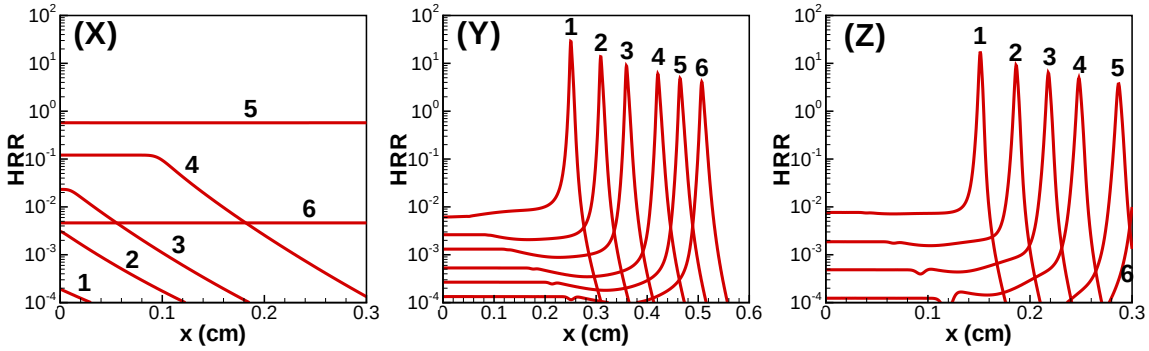

Figure 7.7: HRR profiles at various time instants during the entire combustion event for cases (X), (Y), and (Z). The numbers indicate the time sequence of the combustion event.

is done similarly to the 2D DNS cases. Due to the different ignition delays and different duration of heat release for the three cases, the corresponding numbers represent different times for the three cases. For case (X), it is observed that combustion occurs almost homogeneously over a wide region. For cases (Y) and (Z), on the other hand, a wave-like front propagates from the hot left boundary to the cold right boundary.

Fig. 7.8 shows the plot of normalized integrated heat release rate. Normalization is done again similar to 2D DNS cases. Both axes are shown on a log-scale to cover the entire range for the three cases. It is evident that case (X) shows a distinct heat release history compared to cases (Y) and (Z). Case (X) shows a prolonged ignition delay compared to cases (Y) and (Z) because of a lower initial maximum temperature. Cases (Y) and (Z) ignite almost instantaneously. There is a sharp drop in heat release at about 0.1 ms for cases (Y) and (Z), as the fronts leave the domain. Note that the computational domain for case (Y) is double the size of the domain for case (Z); however, the fronts exit the domain at approximately the same time. This is because the speed of the front in case (Y) is greater than that in case (Z).

The nature of the front propagation, i.e. whether it is a spontaneous ignition front or a premixed deflagration, is still not clear for cases (Y) and (Z). A quantitative diagnostic criterion is now sought to identify the ignition regimes. A steadily propagating premixed

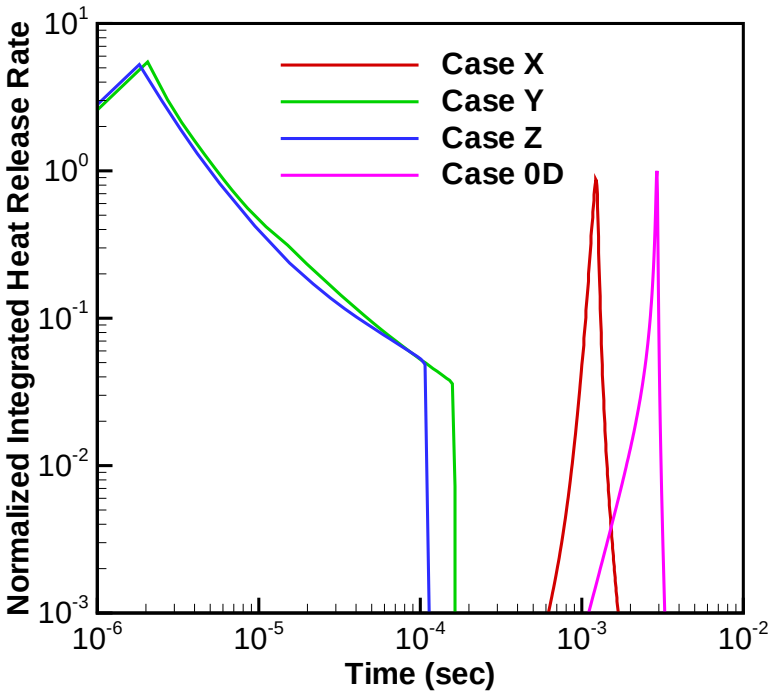

Figure 7.8: Normalized integrated heat release rate as a function of time for cases (X), (Y) and (Z).

flame will have almost equal contribution from reaction and diffusion processes, while a spontaneous ignition front propagation is a chemistry-driven sequential explosion of neighboring mixture in the presence of temperature/concentration gradient [17]. This suggests that comparison of the magnitude of diffusion and reaction is the key observable in determining the ignition characteristics.

Fig. 7.9 shows the spatial profiles of diffusion (red lines) and reaction (blue lines) terms in the HO_2 species conservation equation, considering that HO_2 is one of the key intermediate species during ignition and correlates well with the heat release rate. The time instants for the three cases correspond to that for number 4 in Fig. 7.7. For case (X), the reaction occurs within a widespread region, while the diffusion term is almost negligible. Comparing case (X) with case (Y) or (Z), a quantitative criterion to distinguish ignition regimes is suggested: if the mixture ignites homogeneously, the reaction rate of HO_2 must be positive

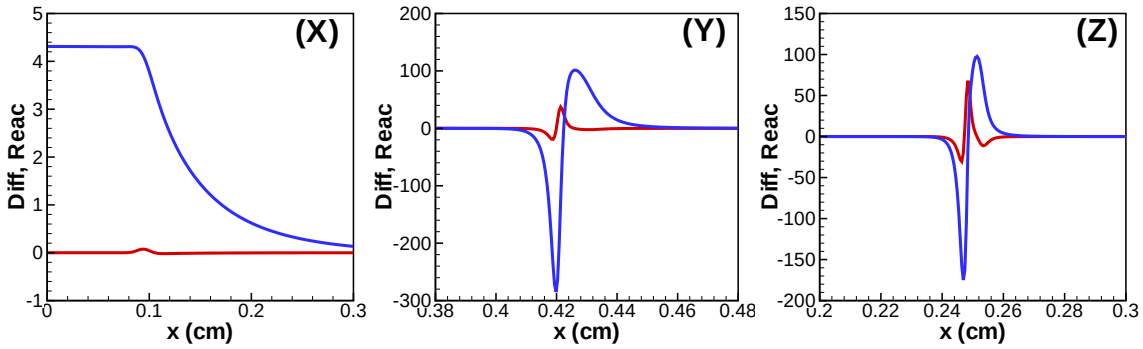

Figure 7.9: Diffusion (red lines) and reaction (blue lines) term profiles for cases (X), (Y), and (Z). The time instants for the three cases correspond to that for number 4 in Fig. 7.7.

throughout the induction period. On the other hand, if a wave-like propagation occurs, the reaction rate profile of HO_2 must transition from negative to positive as one goes from burnt products to unburnt reactants side. Between cases (Y) and (Z), it is observed that the positive peak of diffusion is much smaller than that of reaction for case (Y), while they are comparable for case (Z). Therefore, case (Y) represents a chemistry-driven spontaneous ignition front, and case (Z) represents a deflagration front propagation in which reaction is balanced with diffusion.

Based on the above observation, a characteristic Damköhler number is defined which represents the ratio of the positive peaks of reaction and diffusion of HO_2 within the front:

$$\mathrm{Da}_{\mathrm{HO}_2} = \frac{\max(\omega_{\mathrm{HO}_2})}{\max(\nabla.(-\rho D_{\mathrm{HO}_2} \nabla Y_{\mathrm{HO}_2}))} \tag{7.2}$$

where the maximum values closest to the reaction zone are taken for both reaction and diffusion terms. Since the peaks of reaction and diffusion are not collocated, the Damköhler number based on the local reaction and diffusive terms may lead to a misleading result. This problem becomes more serious in analyzing 2D results. To locate the correct peaks of reaction and diffusion, a gradient ascent algorithm is used. Starting from the point where the reaction terms transitions from negative to positive, two separate numerical markers

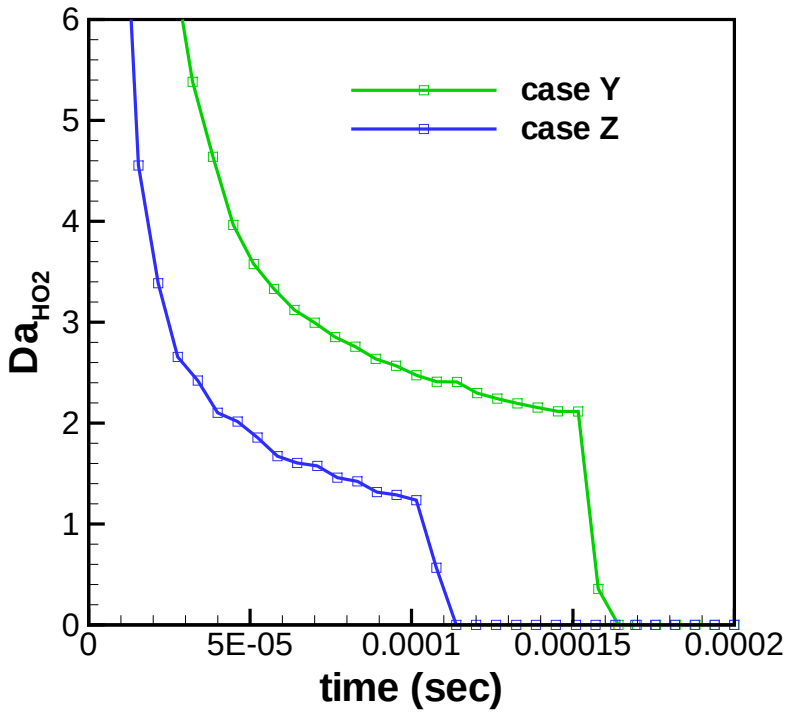

Figure 7.10: Damköhler number history for cases (Y) and (Z).

trace along the reaction and diffusion profiles until the respective maximum is reached. For 2D cases a two-dimensional gradient ascent algorithm is employed.

Fig. 7.10 shows the time history of the Damköhler number for cases (Y) and (Z). Since there is only one front in the domain at any particular time, there is only one value of Damköhler number at any given time. It is seen that case (Y) has higher values of $\mathrm{Da_{HO_2}}$ than case (Z). For cases (Y) and (Z), $\mathrm{Da_{HO_2}}$ asymptotes to values close to 2 and 1, respectively. This clearly indicates that the front in case (Y) is more chemistry-dominant and that in case (Z) is deflagrative in nature. This Damköhler number criterion proposed using 1D tests is now applied to the 2D DNS results presented in the last section.

Figs. 7.11(a), (b) and (c) show the results for cases (A), (B), and (C), respectively. The left, middle, and right plots show the results at time instants corresponding to 10%, 30% and 50% heat release points, respectively. The color field in the background represent

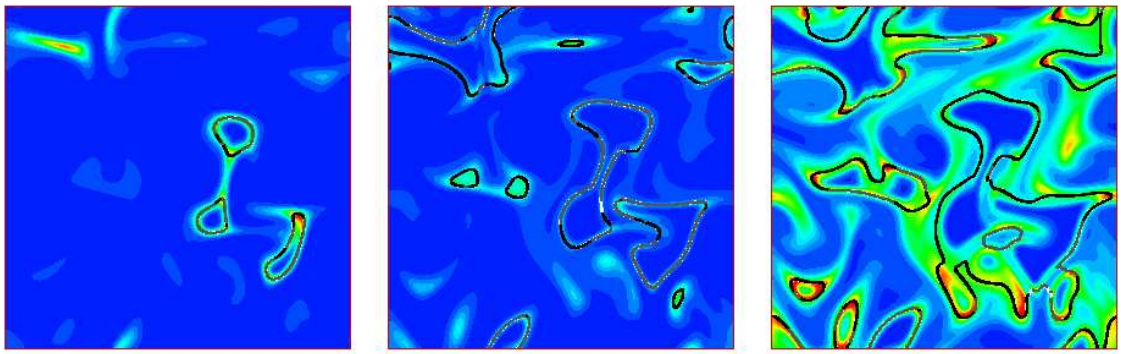

(a) Case A

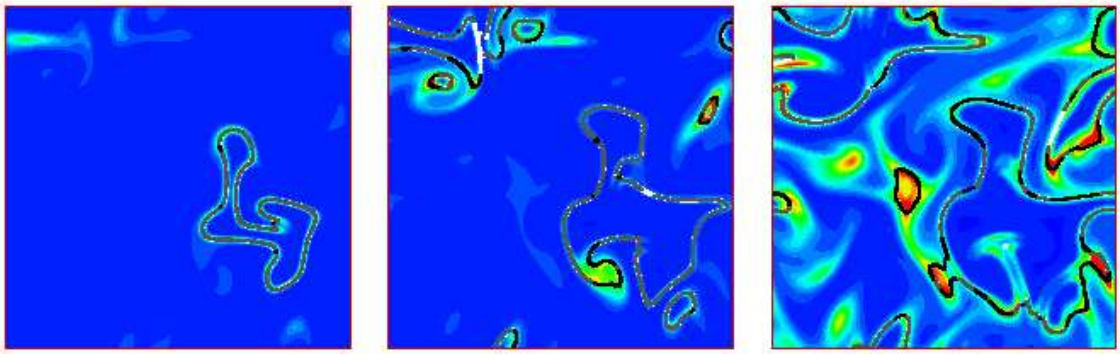

(b) Case B

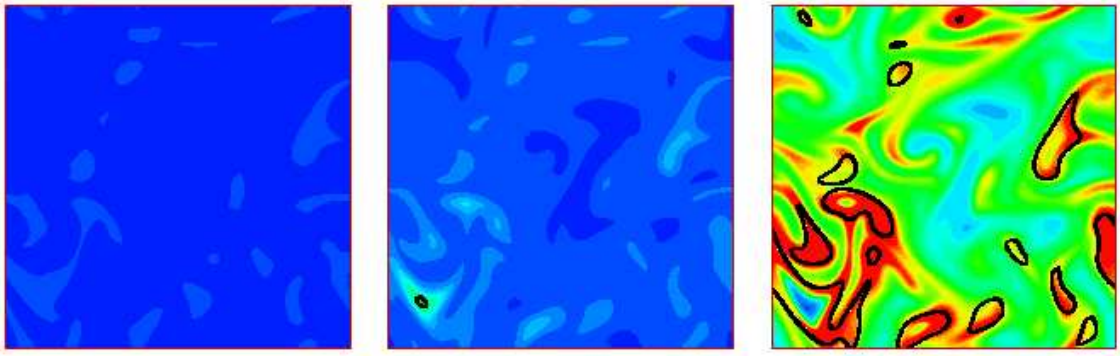

(c) Case C

Figure 7.11: Normalized heat release rate (color field), levels ranging from 0 (blue) to 1 (red). Da_{HO_2} contour is overlaid at locations of the propagating front, Da_{HO_2} levels: 0-0.4 (white), 0.4-1.4 (gray), > 1.4 (black). The left, middle, and right plots show the results at time instants corresponding to 10%, 30% and 50% heat release points, respectively.

the normalized heat release rate, same as Fig. 7.3. The overlaid connected contour lines represent the location of propagating front, identified by the locations where reaction rate of HO_2 transitions from negative to positive. This contour line is colored white, gray, and black, representing different range of Da_{HO_2} values to demarcate, respectively, a quenching premixed flame ($Da_{HO_2} < 0.4$), a deflagration front ($0.4 < Da_{HO_2} < 1.4$), and a spontaneous ignition front ($Da_{HO_2} > 1.4$). Note that the white colored segments of the front are subjected to quench only in a quasi-steady sense; it may not necessarily lead to an actual extinction considering the highly transient process. The values 0.4 and 1.4 are chosen arbitrarily, but other $O(1)$ values also lead to qualitatively consistent results. The high heat release regions without a contour line represent homogeneously igniting regions.

The characteristic Damköhler number in equation (7.2) therefore proves to be a rational way to identify different ignition regimes even in complex multi-dimensional simulation results. In case (A) at 10% heat release as an example, the criterion clearly distinguishes a homogeneous ignition kernel (top left) from a front (middle) which is further divided into the spontaneous ignition front and deflagration. It is observed that combustion always initiates in homogeneous ignition kernel, which may or may not evolve into either propagation front. At 50% heat release for case (A), a larger fraction of the front is burning in the spontaneous ignition front regime, due in part to the additional pressure rise resulting from compression heating enhancing chemical reactions in the reactant mixture. For case (B), the fronts develop due to earlier ignition, which is allowed a longer time to develop deflagration fronts. This explains why a larger fraction of the front appears in the deflagration mode at 30% and 50% heat release. In the negatively-correlated mixture case (C), ignition is predominantly homogeneous, and some level of the spontaneous front propagation emerges at 50% heat release point, yet the bulk of the mixture remains in the homogeneous ignition regime.

The results presented in the last and the present Chapter can be summarized as follows. It is found that inhomogeneities indeed have a significant effect on the various aspects of

combustion in LTC engines: ignition delay, duration of heat release, peak heat release rate, and the nature of combustion phenomena are all dictated by inhomogeneities in various scalars. In Chapter 6, it is found that different fuel injection strategies can result in different T-ϕ correlations close to TDC prior to autoignition. And in the present Chapter it is found that apart from the magnitude of these inhomogeneities, the correlations between temperature and equivalence ratio inhomogeneities also play a key role in governing the nature of combustion in LTC engines.

Chapter 8

A Principal Component Analysis Based Approach for Modeling Autoignition in Inhomogeneous Turbulent Mixtures

Upto this point, we have obtained fundamental physical insights of the complex combustion process occuring in LTC engines through a variety of computational models such as 0D homogeneous reactor, 1D counterflow configuration, and 2D direct numerical simulation. Optmial development of LTC engines also require simulations of realistic engine geometries using RANS/LES based models. For these models, physics based predictive combustion submodels are required which can represent the complex mixed-mode combustion process with good fidelity. Therefore, in this last part of the dissertation, we focus on the modeling aspects of LTC combustion in the context of RANS/LES. As mentioned in the Introduction Chapter, development of combustion submodels for autoignition in inhomogeneous mixtures is especially difficult due to the following two reasons: Firstly, the phenomena is highly chemical in nature and therefore detailed chemistry must be included in the model, and, secondly, an *a-priori* low-dimensional subspace is not available in which the fluctuations of reacting scalars is small. In view of these difficulties, the objective of this Chapter is to identify, in a mathematically rigorous way, a low-dimensional manifold for the autoignition problem studied using DNS in Chapter 7. For this purpose, we will use a novel methodology based on Principal Component Analysis (PCA). To apply PCA, high fidelity datasets from either experiments or DNS are required. In this Chapter, PCA will be applied to DNS database generated in Chapter 7, and low-dimensional manifolds

will be identified. The mathematical formulation of PCA is given in the next section, followed by description of PCA modeling approach. Finally, results of PCA application will be presented.

8.1 Mathematical formulation of PCA

The details of the mathematical formulation of PCA is given elsewhere [39, 40]. A brief description is given here as follows. The goal of PCA is to compute the most meaningful basis to re-express the original data-set. PCA finds a basis which is a *linear* combination of the original basis. Let **X** be a mxn matrix representing the dataset, where m is the number of variables and n is the number of observations. Then one can define a covariance matrix ($\mathbf{C_X}$) as:

$$\mathbf{C_X} \equiv \frac{1}{n-1}\mathbf{X}\mathbf{X}^T \tag{8.1}$$

The covariance matrix has the following properties:

- The diagonal terms of $\mathbf{C_X}$ are the *variances* of particular variables, and therefore, large values of diagonal terms correspond to interesting dynamics of the system.

- The off-diagonal terms of $\mathbf{C_X}$ are the *covariances* between variables, and therefore, large (small) values of off-diagonal terms correspond to high (low) redundancy in the system.

Thus, by diagonalizing covariance matrix the redundancy in the system is minimized and the *signal* is maximized. PCA is essentially a method of diagonalizing the covariance matrix. In other words, given the data-set **X**, the goal is to find a matrix **P**, where **Z** = **PX**, such that $\mathbf{C_Z}$ is diagonalized. The rows of **P** are then the coefficents representing

orthogonal principal components of **X**. It is done as follows:

$$\begin{aligned}
\mathbf{C_Z} &= \frac{1}{n-1}\mathbf{Z}\mathbf{Z}^T && (8.2)\\
&= \frac{1}{n-1}(\mathbf{P}\mathbf{X})(\mathbf{P}\mathbf{X})^T && (8.3)\\
&= \frac{1}{n-1}\mathbf{P}\mathbf{X}\mathbf{X}^T\mathbf{P}^T && (8.4)\\
&= \frac{1}{n-1}\mathbf{P}\mathbf{A}\mathbf{P}^T && (8.5)
\end{aligned}$$

where, a new symmetric matrix **A** = $\mathbf{X}\mathbf{X}^T$ is defined, which can be diagonalized as $\mathbf{A} = \mathbf{E}\mathbf{D}\mathbf{E}^T$. Here **D** is a diagonal matrix and **E** is a matrix of eigen-vectors of **A** arranged as columns. Now, matrix **P** is selected such that each row of **P** is an eigen-vector of $\mathbf{X}\mathbf{X}^T$. Thus, **P** = $\mathbf{E}^T$, and also since **P** is orthogonal, $\mathbf{P}^{-1}$ = $\mathbf{P}^T$. Therefore, continuing the derivation:

$$\begin{aligned}
\mathbf{C_Z} &= \frac{1}{n-1}\mathbf{P}\mathbf{A}\mathbf{P}^T && (8.6)\\
&= \frac{1}{n-1}\mathbf{P}(\mathbf{P}^T\mathbf{D}\mathbf{P})\mathbf{P}^T && (8.7)\\
&= \frac{1}{n-1}(\mathbf{P}\mathbf{P}^{-1})\mathbf{D}(\mathbf{P}\mathbf{P}^{-1}) && (8.8)\\
&= \frac{1}{n-1}\mathbf{D} && (8.9)
\end{aligned}$$

Thus, this choice of **P** diagonalizes $\mathbf{C_Z}$.

The first principal component (PC) accounts for as much of the variability in the data as possible (has the largest eigen-value), and each succeeding component accounts for as much of the remaining variability as possible, and therefore, a truncated set of this new basis is sufficient to represent the original system. We define a transformation matrix **T** as a rank-deficient subset of **P** matrix with m_η ($< m$) rows and m columns. The rows of **T** correspond to rows of **P** with m_η largest eigen-values. We may then approximate **X** as:

$$\mathbf{X} \approx \mathbf{T}^T\mathbf{Z}_\eta \qquad (8.10)$$

where $\mathbf{Z}_\eta$ is the matrix with m_η rows corresponding to m_η principal components. In the present study, only first two principal components (p_1 and p_2) are found to very well parameterize all the reactive scalar variables for the DNS data-sets considered.

A MATLAB based code was written to evaluate the principal components (PCs). The parameterization of reactive scalars on a low-dimensional space is not a trivial problem. This is especially true for parameterizing the source terms of PCs. An advanced regression technique is required to parameterize the original variables in low-dimensional space in a statistically meaninful way. Simple linear regression techniques might not do a good job. A hypercube based algorithm is employed for this purpose. The basic idea of this algorithm is to create hypercubes by recursively partitioning the low-dimensional space and simultaneously merging the hypercubes keeping the number of points in the hypercube in a certain range. The parameterized value of any variable at a given location can then be obtained as the average of observed values of that variable for points in a hypercube centered at that location.

8.2 PCA Modeling Approach

A complete PCA modeling approach requires several ingredients. Firsly, following the theory given in last section, PCs must be identified using high-fidelity DNS or experimental database. Next, the transport equations for PCs may be derived and solved. Following Sutherland and Parente [37] the transport equations for PCs are derived as follows. The transport equations for a set of reactive scalars $\mathbf{\Phi}$ = [T, Y_1, Y_2,....,Y_{nsp-1}], where nsp is the total number of species, may be written as:

$$\frac{\mathrm{D}(\mathbf{\Phi})}{\mathrm{D}t} = -\nabla.(\mathbf{j_\Phi}) + (\mathbf{s_\Phi}) \tag{8.11}$$

where $\frac{\mathrm{D}}{\mathrm{D}t} \equiv \rho\frac{\partial}{\partial t} + \mathbf{u}.\nabla$ is the material derivative operator, $\mathbf{u}$ is the mass-averaged velocity of the system, $\mathbf{j_\Phi}$ is the mass-diffusive flux of $\mathbf{\Phi}$ relative to the mass-averaged velocity,

and $\mathbf{s_\Phi}$ is the volumetric rate of production of $\mathbf{\Phi}$. As will be demonstrated in next section, in this study, PCA is applied on a database consisting of entire time-history of ignition event, and therefore, the matrix $\mathbf{T}$ is a fixed constant in space-time. Since PCA is a linear transformation, after multiplying Eq.(8.11) by T, with $\mathbf{X} = \mathbf{\Phi}$, we get transport equations of PCs as:

$$\frac{\mathrm{D}(\mathbf{Z}_\eta)}{\mathrm{D}t} = -\nabla.(\mathbf{j}_{\mathbf{Z}_\eta}) + (\mathbf{s}_{\mathbf{Z}_\eta}) \tag{8.12}$$

where ($\mathbf{Z}_\eta$)=[$\mathbf{T}$]($\mathbf{\Phi}$), $\mathbf{j}_{\mathbf{Z}_\eta} = [\mathbf{T}](\mathbf{j}_{\mathbf{\Phi}})$ and $\mathbf{s}_{\mathbf{Z}_\eta} = [\mathbf{T}](\mathbf{s}_{\mathbf{\Phi}})$. In Eq. (8.12), the source terms of temperature, and *all* species contribute to the source term for each PC. Therefore, the source terms of PCs must also be parameterized in the low-dimensional space to completely reduce the dimension of the system. This issue is dealt with in Section 8.3.3. To solve the transport equations for PCs initial and boundary conditions are also required. As is discussed in Ref. [37], they can also be prescribed using the transformation matrix $\mathbf{T}$.

For turbulent flow modeling in the context of RANS/LES based models, favre averaged/filtered transport equations for pricipal components need to be solved. For this, closure for favre averaged/filtered source terms of principal components is required. Depending on number of PCs and their spatial correlation, one may consider presumed PDF approaches or transported PDF models. This is a subject of future studies.

It should also be noted that we can apply the PCA modeling approach mentioned above for a class of physical problems which are similar to the DNS database which was originally used to obtain PCs. For example, if we use a DNS database of autoignition and front propagation in premixed systems to obtain PCs, then we can use these PCs to model combustion in similar kind of systems. We may not be able to use these PCs to model, for example, non-premixed systems. So, one may only use PCs to model systems for which they were *trained* to work for. It still remains to be seen how much the principal components vary if one applies PCA to different systems, for example, how much they vary when PCA is applied to non-premixed systems compared to premixed systems. To make the applicability more general, one may consider combining the DNS databases for a large

set of problems spanning both non-premixed and premixed systems and then apply PCA to this database. This will *train* the principal components to work for a large set of problems.

8.3 Results and Discussion

In the following, PCA is applied to the physical problem of constant volume auto-ignition in high pressure inhomogeneous turbulent mixtures. The DNS data-set generated in a recent study [77] and presented in Chapter 7 of this dissertation is used. Detailed hydrogen-air chemistry [58] was used in DNS. Initial pressure was fixed to 41 atm and initial mean hydrogen-air equivalence ratio was fixed to 0.1 for all cases. For other computational details see Ref. [77] or Chapter 7. Two cases with different initial conditions are investigated in the present study: case (A) (corresponds to case (A) of Chapter 7) with only temperature (T) inhomogeneities and uniform equivalence ratio (ϕ) field, and case (B) (corresponds to case (C) of Chapter 7) with negatively-correlated T-ϕ fields. As is shown in Chapter 7, case (A) represents a mixed mode of combustion with the presence of homogeneous auto-ignition, ignition front propagation and premixed flame propagation, and case (B) represents a largely homogeneous autoignition mode. A data-set consisting of data at 11 different time instants is compiled from DNS database. Each time instant corresponds to a subsequent 10$\%$ (of total heat release) rise in heat release. Data at each time instant consists of 2304 spatially sampled points. Thus, the total number of points in the data-set are fixed to 25344. The variables in the data-set consists of temperature and nine chemical species. The data-set thus represents the entire time-history of the ignition and front propagation event. Centering and scaling of data can have significant effects on the results obtained using PCA. In the present study, data is centered about the means and scaled with the standard deviations of the corresponding variables.

	T	Y_{H_2}	Y_{O_2}	Y_O	Y_{OH}	Y_{H_2O}	Y_H	Y_{HO_2}	$Y_{H_2O_2}$	Y_{N_2}
p_1	0.400	-0.395	-0.406	0.278	0.393	0.405	0.118	-0.074	-0.292	0.138
p_2	-0.035	0.009	0.037	0.382	0.044	-0.037	0.601	0.625	0.279	-0.137

Table 8.1: Coefficient matrix for principal components for case (A)

	T	Y_{H_2}	Y_{O_2}	Y_O	Y_{OH}	Y_{H_2O}	Y_H	Y_{HO_2}	$Y_{H_2O_2}$	Y_{N_2}
p_1	0.402	-0.369	-0.403	0.325	0.398	0.403	0.191	0.023	-0.277	-0.016
p_2	0.094	-0.136	-0.077	-0.310	-0.056	0.088	-0.564	-0.642	-0.338	0.120

Table 8.2: Coefficient matrix for principal components for case (B)

8.3.1 Application of PCA

The results of application of PCA to case (A) will be examined first. Table 8.1 shows the entries of the coefficient matrix (c_{ij}) representing the principal components for the first two principal components (p_1, p_2). PCs are given as: $p_i = \sum_{j=1}^{nsp+1} c_{ij}\varphi_j$. Here, nsp is the number of species (= 9) and φ_j is the j^{th} reactive scalar, $j = 1$ being the temperature. It is observed that p_1 has large contributions from temperature and almost all major and minor species. For p_2, primary contributions come from Y_O, Y_H, Y_{HO_2}, $Y_{H_2O_2}$ and Y_{N_2}. Both positive and negative coefficients are observed. This is unlike the definition of mixture fraction [68] which is generally based on elemental mass fractions. Fig. 8.1 shows the scatter plot of p_1 vs. p_2 for all the points in the dataset. A large scatter is observed. It should be noted that the principal components might not be completely statistically independent. This is because in the derivation of PCA, it is assumed that the mean and variance are sufficient statistics for defining the PDF of reactive scalars. This assumption is required because only the covariance matrix is diagonalized in the derivation. If the statistics depend on higher moments, then PCA may not completely remove the redundancy in the system, and other advanced methods like the independent component analysis [78] may be required.

The results for case (B) are examined next. Table 8.2 shows the entries of c_{ij} for first two PCs. The coefficients for p_1, apart from that of Y_{N_2}, are very similar to those of case

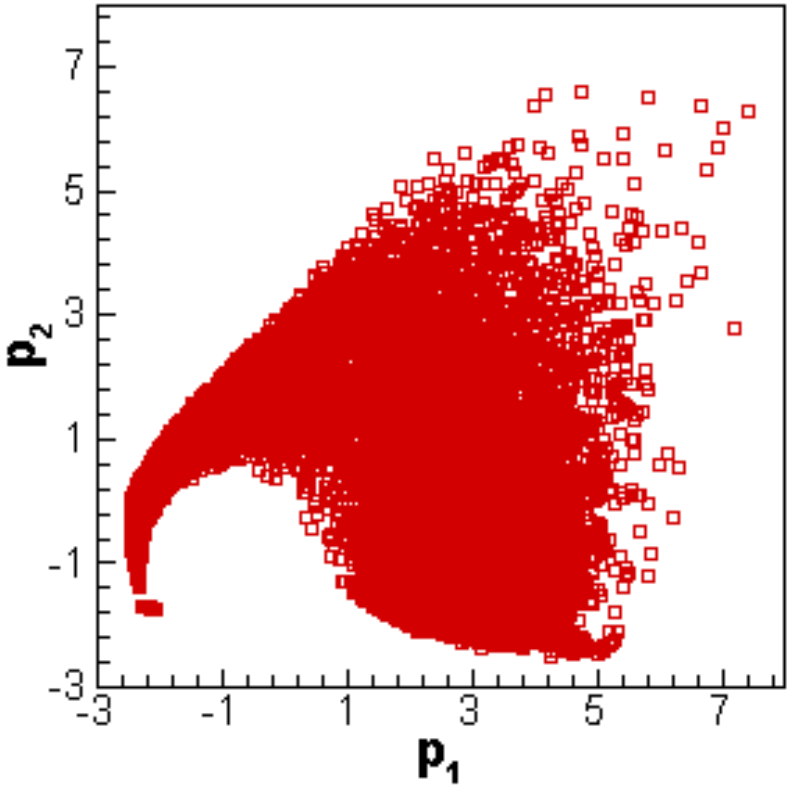

Figure 8.1: Scatter plot of p_1 vs. p_2 for all the points in the dataset, for case (A).

(A) indicating some universality for the first principal component. Coefficients for p_2 are, however, very different compared to those of case (A). Infact all the coefficients for p_2 are opposite in sign to those of case (A). Fig. 8.2 shows the scatter plot of p_1 vs. p_2 for all the points in the dataset. Again a large scatter is observed. The straight line in the top left area represents the scatter at initial time.

8.3.2 Parameterization of reactive scalars

The reactive scalars are now parameterized using the first two principal components p_1 and p_2. Fig. 8.3 shows the plots of all the reactive scalars (temperature and mass fraction of species) plotted in p_1 - p_2 space, for case (A). The horizontal axis in all the figures is p_1 and the vertical axis is the indicated reactive scalar. The color represents p_2, with values

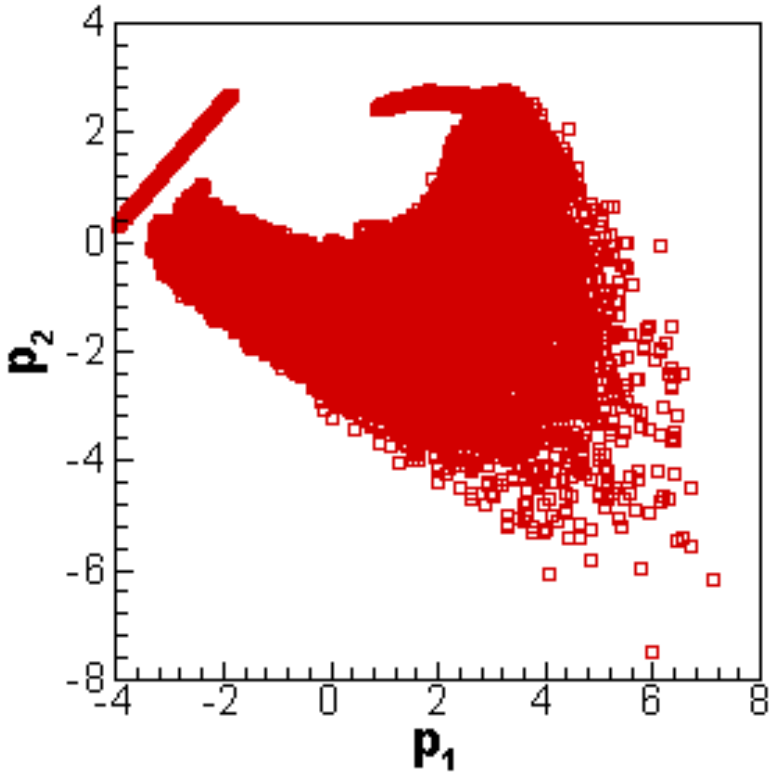

Figure 8.2: Scatter plot of p_1 vs. p_2 for all the points in the dataset, for case (B).

increasing from blue to red. Since the dataset represents the entire time history of the ignition and front propagation event, the range of all the reactive scalars in the figure vary from corresponding values in cold mixture to values in fully burnt mixture. For example, temperature ranges from 1032 K to 1551 K. It is observed that for all reactive scalars the two principal components do a good job in representing the entire dataset. The scatter within any given color is observed to be small.

Using the hypercube-based algorithm the thermochemical state is now parameterized using two principal components. Fig. 8.4 shows the created hypercubes using the hypercube algorithm in the two-dimensional p_1-p_2 space. The parameterized values in p_1-p_2 space at the centroids of hypercubes are obtained as the average of values for all the points in the corresponding hypercube. To quantitatively evaluate the error in parameterizing the

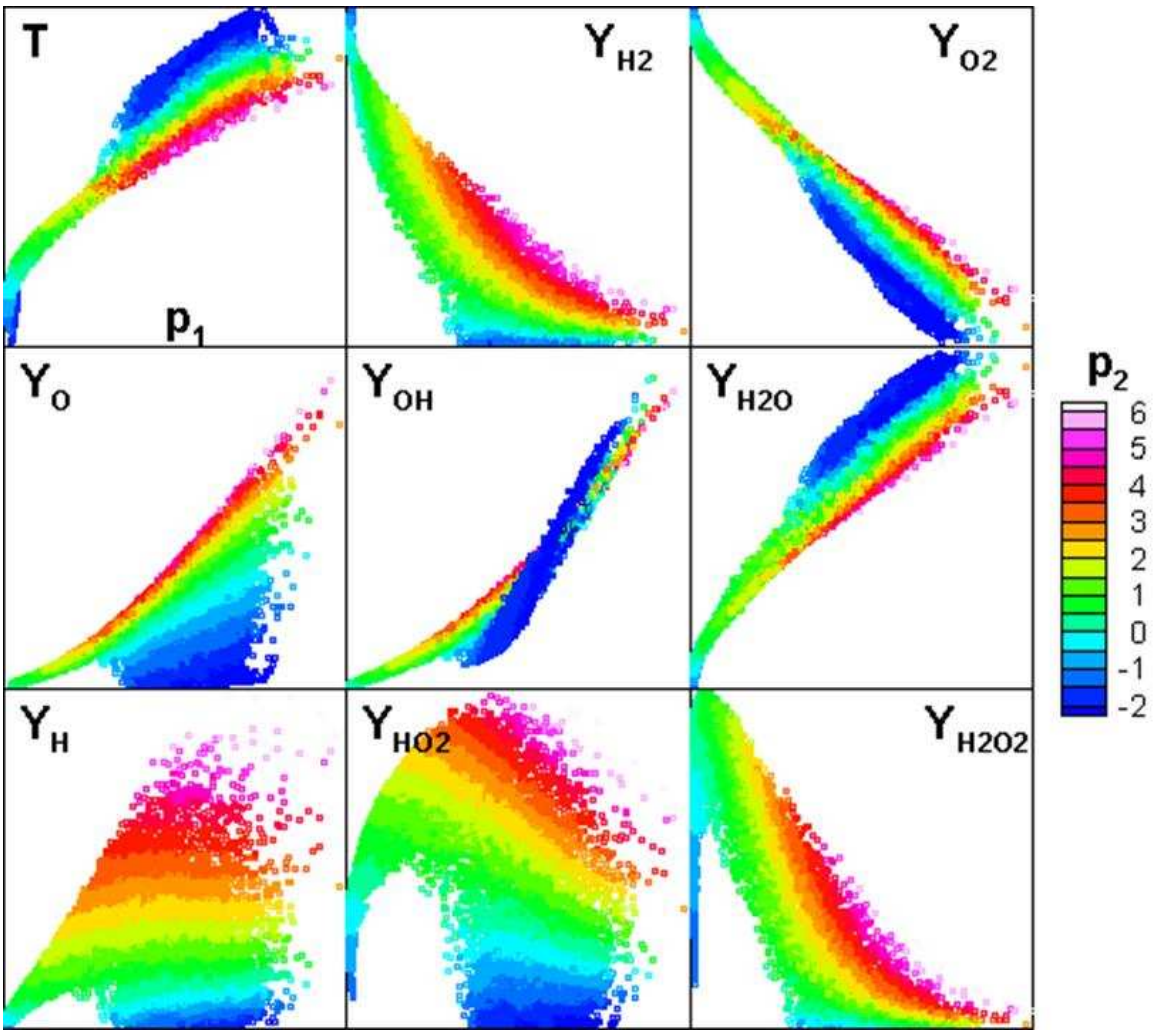

Figure 8.3: Parameterization of reactive scalars using p_1 and p_2, for case (A). The horizontal axis in all the figures is p_1 and the vertical axis is the indicated reactive scalar. The color represents p_2, with values increasing from blue to red.

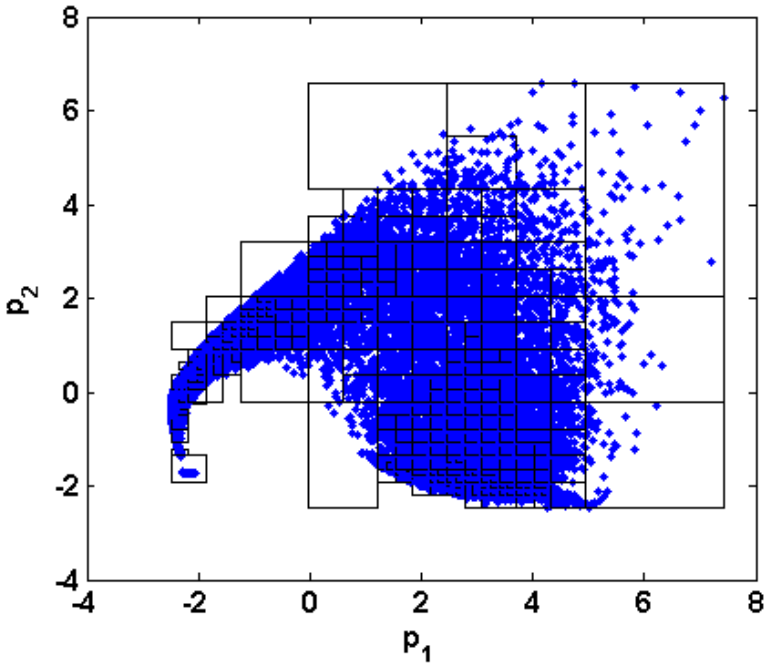

Figure 8.4: Hypercubes in 2D p_1-p_2 space, for case (A).

data in reduced dimension, R^2 values are calculated for any scalar φ similar to Ref. [37] as:

$$R^2 = 1 - \left[\sum_{i=1}^{m}(\varphi_i - \varphi_i^*)^2\right]\left[\sum_{i=1}^{m}(\varphi_i - \overline{\varphi})^2\right]^{-1} \tag{8.13}$$

where φ_i is the i^{th} observation, φ_i^* is the parameterized approximation to φ_i, and $\overline{\varphi_i}$ is the mean of φ_i. The maximum R^2 value can be one, and the error in the parameterization can be evaluated as the deviation of R^2 value from one. Fig. 8.5 shows the parity plot for temperature, for case (A), showing the plot of *observed* value obtained using DNS (T_i) against the parameterized value (T_i^*). Table 8.3 shows the computed R^2 values for the reactive scalar variables. Parameterization is done first using only p_1 and then using both p_1 and p_2. Temperature and all of the major species are observed to have high R^2 values using only one principal component. Using both p_1 and p_2, R^2 values very close to 1 are obtained for all variables, showing that only two principal components do an excellent job in parameterzing all the variables in the dataset.

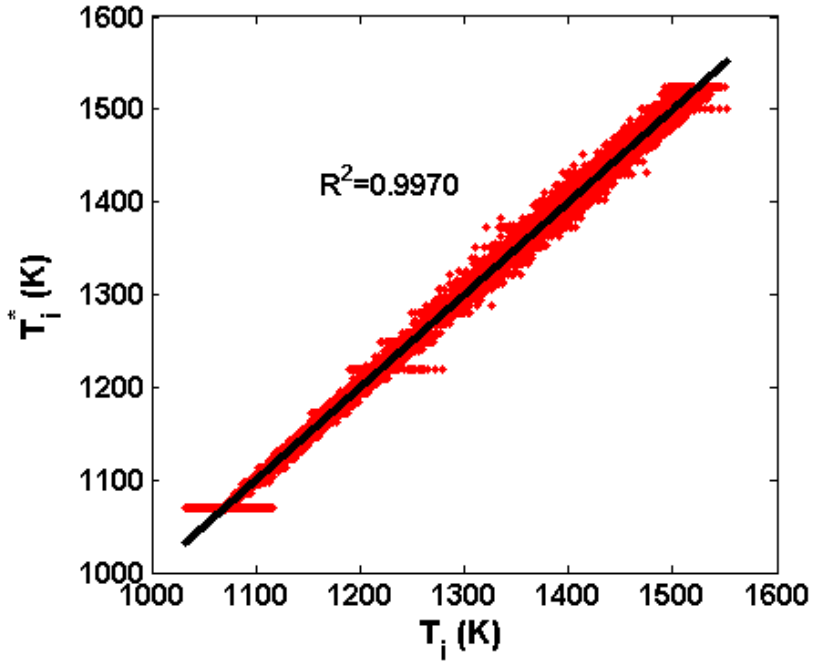

Figure 8.5: Parity plot for temperature, for case (A). X-axis is *observed* temperature (T_i) obtained from DNS, y-axis is parameterized temperature (T_i^*)

Parameterization	T	Y_{H_2}	Y_{O_2}	Y_O	Y_{OH}	Y_{H_2O}	Y_H	Y_{HO_2}	$Y_{H_2O_2}$
p_1	0.963	0.969	0.975	0.514	0.977	0.976	0.366	0.521	0.741
p_1-p_2	0.997	0.998	0.998	0.990	0.992	0.997	0.989	0.995	0.995

Table 8.3: R^2 values for reactive scalars for case (A)

Next the results for case (B) are investigated. Fig. 8.6 shows the plots of all the reactive scalars plotted in p_1 - p_2 space. The axes and coloring variable are similar to those for case (A). The distinct straight line in the scatter plots for T, Y_{H_2} and Y_{O_2} represents scatter at initial time. Once again, it is observed that for all reactive scalars the two principal components do a good job in representing the entire dataset, the scatter within any given color is observed to be small. Table 8.4 shows the computed R^2 values for the reactive scalar variables. Once again, p_1 is sufficient for parameterizing temperature and major species. Using both p_1 and p_2, R^2 values very close to 1 are obtained for all variables, showing again that only two principal components do an excellent job in parameterzing all

Parameterization	T	Y_{H_2}	Y_{O_2}	Y_O	Y_{OH}	Y_{H_2O}	Y_H	Y_{HO_2}	$Y_{H_2O_2}$
p_1	0.949	0.916	0.939	0.719	0.980	0.943	0.40	0.407	0.601
p_1-p_2	0.998	0.993	0.997	0.991	0.992	0.998	0.992	0.997	0.996

Table 8.4: R^2 values for reactive scalars for case (B)

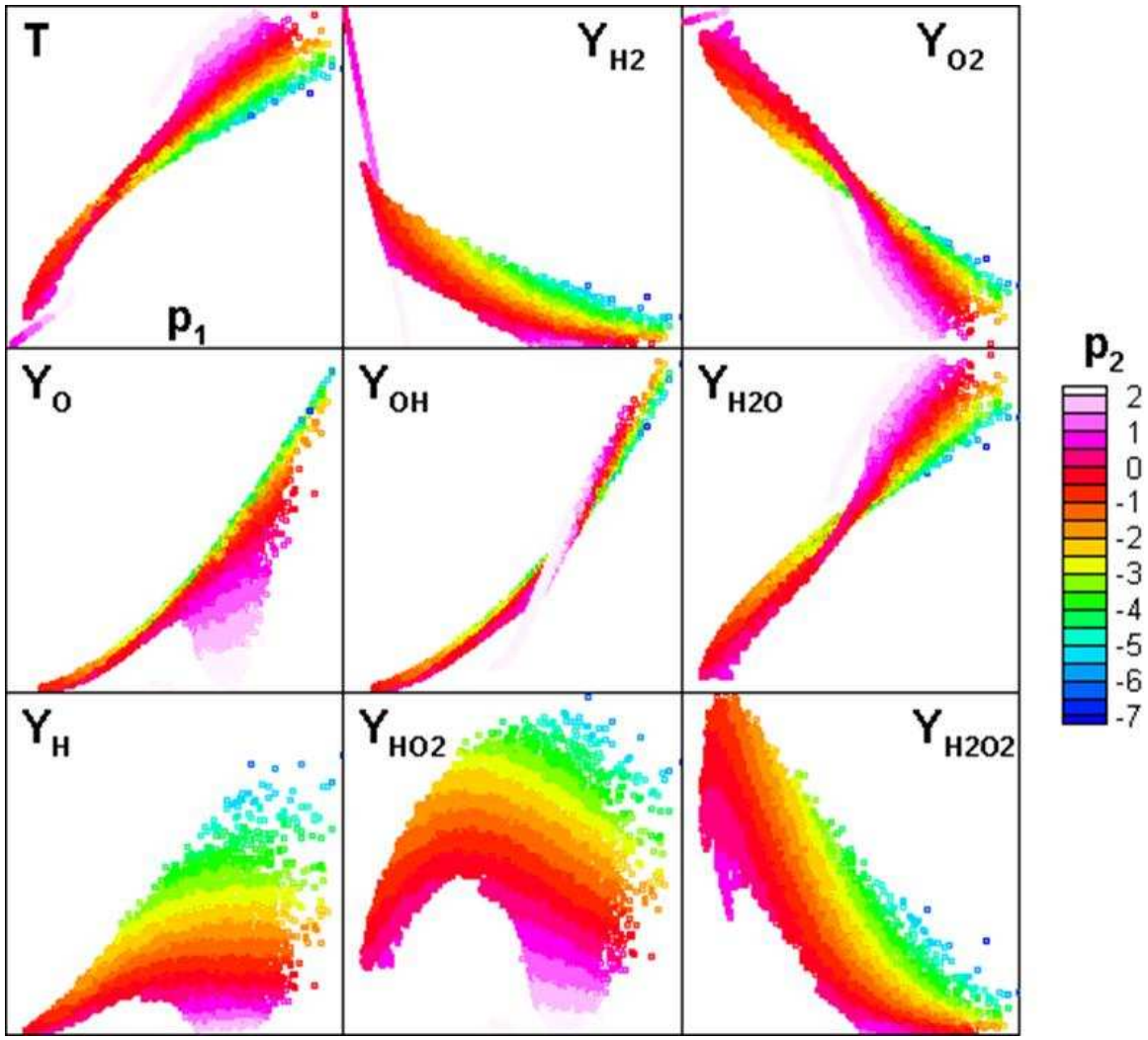

Figure 8.6: Parameterization of reactive scalars using p_1 and p_2, for case (B). The horizontal axis in all the figures is p_1 and the vertical axis is the indicated reactive scalar. The color represents p_2 with values increasing from blue to red.

the variables in the dataset.

It is interesting to compare the parameterizations obtained using the first two principal components with the standard parameterizations adopted in the existing flamelet- or CMC-based models. Mixture fraction (Z), specific total enthalpy (H), mixture fraction dissipation rate (χ) and specific total enthalpy dissipation rate (χ_{H}) are some of the common variables used for parameterizing the thermochemical state. Essentially, the steady flamelet model [79] is based on Z-χ parameterization. H-χ_{H} parameterization was recently adopted in an unsteady flamelet model for simulating auto-ignition in thermally stratified mixtures [80]. Z-H parameterization correspond to an equilibrium-model with no effects of dissipation rate. This parameterization is similar to the one employed in multi-zone models [11] used for simulating stratified HCCI combustion. Additionally, a two-dimensional unsteady flamelet model has been employed using Z,H,χ and χ_{H} based parameterization for simulating combustion in thermally and compositionally stratified engines [34]. Figs. 8.7 and 8.8 represent three different ways to parameterize temperature for cases (A) and (B), respectively. In these figures, vertical axis is temperature and horizontal axis is Z, H, and Z in left, middle, and right figures respectively. The coloring variable is χ, χ_{H}, and H in left, middle, and right figures, respectively. The distinct straight lines observed in some plots is the scatter at initial time. It should also be noted that in these figures, χ and χ_{H} are taken from DNS, whereas, in actual flamelet models they have to be modeled. Therefore, the results are independent of the modeling aspects of scalar dissipation rates.

For case (A), large scatter is observed using the Z-χ parameterization. This is not surprising since the mixture is very lean and no mixture fraction gradients are present at initial time. H-χ_{H} parameterization is better than Z-χ parameterization but still some scatter is observed. Z-H parameterization also shows some scatter. For case (B), again large scatter is observed with Z-χ parameterization. H-χ_{H} parameterization is better than Z-χ. Z-H parameterization in this case does a reasonably well job as scatter within any given color is not very large. It should be noted that unsteady effects are not incorporated

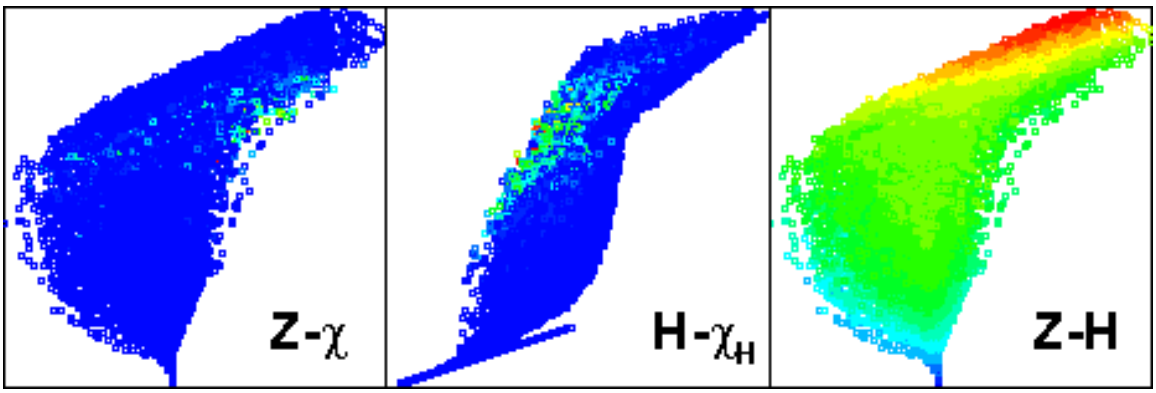

Figure 8.7: Case (A): Temperature parameterization using combination of some standard variables. Vertical axis is temperature, horizontal axis is Z, H, and Z in left, middle, and right figures, respectively. The coloring variable is χ, χ_{H}, and H in left, middle, and right figures, respectively.

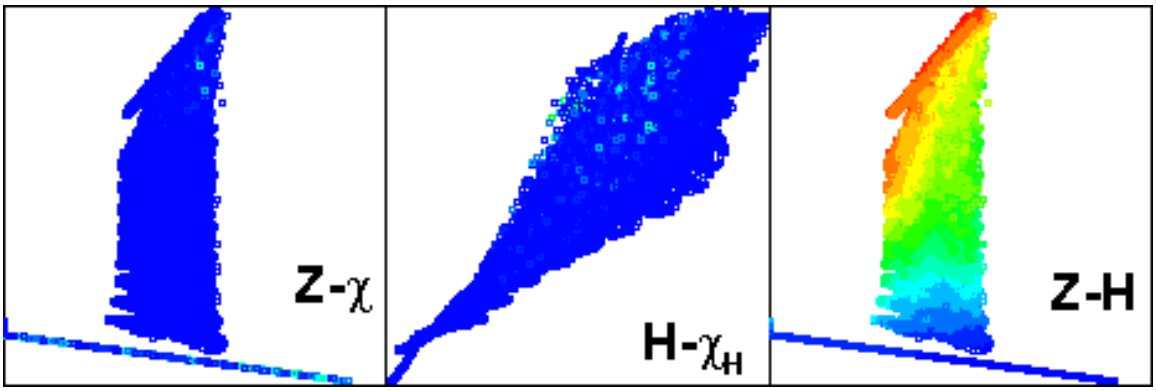

Figure 8.8: Case (B): Temperature parameterization using combination of some standard variables. Vertical axis is temperature, horizontal axis is Z, H, and Z in left, middle, and right figures, respectively. The coloring variable is χ, χ_{H}, and H in left, middle, and right figures, respectively.

Parameterization	T	Y_{H_2}	Y_{O_2}	Y_O	Y_{OH}	Y_{H_2O}	Y_H	Y_{HO_2}	$Y_{H_2O_2}$
Z-χ	0.754	0.740	0.784	0.433	0.832	0.769	0.234	0.342	0.573
H-χ_H	0.947	0.919	0.912	0.613	0.724	0.919	0.560	0.724	0.761
Z-H	0.948	0.919	0.932	0.711	0.901	0.925	0.657	0.791	0.766
Z-H-χ-χ_H	0.958	0.946	0.945	0.568	0.870	0.945	0.562	0.732	0.812
p_1-p_2	0.997	0.998	0.998	0.990	0.992	0.997	0.989	0.995	0.995

Table 8.5: R^2 values using standard parameterizations for case (A). Also shown are R^2 values using p_1 - p_2 parameterization, for comparison.

Parameterization	T	Y_{H_2}	Y_{O_2}	Y_O	Y_{OH}	Y_{H_2O}	Y_H	Y_{HO_2}	$Y_{H_2O_2}$
Z-χ	0.224	0.318	0.256	0.134	0.229	0.242	0.116	0.231	0.209
H-χ_H	0.943	0.913	0.887	0.682	0.735	0.895	0.685	0.823	0.832
Z-H	0.986	0.982	0.979	0.828	0.918	0.978	0.861	0.923	0.960
Z-H-χ-χ_H	0.984	0.977	0.975	0.817	0.909	0.974	0.841	0.915	0.959
p_1-p_2	0.998	0.993	0.997	0.991	0.992	0.998	0.992	0.997	0.996

Table 8.6: R^2 values using standard parameterizations for case (B). Also shown are R^2 values using p_1 - p_2 parameterization, for comparison.

here and the results will definitely improve when using an unsteady model. Note also that case (A) is physically more complex than case (B) since case (A) represents a mixed mode combustion with volumetric and front propagation modes present whereas case (B) represents largely a homogeneous auto-ignition. This is the reason why scalar dissipation rate effects are not so important for case (B). Tables 8.5 and 8.6 show the R^2 values when using these standard parameterizations. R^2 values for Z-H-χ-χ_H parameterization are also shown. It is observed that in some cases Z-H-χ-χ_H parameterization performes slightly poor compared to other two-variable parameterizations. This is because the data has to be conditioned four times for the Z-H-χ-χ_H parameterization and a bigger dataset may be required to perfectly do this parameterization. Nonetheless, the key point is that for both the cases R^2 values obtained using these parameterizations are much lower compared to those obtained using p_1-p_2 parameterization. In Tables 8.5 and 8.6, R^2 values obtained using p_1-p_2 parameterization are also shown for comparison purposes.

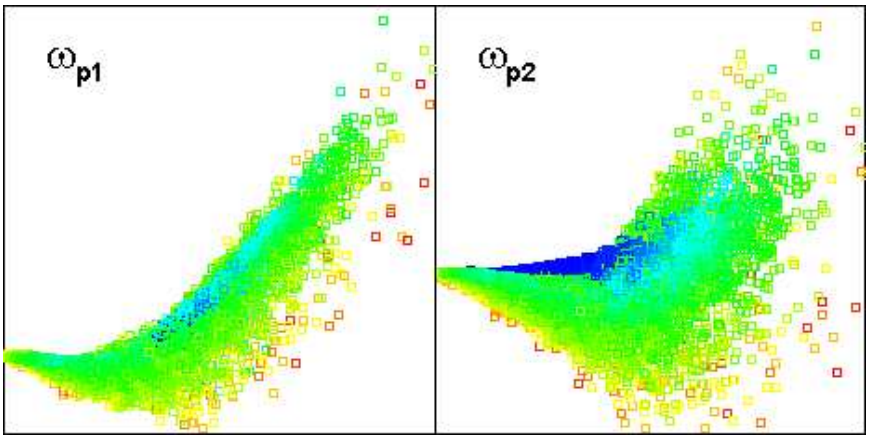

Figure 8.9: Principal component source terms for case (A). The horizontal axis in both the figures is p_2 and the vertical axis is the PC source term as indicated. The color represents p_1, with values increasing from blue to red.

8.3.3 Parameterization of source terms

As discussed in Section 8.2, PCs are not conserved variables and their source terms must also be parameterized in the principal component space. As discussed in Section 8.2, the source terms of principal components are also obtained using the coefficient matrix c_{ij} as: $\omega_{p_i} = \sum_{j=1}^{nsp+1} c_{ij}\omega_{\varphi_j}$. Here ω_{p_i} is the source term for i^{th} principal component and ω_{φ_j} is the source term for j^{th} reactive scalar, temperature being the first. Figs. 8.9 and 8.10 show for cases (A) and (B), respectively, the plots of ω_{p_1} and ω_{p_2} as a function of p_1 and p_2. The horizontal axis in both the figures is p_2 and the vertical axis is the PC source term as indicated. The color represents p_1, with values increasing from blue to red. For case (A), ω_{p_1} is observed to be reasonably well parameterized, whereas, ω_{p_2} plot does show some scatter. For case (B), both the source terms are observed to be very well parameterized with little scatter within any color. This is again not surprising because as mentioned earlier case (A) is physically more complex than case (B).

Tables 8.7 and 8.8 list R^2 values for source terms of p_1 and p_2 using only p_1 and p_1-p_2 parameterization. Using p_1-p_2 parameterization, high R^2 values are obtained for ω_{p_1} for case (A) and for both ω_{p_1} and ω_{p_2} for case (B). The low value of R^2 for ω_{p_2} for case

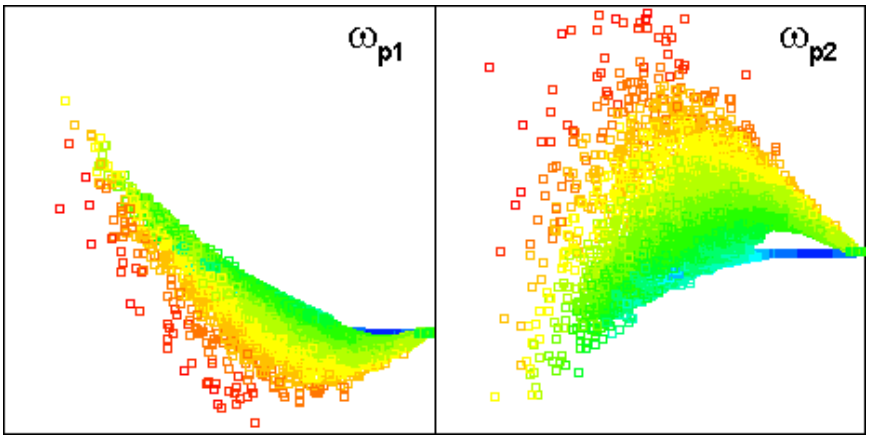

Figure 8.10: Principal component source terms for case (B). The horizontal axis in both the figures is p_2 and the vertical axis is the PC source term as indicated. The color represents p_1, with values increasing from blue to red.

Parameterization	ω_{p_1}	ω_{p_2}
p_1	0.275	0.197
p_1-p_2	0.900	0.511

Table 8.7: R^2 values for PC source terms, for case (A)

(A) may be improved by a variety of approaches. These include increasing the size of the dataset, performing PCA dynamically at each time-step, using other advanced regression techniques like adaptive regression [81], or by simply increasing the number of dimensions of the low-dimensional manifold (for example, 3 PCs can be used to parameterize the system). This is the subject of future studies.

The results presented in this chapter can be summarized as follows. Principal component analysis (PCA) is shown to be an excellent tool to obtain the inherent low-dimensional manifolds in complex mixed-mode combustion systems. PCA is a rigorous mathematical

Parameterization	ω_{p_1}	ω_{p_2}
p_1	0.262	0.689
p_1-p_2	0.960	0.923

Table 8.8: R^2 values for PC source terms, for case (B)

technique and the error in parameterization of thermochemical state in reduced dimension can be characterized using R^2 value. For mixed mode combustion systems, the principal component (PC) parameterization does a much better job in parameterizing the thermochemical state than the standard variables such as mixture fraction, enthalpy, and scalar dissipation rates which are largely based on physical intuition. As a caveat, it should be noted that PCs are not conserved scalars and therefore their source terms also need to be parameterized in PC space. Moreover, due to the non-conservative nature of PCs, new modeling strategies may be needed to achieve turbulent closure. Nonetheless, PCA may be combined with existing turbulent combustion models and can greatly aid in reducing the computational complexity in solving detailed chemistry.

Chapter 9

Conclusions and Future Work

In this dissertation, computational modeling of the autoignition and combustion processes in low temperature combustion (LTC) engine environments was carried out by using a variety of models. In particular, the effects of temperature and scalar inhomogeneities on autoignition were systematically investigated using various high-fidelity computational models: zero-dimensional homogeneous reactor model, one-dimensional opposed flow model, two-dimensional direct numerical simulation (DNS), and three-dimensional engine simulation with a Reynolds-Averaged Navier-Stokes (RANS) model. The fundamental understanding from these studies subsequently provided insights into a novel modeling strategy for mixed-mode turbulent combustion system based on principal component analysis (PCA). It was demonstrated that a significant reduction in computational complexity can be achieved by use of the newly identified low-dimensional manifolds. In the following, the major conclusions of this dissertation are summarized.

Homogeneous hydrogen-air autoignition subjected to temperature fluctuations The effect of unsteady temperature oscillation on the ignition of homogeneous constant-volume hydrogen-air mixture was studied computationally with detailed chemical kinetics and theoretically using large activation energy asymptotics. The asymptotic analysis was conducted for the low and high temperature regimes independently and the results were found to agree well with those obtained by direct numerical inte-

gration with detailed chemistry, confirming that the analysis properly captures the key chemical/thermal mechanisms driving ignition for a wide range of thermodynamic conditions. In both the high and low temperature ignition regimes, ignition delay showed a harmonic response to the imposed temperature oscillations. It was found that the ignition delay response in the first harmonic correlated well with the mean temperature during the induction period. For higher frequencies, ignition delay response was governed by the instantaneous temperature gradient of temperature oscillation at the onset of ignition, such that ignition is enhanced or retarded depending on the temporal gradient of the imposed temperature when the radical pool development is ripe for chemical and thermal runaway.

Nonpremixed hydrogen-air autoignition subjected to scalar dissipation rate fluctuations

The effects of unsteady scalar dissipation rate fluctuation on the ignition of a nonpremixed hydrogen/air mixture were studied using a counterflow configuration. Axial velocity at the nozzle inlet was imposed as a sinusoidal function in time, and the corresponding variation in the scalar dissipation rate at the ignition kernel was adopted as the main parameter. Two cases with different mean scalar dissipation rates were considered based on whether the mean scalar dissipation rate at ignition kernel is (a) less or (b) greater than the steady ignition limit. The results showed that the ignition behavior is characterized in three distinct regimes depending on the frequency. At low frequencies such that ignition occurs within one cycle of imposed oscillation (Regime I), the ignition delay correlates strongly with the mean scalar dissipation rate during the induction period. At very high frequencies (Regime III), the system again recovers a quasi-steady behavior, in which case the ultimate fate of the ignition kernel is dictated by the magnitude of the mean scalar dissipation rate relative to the steady ignition limit. At intermediate frequencies (Regime II), accurate prediction of the ignition delay requires the knowledge of cumulative history of the unsteady fluctuations. A new criterion for the ignitability, Γ, was defined as a

product of the mean kernel Damköhler number and the fractional duration of favorable condition for ignition. The ignition delay versus Γ showed excellent collapse for a wide range of parametric conditions, demonstrating the validity of the criterion in predicting the unsteady ignition characteristics. It was found that the ignition delay increases as Γ decreases, and the critical value of Γ was identified, below which the kernel fails to ignite because the radical generation cannot overcome the increased transport losses throughout the oscillatory cycles.

Nonpremixed *n*-heptane-air autoignition subjected to scalar dissipation rate fluctuations

The effects of unsteady scalar dissipation rate on high pressure autoignition of nonpremixed *n*-heptane were studied computationally using detailed chemistry in a counterflow configuration. Transient ignition subjected to steady scalar dissipation rate was first examined under the condition at which two-stage ignition occurs. It was found that ignition kernel starts on the hot oxidizer side where the magnitude of the scalar dissipation rate is very small, and then migrates toward the fuel rich zone toward the end of the first stage. This serves as a simple explanation for the observation that the first stage ignition is hardly affected by scalar dissipation rate variations. Similar to the hydrogen ignition case, the effect of oscillation frequency on the ignition delay was found to be highly non-monotonic. Again, three distinct frequency regimes were found with similar quasi-steady and unsteady behavior as for the hydrogen case. These results suggest that some conventional turbulent combustion models based on conserved scalar mapping need to be modified depending on the characteristic time scales of turbulent fluctuations.

Unsteady ignition at a higher temperature was also investigated. Even though the initial temperature was so high that only single-stage ignition behavior was observed at steady scalar dissipation rate conditions, the same mixture exhibited two-stage ignition when an oscillatory scalar dissipation rate was imposed. Unlike the typical two-stage ignition observed in a homogeneous mixture which is explained by the

NTC chemistry, the reappearance of the two-stage ignition at higher temperatures in the presence of unsteady scalar dissipation rate is attributed to the spatial broadening of the ignition kernel resulting in instantaneous enhancement in radical losses. The results may suggest higher possibilities of encountering two-stage ignition behavior in IC engines at higher levels of flow and scalar fluctuations.

Turbulent mixing in LTC engine environments Non-reacting realistic three-dimensional (3D) RANS engine simulations were carried out to explore the different mixture formation scenarios existing in an LTC engine prior to autoignition. Specifically, the influence of fuel spray injection timing on the correlation between temperature and equivalence ratio close to top-dead center was investigated. It was observed that early fuel injection results in a largely uncorrelated temperature-equivalence ratio fields, whereas late fuel injection results in a largely negatively correlated temperature-equivalence ratio fields.

DNS of autoignition and front propagation in LTC engine environments Based on the different mixture fields observed in the 3D RANS LTC engine simulations, parametric studies of the various scalar mixing scenarios were conducted using high-fidelity DNS. Results of two-dimensional DNS were investigated for three cases with different initial conditions: case (A) with only temperature inhomogeneities, case (B) with uncorrelated temperature and equivalence ratio fields, and case (C) with negatively correlated temperature and equivalence ratio fields. Front propagation was observed for cases (A) and (B) and homogeneous ignition was predominantly observed for case (C). Compared to case (A), ignition delay was found to decrease for case (B) and increase for case (C). Duration of heat release was increased for case (B) and decreased for case (C), compared to case (A). These results provide a counter-intuitive implication that early fuel-injection may result in front propagation through the engine and late fuel-injection may result in a more volumetric combustion mode.

To obtain a quantitative diagnostic criterion demarcating the different modes of heat release, one-dimensional simulations were performed for three different cases: (X), (Y) and (Z), with different initial temperature gradients (33.34 K/mm, 200 K/mm, and 466.67 K/mm, respectively). Case (X) showed a prolonged ignition delay compared to cases (Y) and (Z). It was observed that case (X) represents a homogeneous ignition with combustion occurring over a wide region. For cases (Y) and (Z) a wave-like front propagation was observed. A Damköhler number based on $\mathrm{HO_2}$ species ($\mathrm{Da_{HO_2}}$) was proposed to identify the roles of diffusion and reaction in the heat release process. A gradient ascent algorithm was employed to track the non-collocated peaks of diffusion and reaction in a front. The values of Damköhler number indicated that case (Y) represents a chemistry-driven spontaneous ignition front propagation, while case (Z) exhibits a typical deflagration front. The Damköhler number criterion was applied to 2D DNS cases and was found to be a useful computational diagnostic tool to identify the ignition regimes in multi-dimensional turbulent ignition problems.

Low-dimensional manifolds in mixed-mode combustion systems Principal component analysis was applied to high-fidelity DNS dataset of auto-ignition and front propagation in thermally and compositionally stratified turbulent hydrogen-air mixture. Two DNS cases with different initializations were investigated: case (A) with only temperature (T) inhomogeneities and uniform equivalence ratio (ϕ) field, and case (B) with negatively-correlated T-ϕ fields (These correspond to cases (A) and (C), respectively, of the DNS study presented in Chapter 7). PCA was applied to a data-set containing 25344 observations representing the time-history of the combustion event. It was found that only first two principal components (PCs) are sufficient to parameterize the thermochemical state for the entire DNS dataset with excellent accuracy.

PC parameterization was compared with other standard parameterizations such as Z-χ, H-χ_H, Z-H, and Z-H-χ-χ_H, which are adopted in existing turbulent combustion models. p_1-p_2 parameterization is found to work much better than any of these

standard parameterizations. Since PCs are not conserved scalars, source terms of the PCs were also parameterized in p_1-p_2 space. For case (A), ω_{p_1} was found to be reasonably well parameterized in p_1-p_2 space, while ω_{p_2} showed some scatter and was not very well parameterized. For case (B), both ω_{p_1} and ω_{p_2} were parameterized in p_1-p_2 space with good accuracy. Better regression techniques, larger dataset, dynamic PCA at each time-step, or a larger dimension of the PC manifold are some ideas which may be adopted for improving the parameterization of source terms. To achieve turbulent closure, models for average/filtered source terms of principal components are required. PCA may be combined with existing turbulent combustion models in either RANS or LES framework and can greatly aid in reducing the chemical complexity of the system.

9.1 Directions for Future Work

Based on the scientific findings and model developments obtained in this study, future research issues on turbulent combustion in LTC engine environments are summarized as follows.

Effects of unsteady turbulent flow on autoignition of nonpremixed fuel-air mixture In this dissertation, we have studied effects of unsteady scalar dissipation rate fluctuation on autoignition of nonpremixed fuel-air mixtures in Chapters 4 and 5. In these chapters ignition response to a monochromatic frequency of fluctuation of scalar dissipation rate was investigated. Real turbulent flows, however, contain a range of eddy turnover times and hence a range of frequencies. By combining a range of frequencies and through the use of turbulence energy cascade, an unsteady velocity fluctuation that mimics a turbulent flow can be specified at the nozzle inlets. The interaction of this "turbulent-like" scalar dissipation rate fluctuation on ignition behavior can then be studied. The results obtained in Chapters 4 and 5 will serve as a

building block for understanding the effects of more realistic “turbulent-like” scalar dissipation rate fluctuation.

Turbulent mixing in LTC engine environments In Chapter 6 RANS simulations using Kiva-3v were conducted in order to investigate mixing characteristics in an LTC engine. As mentioned in the Chapter 6 there remains a question as to how the large RANS-scale correlations between temperature and equivalence ratio relate to small subgrid-scale correlations. More work is required to shed light on this question. In particular large-eddy simulations of turbulent mixing might help in bridging the gap between large scale and small subgrid scale mixing characteristics. Experimental results might also be useful in this regard.

3D direct numerical simulations of higher hydrocarbons In Chapter 7 2D DNS of hydrogen autoignition in inhomogeneous mixtures is conducted. Real turbulent flows are, however, three-dimensional. To accurately represent three dimensional turbulent mixing characteristics 3D DNS simulations may be conducted. Results of 2D DNS presented in this dissertation will serve as reference cases to understand the more complex 3D simulations. Although, 3D DNS simulations will require new algorithms for feature detection and data mining on top of an extremely high computational overhead, significant new insights can be gained by conducting 3D simulations. Sreedhara and Lakshmisha [82] have conducted 3D DNS simulations of autoignition in non-premixed systems, albeit with reduced four step chemistry for *n*-heptane fuel. They specifically focussed on the differences between two- and three-dimensional turbulence and its effects on autoignition. They made two important conclusions: Firstly, the topology of autoignition spots remains the same irrespective of whether the flow is represented in two or three-dimensions, and secondly, the difference between two- and three-dimensional simulations arises from the fact that the kinetic energy dissipation (and hence the scalar dissipation rate) is more ac-

curately represented in the latter than in the former owing to the vortex-stretching phenomenon. Because of this, the autoignition delay time decreases with an increase in turbulence intensity in three-dimensional simulations, in a regime where the rate-limiting process is mixing. More three-dimensional simulations of autoignition of higher hydrocarbons with detailed chemistry are required to further shed light on this phenomena.

Generation of low-dimensional manifolds using principal component analysis In Chapter 8 principal component analysis (PCA) has been shown to be an excellent tool to obtain inherent low-dimensional manifolds in complex multi-mode combustion systems. This is a new attempt at turbulent combustion modeling with high promises, but is subjected to further improvements. First is to develop new methodologies to combine PCA with existing turbulent closure models such as transported pdf methods, flamelet, or CMC models. This will greatly aid in reducing the computational complexity in solving realistic detailed chemistry using these models. For example, in context of transported pdf models, transport equation for joint pdf of small number of principal components may be solved instead of solving that of large number of primitive reactive scalars such as species mass fractions and temperature. Alternatively, PCA may be combined with second order CMC method, thereby conditional mean, variance and covariance equations for a small number of principal components may be solved instead of solving a large number of those equations for primitive reactive scalars. Second area of improvement in combustion modeling with PCA is to develop better algorithms for parameterization of thermochemical state and source terms of principal components in the low-dimensional manifold. A hypercube-based algorithm was employed in the present study, but better regression algorithms based on state-of-the-art computational methods will significantly enhance the fidelity and efficiency of the model. Finally, as mentioned in Chapter 8, if the statistics of underlying system depend strongly on higher than second order moments, then PCA may

not completely remove the redundancy in the system. In this case, other advanced methods such as the independent component analysis [78] may be required. Further research is needed to explore this new opportunity.

Bibliography

[1] Zhao, F., Asmus, T., Assanis, D., Dec, J., Eng, J. and Najt, P. (2002). *Homogeneous Charge Compression Ignition (HCCI) Engines, Key Research and Development Issues*. Society of Automotive Engineers, Inc., Warrendale, Pennsylvania. 1

[2] A University Consortium on Low Temperature Combustion for High-Efficiency Ultra-Low Emission Engines, directed by the University of Michigan, funded by Department of Energy under agreement DE-FC26-06NT42629. 1

[3] Richter, M., Engstrom, J., Franke, A., Alden, M., Hultqvist, A. and Johansson, B. (2000). The Influence of Charge Inhomogeneity on the HCCI Combustion Process. *SAE Technical Paper*, 2000-01-2868. 2

[4] Graf, N., Gronki, J., Schulz, C., Baritaud, T., Cherel, J., Duret, P. and Lavy, J. (2001). In-Cylinder Combustion Visualization in an Auto-Igniting Gasoline Engine using Fuel Tracer- and Formaldehyde-LIF Imaging. *SAE Technical Paper*, 2001-01-1924. 2

[5] Collin, R., Nygren, J., Richter, M., Alden, M., Hildingsson, L. and Johansson, B. (2003). Simultaneous OH- and Formaldehyde-LIF Measurements in an HCCI Engine. *SAE Technical Paper*, 2003-01-3218.

[6] Kumano, K. and Iida, N. (2004). Analysis of the Effect of Charge Inhomogeneity on HCCI Combustion by Chemiluminescence Measurement. *SAE Technical Paper*, 2004-01-1902.

[7] Reuss, D. and Sick, V. (2005). Inhomogeneities in HCCI Combustion: An Imaging Study. *SAE Technical Paper*, 2005-01-2122.

[8] Dec, J. E., Hwang, W. and Sjoberg, M. (2006). An Investigation of Thermal Stratification in HCCI Engines using Chemiluminescence Imaging. *SAE Technical Paper*, 2006-01-1518. 2

[9] Epping, K., Aceves, S., Bechtold, R. and Dec, J. (2002). The Potential of HCCI Combustion for High Efficiency and Low Emissions. *SAE Technical Paper*, 2002-01-1923. 2

[10] Sjöberg, M., Dec, J. E. and Cernansky, N. P. (2005). Potential of Thermal Stratification and Combustion Retard for Reducing Pressure-Rise Rates in HCCI Engines,

Based on Multi-Zone Modelling and Experiments. *SAE Technical Paper*, 2005-01-0113. 2

[11] Babajimopoulos, A., Lavoie, G. A. and Assanis, D. (2003). Modelling HCCI Combustion with High Levels of Residual Gas Fraction - A Comparison of Two VVA Strategies. *SAE Technical Paper*, 2003-01-3220. 2, 8, 17, 66, 99

[12] Hasegawa, R. and Yanagihara, H. (2003). HCCI Combustion in DI Diesel Engine. *SAE Technical Paper*, 2003-01-0745. 2

[13] Hultqvist, A., Christenson, M., Johansson, B., Richter, M., Nygren, J., Hult, J. and Alden, M. (2002). The HCCI Combustion Process in a Single Cycle - High-Speed Fuel Tracer LIF and Chemiluminescence Imaging. *SAE Technical Paper*, 2002-01-0424. 2, 63, 71

[14] Walton, S. M., He, X., Zigler, B. T., Wooldridge, M. S. and Atreya, A. (2007). An Experimental Investigation of iso-Octane Ignition Phenomena. *Combust. Flame*, 150, pp. 246–262. 3

[15] Krasselt, J., Foster, D., Ghandhi, J., Herold, R., Reuss, D. and Najt, P. (2009). Investigations into the Effects of Thermal and Compositional Stratification on HCCI Combustion - Part I: Metal Engine Results. *SAE Technical Paper*, 2009-01-1105. 3, 63

[16] Herold, R. E., Krasselt, J. M., Foster, D. E. and Ghandhi, J. B. (2009). Investigations into the Effects of Thermal and Compositional Stratification on HCCI Combustion - Part II: Optical Engine Results. *SAE Technical Paper*, 2009-01-1106. 3, 63

[17] Zeldovich, Y. B. (1980). Regime Classification of an Exothermic Reaction with Nonuniform Initial Conditions. *Combust. Flame*, 39, pp. 211–214. 3, 7, 9, 69, 80

[18] Im, H. G., Chen, J. H. and Law, C. K. (1998). Ignition of Hydrogen-Air Mixing Layer In Turbulent Flows. *Proc. Combust. Inst.*, 27, pp. 1047–1056. 3

[19] Sung, C. J. and Law, C. K. (1997). Ignition of Oscillatory Counterflowing Nonpremixed Hydrogen against Heated Air. *Combust. Sci. Technol.*, 129, pp. 347–370. 6

[20] Im, H. G., Raja, L. L., Kee, R. J. and Petzold, L. R. (2000). A Numerical Study of Transient Ignition in a Counterflow Nonpremixed Methane-Air Flame Using Adaptive Time Integration. *Combust. Sci. Technol.*, 158, pp. 341–363. 6, 15

[21] Mason, S. D., Chen, J. H. and Im, H. G. (2002). Effects of Unsteady Scalar Dissipation Rate on Ignition of Non-premixed Hydrogen/Air Mixtures in Counterflow. *Proc. Combust. Inst.*, 29, pp. 1629–1636. 6, 20, 43

[22] Liu, S., Hewson, J. C., Chen, J. H. and Pitsch, H. (2004). Effects of Strain Rate on High-Pressure Nonpremixed *n*-Heptane Autoignition in Counterflow. *Combust. Flame*, 137, pp. 320–339. 6, 7, 48, 49

[23] Liu, S., Hewson, J. C. and Chen, J. H. (2006). Nonpremixed *n*-Heptane Autoignition in Unsteady Counterflow. *Combust. Flame*, 145, pp. 730–739. 6, 7

[24] Warnatz, J., Mass, U. and Dibble, R. W. (2001). *Combustion: Physical and Chemical Fundamentals, Modeling and Simulation, Experiments, Pollutant Formation*. Springer. 7, 48

[25] Babajimopoulos, A., Assanis, D. and Fiveland, S. B. (2002). An Approach for Modelling the Effects of Gas Exchange Processes on HCCI Combustion and its Application in Evaluating Variable Valve Timing Control Strategies. *SAE Technical Paper*, 2002-01-2829. 8, 17

[26] Sankaran, R., Im, H. G., Hawkes, E. R. and Chen, J. H. (2005). The Effects of Non-Uniform Temperature Distribution on the Ignition of a Lean Homogeneous Hydrogen-Air Mixture. *Proc. Combust. Inst.*, 30, pp. 875–882. 8, 9, 70, 72

[27] Chen, J. H., Hawkes, E. R., Sankaran, R., Mason, S. D. and Im, H. G. (2006). Direct Numerical Simulation of Ignition Front Propagation in a Constant Volume with Temperature Inhomogeneities: I. Fundamental Analysis and Diagnostics. *Combust. Flame*, 145, pp. 128–144. 9, 70, 72

[28] Hawkes, E. R., Sankaran, R., Pébay, P. P. and Chen, J. H. (2006). Direct Numerical Simulation of Ignition Front Propagation in a Constant Volume with Temperature Inhomogeneities: II. Parametric Study. *Combust. Flame*, 145, pp. 145–159. 8, 72

[29] Peters, N. (1988). Laminar Flamelet Concepts in Turbulent Combustion. *Proc. Combust. Inst.*, 21, pp. 1231–1250. 10, 60, 61

[30] Bilger, R. W. (1993). Conditional Moment Closure for Turbulent Reacting Flow. *Phys. Fluids A*, 5, p. 436. 10, 60

[31] Pope, S. B. (1991). Computations of Turbulent Combustion: Progress and Challenges. *Proc. Combust. Inst.*, 23, pp. 591–612. 10

[32] Pitsch, H., Chen, M. and Peters, N. (1998). Unsteady Flamelet Modeling of Turbulent Hydrogen-Air Diffusion Flames. *Proc. Combust. Inst.*, 27, pp. 1057–1064. 10

[33] Smith, N. S. A., Bilger, R. W. and Chen, J.-Y. (1992). Modelling of Nonpremixed Hydrogen Jet Flames using a Conditional Moment Closure Method. *Proc. Combust. Inst.*, 24, pp. 263–269. 10

[34] Cook, D. J., Pitsch, H. and Nentwig, G. (2008). Numerical Investigation of Unburnt Hydrocarbon Emissions in a Homogeneous-Charge, Late-Injection, Diesel-Fueled Engine. *SAE Technical Paper*, 2008-01-1666. 10, 99

[35] Cha, C. M., Kosály, G. and Pitsch, H. (2001). Modeling Extinction and Reignition in Turbulent Nonpremixed Combustion using a Doubly-Conditional Moment Closure Approach. *Phys. Fluids*, 13, p. 3824. 10

[36] Mastorakos, E. and Bilger, R. W. (1998). Second-Order Conditional Moment Closure for the Autoignition of Turbulent Flows. *Phys. Fluids*, 10, p. 1246. 10

[37] Sutherland, J. C. and Parente, A. (2009). Combustion Modeling using Principal Component Analysis. *Proc. Combust. Inst.*, 32, pp. 1563–1570. 11, 89, 90, 96

[38] Parente, A., Sutherland, J. C., Tognotti, L. and Smith, P. J. (2009). Identification of Low-Dimensional Manifolds in Turbulent Flames. *Proc. Combust. Inst.*, 32, pp. 1579–1586. 11

[39] Jackson, J. E. (1991). *A Users Guide to Principal Component Analysis*. Wiley Series in Probability and Statistics. 11, 87

[40] Jolliffe, I. T. (2002). *Principal Component Analysis (second ed.)*. Springer, New York. 11, 87

[41] Brown, P. N., Byrne, G. D. and Hindmarsh, A. C. (1989). VODE: A Variable Coefficient ODE Solver. *siamjsasc*, 10, pp. 1038–1051. 13

[42] Kee, R. J., Rupley, F. M. and Miller, J. A. (1991). Chemkin-II: A Fortran Chemical Kinetics Package for the Analysis of Gas-Phase Chemical Kinetics. Tech. Rep. SAND89-8009B, Sandia National Laboratories. 13, 16

[43] Peters, N. (2000). *Turbulent Combustion*. Cambridge University Press. 14

[44] Kee, R. J., Miller, J. A., Evans, G. H. and Dixon-Lewis, G. (1988). A Computational Model of the Structure and Extinction of Strained, Opposed Flow, Premixed Methane-Air Flames. *Proc. Combust. Inst.*, 22, pp. 1479–1494. 15

[45] Lutz, A. E., Kee, R. J., Grcar, J. F. and Rupley, F. M. (1997). OPPDIF: A Fortran Program for Computing Opposed-Flow Diffusion Flames. Tech. Rep. SAND96-8243, Sandia National Laboratories. 15, 16

[46] Raja, L. L., Kee, R. J. and Petzold, L. R. (1998). Simulation of the Transient, Compressible Gas-Dynamic Behavior of Catalytic-Combustion Ignition in Stagnation Flows. *Proc. Combust. Inst.*, 27, pp. 2249–2257. 15

[47] Im, H. G., Raja, L. L., Kee, R. J., Lutz, A. E. and Petzold, L. R. (2000). OPUS: A Fortran Program for Unsteady Opposed-Flow Flames. Tech. Rep. SAND2000-8211, Sandia National Laboratories. 16

[48] Li, S. and Petzold, L. R. (1999). Design of New DASPK for Sensitivity Analysis. Tech. Rep. TRCS99-23, Computer Science Department, University of California, Santa Barbara. 16

[49] Kee, R. J., Dixon-Lewis, G., Warnatz, J., Coltrin, M. E. and Miller, J. A. (1986). A Fortran Computer Code Package for the Evaluation of Gas-Phase Multicomponent Transport Properties. Tech. Rep. SAND86-8246, Sandia National Laboratories. 16

[50] Amsden, A. A., O'Rourke, P. J. and Butler, T. D. (1989). KIVA-II: A Computer Program for Chemically Reactive Flows with Sprays. Tech. Rep. LA-11560-MS, Los Alamos National Laboratory. 17

[51] Amsden, A. A. (1997). KIVA-3V: A Block-Structured KIVA Program for Engines with Vertical or Canted Valves. Tech. Rep. LA-13313-MS, Los Alamos National Laboratory. 17

[52] Hirt, C. W., Amsden, A. A. and Cook, J. L. (1974). An Arbitrary Lagrangian-Eulerian Computing Method for All Flow Speeds. *compphys*, 14, p. 227. 17

[53] Pracht, W. E. (1975). Calculating Three-Dimensional Fluid Flows at All Speeds with an Eulerian-Lagrangian Computing Mesh. *compphys*, 17, p. 132. 17

[54] Im, H. G. (2003). Formulation for Compressible Reacting Flow DNS. Personal Communication. 18

[55] Yoo, C. (2005). Direct Numerical Simulations of Strained Laminar and Turbulent Nonpremixed Flames: Computational and Physical Aspects. Tech. Rep. Ph.D. Dissertation, University of Michigan, Ann Arbor. 18

[56] Kennedy, C. A. and Carpenter, M. H. (1994). Several New Numerical Methods for Compressible Shear-layer Simulations. *Appl. Num. Math.*, 14(4), pp. 397–433. 18

[57] Kennedy, C. A., Carpenter, M. H. and Lewis, R. M. (2000). Low-storage Explicit Runge-Kutta Schemes for the Compressible Navier-Stokes Equations. *Appl. Num. Math.*, 35(3), pp. 177–219. 18

[58] Mueller, M. A., Kim, T., Yetter, R. and Dryer, F. (1999). Flow Reactor Studies and Kinetic Modeling of the H//2/O//2 Reaction. *Int. J. Chem. Kinetics*, 31(2), pp. 113–125. 18, 91

[59] Smooke, M. D. and Giovangigli, V. (1991). *Reduced Kinetic Mechanisms and Asymptotic Approximations for Methane-Air Flames, in: Lecture Notes in Physics*, vol. 384. Springer-Verlag, New York. 18

[60] Kee, R. J., Rupley, F. M., Meeks, E. and Miller, J. A. (1996). Chemkin-III: A Fortran Chemical Kinetics Package for the Analysis of Gas-Phase Chemical and Plasma Kinetics. Tech. Rep. SAND96-8216, Sandia National Laboratories. 18

[61] Semenov, N. N. (1958). Some Problems in Chemical Kinetics and Reactivity, Vols I and II. Tech. rep., Princeton: Princeton University Press. 19, 22, 23

[62] Yetter, R. A., Dryer, F. L. and Rabitz, H. (1991). A Comprehensive Reaction Mechanism for Carbon Monoxide/Hydrogen/Oxygen Kinetics. *Combust. Sci. Technol.*, 79, pp. 97–128. 20, 23, 24, 25, 35

[63] Kreutz, T. G. and Law, C. K. (1996). Ignition in Non-Premixed Counterflowing Hydrogen versus Heated Air: Computational Study with Detailed Chemistry. *Combust. Flame*, 104, pp. 157–175. 20

[64] Helenbrook, B. T., Im, H. G. and Law, C. K. (1998). Theory of Radical-Induced Ignition of Counterflowing Hydrogen versus Oxygen at High Temperatures. *Combust. Flame*, 112, pp. 242–252. 20, 23

[65] Law, C. K. (2006). *Combustion Physics*. Cambridge University Press. 20, 35

[66] Im, H. G., Helenbrook, B. T., Lee, S. R. and Law, C. K. (1996). Ignition in the Supersonic Hydrogen/Air Mixing Layer with Reduced Reaction Mechanisms. *J. Fluid Mech.*, 322, pp. 275–296. 23, 25

[67] Sánchez, A. L., Balakrishnan, G., nán, A. L. and Williams, F. A. (1996). Relationships between Bifurcation and Numerical Analyses for Ignition of Hydrogen/Air Diffusion Flames. *Combust. Flame*, 105, pp. 569–590. 23

[68] Bilger, R. W. (1989). The Structure of Turbulent Nonpremixed Flames. *Proc. Combust. Inst.*, 22, pp. 475–488. 36, 49, 92

[69] Bansal, G., Im, H. G. and Lee, S. R. (2009). Auto-Ignition of Homogeneous Hydrogen-Air Mixture subjected to Unsteady Temperature Fluctuations. *Combust. Theory Modelling*, in press. 41

[70] Bansal, G., Im, H. G. and Lee, S. R. (2009). Effects of Scalar Dissipation Rate Fluctuations on Autoignition of Hydrogen-Air Mixture. *AIAA J.*, 47 (2), pp. 468–472. 55, 57, 71

[71] Hinze, J. O. (1975). *Turbulence*. McGraw-Hill, New York. 70

[72] Funk, C., Sick, V., Reuss, D. L. and Dahm, W. J. A. (2002). Turbulence Properties of High and Low Swirl In-Cylinder Flows. *SAE Technical Paper*, 2002-01-2841. 70

[73] Bansal, G., Im, H. G. and Lee, S. R. (2009). Autoignition of Non-Premixed *n*-Heptane/Air Counterflow subjected to Unsteady Scalar Dissipation Rate. *Proc. Combust. Inst.*, 32, pp. 1083–1090. 71

[74] Bradley, D., Morley, C., Gu, X. J. and Emerson, D. R. (2002). Amplified Pressure Waves During Autoignition: Relevance to CAI Engines. *SAE Technical Paper*, 2002-01-2868. 78

[75] Gu, X. J., Emerson, D. R. and Bradley, D. (2003). Modes of Reaction Front Propagation from Hot Spots. *Combust. Flame*, 133, pp. 63–74.

[76] Sankaran, R. and Im, H. G. (2005). Characteristics of Auto-Ignition in a Stratified Iso-Octane Mixture with Exhaust Gases under Homogeneous Charge Compression Ignition Conditions. *Combust. Theory Modelling*, 9, pp. 417–432. 78

[77] Bansal, G. and Im, H. G. (2009). Autoignition of Hydrogen-Air Mixture with Temperature and Composition Inhomogeneities. In *47th AIAA Aerospace Sciences Meeting and Exhibit*, pp. AIAA Paper 2009–1559. Orlando, FL, USA. 91

[78] Comon, P. (1994). Independent Component Analysis, A New Concept ? *Signal Process.*, 36, pp. 287–314. 92, 113

[79] Liew, S. K., Bray, K. N. C. and Moss, J. B. (1984). A Stretched Laminar Flamelet Model of Turbulent Nonpremixed Combustion. *Combust. Flame*, 56, pp. 199–213. 99

[80] Cook, D. J., Pitsch, H., Chen, J. H. and Hawkes, E. R. (2007). Flamelet-Based Modeling of Auto-Ignition with Thermal Inhomogeneities for Application to HCCI Engines. *Proc. Combust. Inst.*, 31, pp. 2903–2911. 99

[81] Friedman, J. H. (1991). Multivariate Adaptive Regression Splines. *Ann. Stat.*, 19, pp. 1–67. 103

[82] Sreedhara, S. and Lakshmisha, K. N. (2002). Autoignition in a Non-Premixed Medium: DNS Studies on the Effects of Three-Dimensional Turbulence. *Proc. Combust. Inst.*, 29, pp. 2051–2059. 111